SCIENCE & TECHNOLOGY

ARS JOURNAL

A PUBLICATION OF THE AMERICAN ROCKET SOCIETY

VOLUME 30 NUMBER 11 NOVEMBER 1960

ANGELES PUBLIC LIBRARY

DEC 9 1960

BIND

CONTRIBUTED ARTICLES

Structures Considerations in Design for Space Boosters . . . . Paul E. Sandorff 999

Fundamental Satellite Perturbations . . . . . F. T. Geyling 1009

Optimum Orbital Transfer by Impulses . . . . . Lu Ting 1013

Relative Thermodynamic Efficiency of Supersonic Combustion and Subsonic Combustion Hypersonic Ramjets . . . . . George H. McLafferty 1019

Effect of Nonlinear Losses on the Design of Absorbers for Combustion Instabilities . . . . . A. W. Blackman 1022

TECHNICAL NOTES

Specific Heat Inequality Effect in the Chemically Frozen Stagnation Point Boundary Layer . . . . . George R. Inger 1028

Transient Heat Conduction in a Melting Finite Slab: An Exact Solution . . R. W. Sanders 1030

Further Comments on the Measurement of the Speed of Propagation of Turbulent Combustion . . . . . R. E. Bolz and H. Burlage Jr. 1032

Optimum Time to Rendezvous . . . . . John M. Eggleston 1089

Approximate Solution for Rocket Flight With Linear-Tangent Thrust Attitude Control. . . . . John S. MacKay 1091

Free Surface Condition for Sloshing Resulting From Pitching and Some Corrections . . . . . Wen-Hwa Chu 1093

Lateral Hydrodynamic Forces on an Airborne Missile Launched Underwater . . . . . Theodore R. Goodman 1095

Comparison of Gas-Turbine Cycles for Space Applications . . . . . Robert E. English and Henry O. Slone 1097

Rocket Propulsion With Nuclear Power . . . . . E. L. Resler Jr. and N. Rott 1099

DEPARTMENTS

Technical Comments 1101

Book Reviews 1106

New Patents 1109

Technical Literature Digest 1111

RUSSIAN SUPPLEMENT . . . 1033–1088

SOLID PROPELLANT ROCKET RESEARCH
VOLUME I, ARS PROGRESS SERIES . . . 998

because this oxidizer's stored aboard

Nitrogen Tetroxide provides immediate, hypergolic ignition with amine fuels. Even after 9 years of storage, nitrogen tetroxide is ready for instant use. Combustion efficiencies closely approach the theoretical 99%.

N_2O_4—**Requires no refrigeration**—can be stored indefinitely in missiles at launching sites.—**Can be used with most fuels**—including those containing carbon.—**Eliminates rough starts**—fast reaction prevents accumulation of propellants in thrust chambers.—**Allows throttleable control** of motors.

We'll gladly supply technical literature, including: a 59-page Product Bulletin, and a brochure entitled "Large Scale Handling of Nitrogen Tetroxide."

For specifications and local offices, see our insert in Chemical Materials Catalog, pages 475-482 and in Chemical Week Buyers Guide, pages 37-44.

BASIC TO AMERICA'S PROGRESS

Allied Chemical

NITROGEN DIVISION
Dept. NT14-21-3, 40 Rector Street, New York 6, N.Y.

2819

Will The Mission Succeed?

Ask . . .

DATS

(Dynamic Accuracy Test System)

Flight-line checkout by DATS (Dynamic Accuracy Test System) tells the interceptor commander whether his aircraft and weapon control systems are completely ready for a successful mission. As a result of field evaluation tests, showing the effectiveness of DATS in improving weapon control performance, RCA has been awarded an Air Force production contract. Developed by RCA's Airborne Systems Division, Defense Electronic Products, Camden, New Jersey, DATS is a new approach to the evaluation of system readiness.

It makes certain that only aircraft with properly operating weapon control systems are sent on missions. Based on a building-block design employing the highest reliability factors, a mechanical programming device and self-test capability, DATS utilizes a series of synthesized attack runs typical of mission conditions. DATS could be made applicable to many interceptor types of aircraft.

The Most Trusted Name in Electronics

RADIO CORPORATION OF AMERICA

ARS JOURNAL

A PUBLICATION OF THE AMERICAN ROCKET SOCIETY

EDITOR **Martin Summerfield**

ASSOCIATE TECHNICAL EDITOR **Irvin Glassman**

MANAGING EDITOR **Barbara Nowak**

ART EDITOR **John Culin**

ASSOCIATE EDITORS

Ali Bulent Cambel, *Northwestern University, Book Reviews;* **Igor Jurkevich,** *G. E. Space Sciences Laboratory, Russian Supplement;* **George F. McLaughlin,** *Patents;* **Charles J. Mundo Jr.,** *Raytheon Co., Guidance;* **Bernard H. Paiewonsky,** *Aeronautical Research Associates of Princeton, Flight Mechanics;* **M. H. Smith,** *Princeton University, Technical Literature Digest*

ASSISTANT EDITORS

Julie Hight, Carol Rubenstein, Estelle Viertel

DIRECTOR OF MARKETING

Owen Kean

ADVERTISING PROMOTION MANAGER

Robert M. Lamb

ADVERTISING PRODUCTION MANAGER

Walter Brunke

ADVERTISING REPRESENTATIVES

New York
D. C. Emery and Associates
400 Madison Ave., New York, N. Y.
Telephone: Plaza 9-7460

Los Angeles
James C. Galloway and Co.
6535 Wilshire Blvd., Los Angeles, Calif.
Telephone: Olive 3-3223

Chicago
Jim Summers and Associates
35 E. Wacker Dr., Chicago, Ill.
Telephone: Andover 3-1154

Detroit
R. F. Pickrell and Vincent Purcell
318 Stephenson Bldg., Detroit, Mich.
Telephone: Trinity 1-0790

Boston
Robert G. Melendy
17 Maugus Ave., Wellesley Hills, Mass.
Telephone: Cedar 5-6503

Pittsburgh
C. F. Livingston
17 Canterbury Rd., Pittsburgh 2, Pa.
Telephone: Poplar 6-8639

American Rocket Society

500 Fifth Avenue, New York 36, N. Y.

Founded 1930

OFFICERS

President	Howard S. Seifert
Vice-President	Harold W. Ritchey
Executive Secretary	James J. Harford
Treasurer	Robert M. Lawrence
General Counsel	Andrew G. Haley
Director of Publications	Irwin Hersey

BOARD OF DIRECTORS

Terms expiring on dates indicated

Ali B. Cambel	1962	William H. Pickering	1961
Richard B. Canright	1962	Simon Ramo	1960
James R. Dempsey	1961	William L. Rogers	1960
Herbert Friedman	1962	David G. Simons	1961
Robert A. Gross	1962	John L. Sloop	1961
Samuel K. Hoffman	1960	Martin Summerfield	1962
A. K. Oppenheim	1961	Wernher von Braun	1960
		Maurice J. Zucrow 1960	

TECHNICAL COMMITTEE CHAIRMEN

C. Daniel Brewer, Solid Rockets
Ali B. Cambel, Magnetohydrodynamics
William H. Dorrance, Hypersonics
James S. Farrior, Guidance and Navigation
Herbert Friedman, Physics of the Atmosphere and Space
George Gerard, Structures and Materials
Martin Goldsmith, Liquid Rockets
Andrew G. Haley, Space Law and Sociology
Samuel Herrick, Astrodynamics
Maxwell W. Hunter, Missiles and Space Vehicles
David B. Langmuir, Ion and Plasma Propulsion
Max A. Lowy, Communications
Irving Michelson, Education
Peter L. Nichols Jr., Propellants and Combustion
Eugene Perchonok, Ramjets
Richard A. Schmidt, Test, Operations and Support
C. J. Wang, Nuclear Propulsion
Stanley C. White, Human Factors and Bioastronautics
George F. Wislicenus, Underwater Propulsion
John E. Witherspoon, Instrumentation and Control
Abe M. Zarem, Power Systems

Scope of ARS JOURNAL

This Journal is devoted to the advancement of astronautics through the dissemination of original papers disclosing new scientific knowledge and basic applications of such knowledge. The sciences of astronautics are understood here to embrace selected aspects of jet and rocket propulsion, spaceflight mechanics, high speed aerodynamics, flight guidance, space communications, atmospheric and outer space physics, materials and structures, human engineering, overall system analysis, and possibly certain other scientific areas. The selection of papers to be printed will be governed by the pertinence of the topic to the field of astronautics, by the current or probable future significance of the research, and by the importance of distributing the information to the members of the Society and to the profession at large.

Information for Authors

Manuscripts must be as brief as the proper presentation of the ideas will allow. Exclusion of dispensable material and conciseness of expression will influence the Editors' acceptance of a manuscript. In terms of standard-size double-spaced typed pages, a typical maximum length is 22 pages of text (including equations), 1 page of references, 1 page of abstract and 12 illustrations. Fewer illustrations permit more text, and vice versa. Greater length will be acceptable only in exceptional cases.

Short manuscripts, not more than one quarter of the maximum length stated for full articles, may qualify for publication as Technical Notes or Technical Comments. They may be devoted to new developments requiring prompt disclosure or to comments on previously published papers. Such manuscripts are published within a few months of the date of receipt.

Sponsored manuscripts are published occasionally as an ARS service to the industry. A manuscript that does not qualify for publication, according to the above-stated requirements as to subject, scope or length, but which nevertheless deserves widespread distribution among jet propulsion engineers, may be printed as an extra part of the Journal or as a special supplement, if the author or his sponsor will reimburse the Society for actual publication costs. Estimates are available on request. Acknowledgment of such financial sponsorship appears as a footnote on the first page of the article. Publication is prompt since such papers are not in the ordinary backlog.

Manuscripts must be double spaced on one side of paper only with wide margins to allow for instructions to printer. Include a 100 to 200 word abstract. State the authors' positions and affiliations in a footnote on the first page. Equations and symbols may be handwritten or typewritten; clarity for the printer is essential. Greek letters and unusual symbols should be identified in the margin. If handwritten, distinguish between capital and lower case letters, and indicate subscripts and superscripts. References are to be grouped at the end of the manuscript and are to be given as follows. For journal articles: Authors first, then title, journal, volume, year, page numbers; for books: Authors first, then title, publisher, city, edition and page or chapter numbers. Line drawings must be clear and sharp to make clear engravings. Use black ink on white paper or tracing cloth. Lettering should be large enough to be legible after reduction. Photographs should be glossy prints, not matte or semi-matte. Each illustration must have a legend; legends should be listed in order on a separate sheet.

Manuscripts must be accompanied by written assurance as to security clearance in the event the subject matter lies in a classified area or if the paper originates under government sponsorship. Full responsibility rests with the author.

Preprints of papers presented at ARS meetings are automatically considered for publication.

Submit manuscripts in duplicate (original plus first carbon, with two sets of illustrations) to the Managing Editor, ARS JOURNAL, 500 Fifth Avenue, New York 36, N.Y.

ARS JOURNAL is published monthly by the American Rocket Society, Inc. and the American Interplanetary Society at 20th & Northampton Sts., Easton, Pa., U. S. A. Editorial offices: 500 Fifth Ave., New York 36, N. Y. Price: $12.50 per year, $2.00 per single copy. Second-class postage paid at Easton, Pa., with additional entry at New York, N. Y. This publication is authorized to be mailed at the special rates of postage prescribed by Section 132.122. Notice of change of address should be sent to the Secretary, ARS, at least 30 days prior to publication. Opinions expressed herein are the authors' and do not necessarily reflect the views of the Editors or of the Society.

© Copyright 1960 by the American Rocket Society, Inc.

The national security need for **S**pace **T**echnology **L**eadership

Space is a medium in which many military missions can be most effectively performed • The U. S. arsenal of ballistic missiles—in being and forthcoming — the Air Force Thor, Atlas, Titan, and Minuteman, the Navy Polaris, and the Army Jupiter, are all designed to deter the outbreak of a nuclear World War III or to retaliate overwhelmingly if it should occur • If our ballistic missiles are to realize their greatest potential in carrying out their dual task, they must be supported by a number of companion space systems for such missions as early warning, reconnaissance, communications, navigation, weather forecasting. Space Technology Laboratories is proud of its contributions to the national space effort as a principal contractor in carrying out major programs for the Air Force Ballistic Missile Division, National Aeronautics and Space Administration, and Advanced Research Projects Agency • The increasing scope of STL's activity is opening up exceptional opportunities for the exceptional scientist and engineer, who will find creativity given encouragement and recognition in an organization synonymous with Space Technology Leadership. Resumes and inquiries will receive meticulous attention.

SPACE TECHNOLOGY LABORATORIES, INC. P.O. BOX 95005C, LOS ANGELES 45, CALIFORNIA

a subsidiary of Thompson Ramo Wooldridge Inc.

Los Angeles • Santa Maria • Edwards Rocket Base • Cheyenne Cape Canaveral • Manchester, England • Singapore • Hawaii

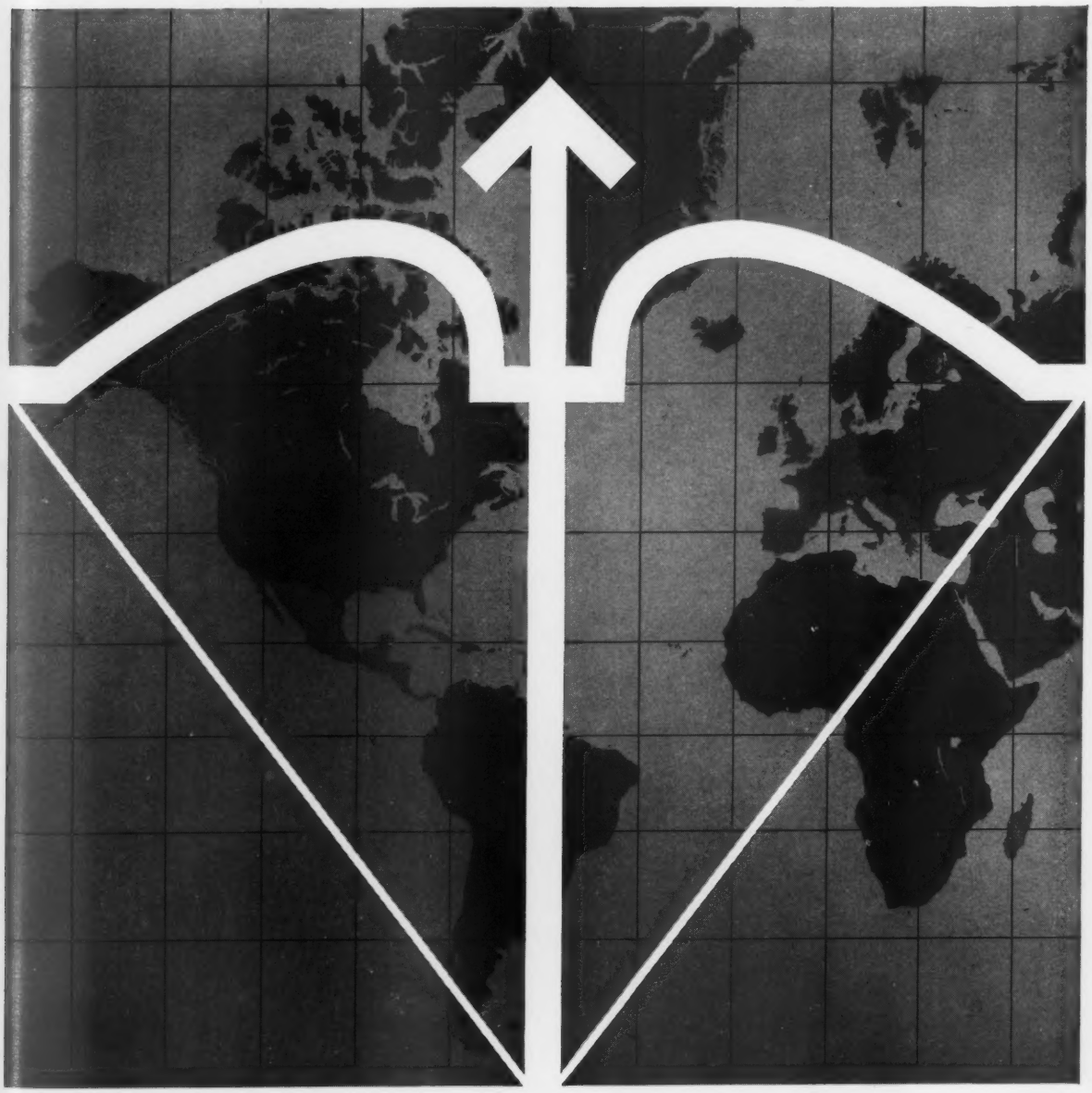

Is the "S" curve our best missile defense?

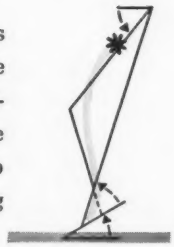

There have been many theories advanced on techniques of ICBM intercept, including those that postulate the use of an anti-missile missile. Some studies favor a head-on course for the weapon during terminal phase because any angle other than 180° from warhead flight allows too much error-margin, and 360° allows too much time lag for the "chase."

■ To give the anti-missile as much time as possible to seek the warhead, and lower the maneuverability requirements, it should be in the air ready to intercept while computers translate the acquisition signals into a plotted line of approach. Thus the anti-weapon can be closing the altitude gap before it "knows" the exact approach vector. The path described by this anti-missile would take the form of an "S" curve.

■ Yet, there may be other, more effective means of intercept. At Loral, where fresh attacks on formalized thinking result in new concepts for defense, the broad approach to problems such as this is backed in depth by advanced research in such fields as electronic scanning and electro-optics. And from these probings come designs that our production teams turn into operational defense hardware.

■ If you are a senior engineer or scientist interested in being part of this rapidly-expanding thinking group, write LORAL Electronics Corporation, New York 72, New York.

LORAL

Imprint of Integrity

Expertness in Systems Management through Experience in Systems R&D for Anti-Submarine Warfare, Passive Surveillance, Electronic Countermeasures, Penetration Aids, Navigation, Reconnaissance, Early Warning, and related areas of defense.

Regional Engineering Offices: Boston, Massachusetts; Dayton, Ohio; Tustin, California; Washington, D. C.

Yerkes Observatory photograph, taken October 23, 1911

PROGRESS IN ASTRONAUTICS AND ROCKETRY

SPONSORED BY THE AMERICAN ROCKET SOCIETY

Series Editor
MARTIN SUMMERFIELD
Princeton University

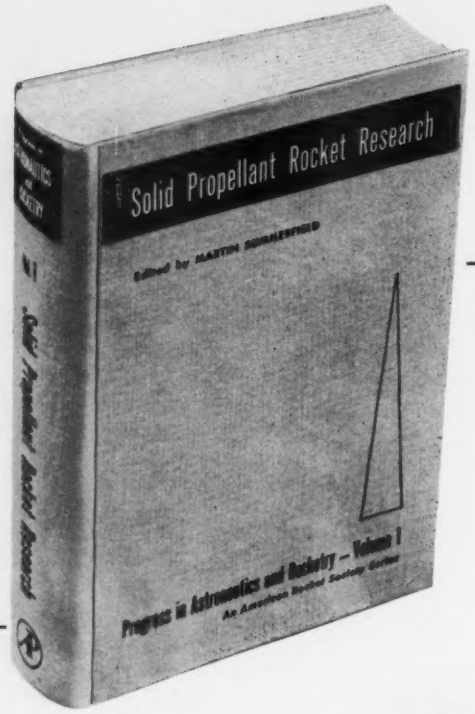

PROGRESS IN ASTRONAUTICS AND ROCKETRY will publish selected papers offered at the specialized symposia of the ARS, together with other papers on the same subject. Beginning with Volume 2, each volume is expected to be published within four months after the papers are received.

At this time, when the quantity of scientific papers is rapidly exceeding the capacities of the customary media in many disciplines, this series presents an important new concept in providing prompt publication combined with convenient concentration of related papers.

Volume 1

Solid Propellant Rocket Research

A Selection of Technical Papers based mainly on a Symposium of the American Rocket Society held at Princeton University, Princeton, New Jersey, January 28, 29, 1960
Edited by MARTIN SUMMERFIELD, *Princeton University*
(Complete contents were given in *ARS Journal*, October 1960, page 927.) *October 1960, 692 pp., illus., $6.50*

Volume 2, 1960

Liquid Rockets and Propellants

Edited by Loren E. Bollinger, Martin Goldsmith, and Alexis W. Lemmon, Jr.
Ohio State University; RAND Corporation; and Battelle Memorial Institute

Volume 3, 1961

Energy Conversion for Space Power

Volume 4, 1961

Space Power Systems

Edited by Nathan W. Snyder, *Institute for Defense Analyses*

Volume 5, 1961

Electrostatic Propulsion

Edited by David B. Langmuir, Ernst Stuhlinger, and J. M. Sellen, Jr.
Thompson-Ramo-Wooldridge, Inc.; Marshall Space Flight Center; and Thompson-Ramo-Wooldridge, Inc.

Orders and requests for information should be sent to ACADEMIC PRESS, rather than to the ARS.

ACADEMIC PRESS New York and London
111 Fifth Avenue, New York 3, New York **17 Old Queen Street, London, S.W. 1**

German Agency: Minerva, G.m.b.H., Holbeinstrasse 25-27, Frankfort am Main
Indian Agency: Asia Publishing House, Nicol Road, Ballard Estate, Bombay 1

Structures Considerations in Design for Space Boosters

PAUL E. SANDORFF[1]

Massachusetts Institute of Technology
Cambridge, Mass.

Structures aspects of the design of space vehicles are studied from the viewpoint of how they influence and are influenced by other technical problems of the space mission. Booster size and configuration are given special attention. It is concluded that structures considerations favor much larger vehicles than those currently contemplated, and that a systems approach to the space effort calls for strong emphasis on the structures contribution.

THE OBJECT of this paper is to describe the ways in which structures problems influence and are influenced by the other aspects of early space vehicle design.

To achieve this aim, the nature of the major loading conditions and how they may vary with vehicle size, configuration and design parameters is first discussed. Structural design methods which are available to support the major vehicle loads are next compared, using structural indexes to assess future design problems. Functional components of the structure are analyzed to determine how weight may vary with vehicle design parameters. Dead weight data available on existent designs are summarized, and the trends noted. Finally, in support of the predictions derived analytically, a family of large booster vehicle designs is presented.

Although at this time all space vehicles are chemical rockets which take off from the surface of Earth, the modular concept of orbital assembly, pilotless rendezvous techniques and orbital refueling may soon provide preliminary steps toward orbital erection and satellite-based, high performance interplanetary vehicles. Such measures are only another form of staging, where the first stage is comprised of multiple ascents of a device of limited size instead of a single large booster, and as such they deserve re-evaluation. A particular objective of this paper therefore is to predict the effect of size increase on the structures aspects of large liquid propellant booster rockets.

System Design and the Structural Requirements

The interrelationship between vehicle design considerations and major structural loading conditions is considered here from the point of view of minimizing structural problems through design.

Ground Loads

Handling requirements may be quite significant to the structural design, and problems of transportation from factory to launch pad have strongly influenced contemporary booster dimensions. A serious venture into space demands re-evaluation of our Earth-side methods and facilities from a systems point of view.

Loads which occur on the launching pad include a ground wind condition, important when the vehicle is supported only at the base. In addition to the static loading, von Kármán vortex excitation can induce the low frequency cantilever bending modes, possibly leading to a fatigue condition (1).[2] Consideration should be given to structural design with external stiffeners which serve as spoilers. The loading condition may not be a source of great concern for vehicles of smaller fineness ratio than contemporary designs.

Thrust Loading

A major portion of the structural weight results from the design condition owing to thrust, which is reacted by inertial loading throughout the vehicle. Maximum acceleration for any stage occurs just prior to burnout and establishes design values for thrust transmitted to forward structure and payload.

In propellant tanks, hydrostatic pressure is the mechanism whereby the fluid is accelerated, and the thrust condition therefore establishes tankage design pressures. In the first stage this pressure component is maximum at the instant of takeoff; for upper stages the hydrostatic loads, like the other thrust loads, will usually be established at booster burnout. Hydrostatic pressure requirements may be raised significantly by dynamic effects arising from longitudinal thrust variations and the symmetrical surging associated with fluid compressibility and tank wall elasticity. An overload factor approaching 2 is possible, especially if the time for acceleration to build up is less than the period of the surging mode. The undamped natural period for this dynamic system in a simple cylindrical tank is approximately (2)

$$T_{n\ \mathrm{surge}} = 2\pi \sqrt{\frac{2}{3}h^2\rho_P \left(\frac{R}{tE} + \frac{1}{2K}\right)}$$

For contemporary applications, this period is already appreciable (0.2 sec for the Saturn booster, for example) compared to the time for thrust buildup at takeoff. In addition to the simple surging overload is the possibility of self-supported dynamic response owing to coupling of pump inlet pressure with engine thrust. In liquid hydrogen tankage, the high fluid compressibility will make surging effects slower and therefore more difficult to control.

Little can be done to reduce the thrust requirements for the booster stage of Earth takeoff vehicles. In fact, slightly

Presented at the ARS 13th Annual Meeting, New York, N. Y., Nov. 17–21, 1958. Revised, August 1960.

[1] Associate Professor, Department of Aeronautics and Astronautics. Member ARS.

[2] Numbers in parentheses indicate References at end of paper.

higher thrust factors might be anticipated as booster size is increased, because larger vehicles generally have larger ballistic coefficients, and drag becomes less important in determining the overall performance optimum. Upper stage thrust loading, however, may be strongly influenced by overall design considerations:

1 Lower burnout acceleration for the previous stage resulting from improvement in specific impulse or the use of multiple staging.

2 The use of low thrust, long duration rocket engines as a better overall compromise with the trajectory penalties due to gravitational losses.

Losses associated with the optimum trajectory diminish in magnitude as the vehicle speed approaches and exceeds orbital velocity. For a liquid propellant rocket operating from orbit, for example, engine mass considerations alone result in a thrust level of perhaps $\frac{1}{3}$ G as the best compromise between the mass ratio penalty of a larger heavier engine and the gravitational loss of a lower thrust, longer duration engine. Vehicles which are to be erected or filled in orbit will strike an even lower compromise thrust level, because this thrust condition will also establish structural mass of the vehicle.

Pressurization

In addition to hydrostatic pressures already mentioned, internal pressure loads may be expected for the following reasons:

1 In tankage structure, for propellant handling purposes.

2 In membrane structure, for stabilization purposes.

3 In cabins of manned vehicles, to provide artificial environment.

4 In cargo and instrument compartments, for functional purposes, such as temperature control.

5 In propulsion system components: Combustion chambers, heat exchangers, piping, etc.

6 In compressed gas storage vessels.

Clearly, space vehicle structure will be largely pressure vessel design.

Flight Loads in Space

Maneuvering and control conditions provide the only external transverse loads of any magnitude. For space operations the time scale can be of such an extent that maneuvering requirements per se will establish only minor loads. Control loads may bear further examination, depending on the functions of the control system, detail problems of control which are not yet clearly defined and the way in which the science may develop to meet them.

One such problem concerns the interaction of propellant sloshing with engine thrust vectoring, vehicle bending and control dynamics (3,4). The natural frequency of the side-to-side sloshing of fluid in a circular cylindrical tank with the free surface more than one diameter above the bottom may be roughly predicted by the formula

$$f_{n\ \text{slosh}} = 1.7\sqrt{n/D}$$

where

n = acceleration factor, Earth G
D = tank diameter, ft

This is an empirical relation based on small scale tests. It indicates extremely low frequencies for the large low acceleration vehicles which might be visualized for interplanetary journeys. The forces involved depend on the mass of the sloshing fluid, and for geometrically similar amplitudes this varies as the cube of the tank diameter (3). Consequently, large size tankage will be possible only if sloshing can be controlled.

This problem may be attacked in several ways; in any case, consideration of all dynamical effects simultaneously, analytically or experimentally, is long overdue (5,6). Nelson (5) has recently demonstrated that the simple pendulum analogy generally used to represent propellant sloshing may be inadequate; sloshing raises the natural frequency and effective damping of structural modes, and drainage of fluid from the tank produces an important negative damping effect on the sloshing phenomenon itself. His work was also directed to provide generalized relations for pressure distribution and system response, on the basis of which pressure pickups and a servo system might be designed to introduce artificial damping of sloshing by out-of-phase thrust vector control. This type of artificial damping is commonly used to reduce overall vehicle bending disturbances, and was first applied in the Vanguard (7).

Control of sloshing would be much easier if the frequency of the vehicle autopilot system could be made low compared to the frequency of the lowest sloshing mode. This can certainly be done while still meeting the trajectory limitations and maneuvering requirements of spaceflight in designs foreseen for chemical rockets. For exotic propulsion schemes which result in very low vehicle acceleration, the interaction of fluid stores with structure and vehicle response may again exert important and as yet unexplored limitations on system design.

Booster Flight Loads

An important design load problem for Earth takeoff rockets is the complex one involving aerodynamic disturbance owing to lateral winds acting on the ascending vehicle and the dynamic response of the vehicle and its control system. A typical design condition stipulates steadily increasing lateral wind (wind shear condition) tending to 150 fps at 40,000-ft altitude, then diminishing; superimposed on this profile is a triangularly shaped spike (jetstream) of an additional 150-fps strength, occupying perhaps 5000 ft of vertical distance in the 30,000- to 40,000-ft altitude zone. It is in this altitude range that maximum dynamic pressure and maximum q/v occur for large liquid propellant rocket boosters; a typical mission for such devices would result in a velocity of perhaps 2000 fps at an inclination 30 to 40 deg above the horizontal at 40,000-ft altitude.

Of primary significance in determining the resultant structural loads is the guidance philosophy. Control of the vehicle flight path may be based on the attempt to hold a constant or programmed attitude with respect to inertial space; even with perfect control, this results in substantial aerodynamic forces. Lower loads and a better trajectory would be obtained with a system which attempts to hold, instead of a specified attitude, a specified flight path. The minimum aerodynamic load is obtained by exercising control with respect to angle of attack (weathercock stability), with, however, considerable trajectory displacement. Geissler (4), in an unusually thorough treatment of this problem, has shown how by obtaining angle of attack information in addition to inertial attitude and by using programmed gain factors, a swivel engine system which is maneuverable with respect to the disturbance may be designed to achieve characteristics varying from "minimum drift control" to "minimum load control," the latter affording significant reduction in structural and control requirements.

Equal in importance in determining structural loads is the capability of the control system, for if it is marginal in capacity or in speed of response, high structural loads and even divergence may result. But practical problems limit the control system design: Favorable aerodynamic characteristics usually entail compromises and weight penalties, as does actuator capability. Control system dynamical response is limited by structural vibratory modes, which the gyro and accelerometer sensors confuse with rigid body motion. To avoid coupling effects which may result in saturation or instability, the lower modes may be damped by phase shifting of thrust response

(7), high frequency signals blocked with filtering networks, and the vehicle autopilot response consequently held to perhaps a fifth of the fundamental body bending frequency. There is little doubt, however, that this ratio can be improved, with greater sophistication in control system design, for example, by employing multiple sensors or strain gage networks which permit identification and rejection of the effects arising from structural deformation.

How are the control system requirements affected by size and shape of the booster? For large boosters these requirements are established chiefly by the jetstream, which the vehicle following a reasonable trajectory passes through in perhaps 5 sec regardless of size. Assuming vehicle pitch angle to be kept small compared to the angle of attack, the total moment impulse developed by the aerodynamic disturbance is

$$\int M_{\text{aero}} d\tau = \int C_{m_\alpha} \frac{u}{v} \left(\frac{\rho}{2} v^2\right)\left(\frac{\pi}{4} D^2\right) (kL) d\tau$$

For cone bodies the coefficient C_{m_α} varies slightly with L/D, giving some incentive for lower fineness ratio, that will be disregarded for the time being. Adopting C_{m_α} as invariant on the basis indicated and using k to indicate proportionality, the aerodynamic input over any selected time increment varies among similar vehicles as

$$\int M_{\text{aero}} d\tau = kD^2L \int \frac{u}{v} v^2 d\tau$$

The rate of response required of similarly effective control systems will be determined by the rate of pitch which the vehicle develops, for if it pitches at a slow rate, the corrective maneuver may also be accomplished leisurely—assuming always that the total excursion will not be permitted to be large. Making an approximation for the instantaneous vehicle moment of inertia

$$I_{\text{veh}} = kW_P L^2 = k\rho_P D^2 L^3$$

the minimum required natural frequency of the vehicle autopilot system is seen to vary as

$$f_{\text{control, min req.}} = k \frac{\int M_{\text{aero}} d\tau}{I_{\text{veh}}} = \frac{k}{\rho_P L^2}$$

where the quantity $\int (u/v) v^2 d\tau$ has been assumed invariant for vehicles following similar trajectories and exposed to similar aerodynamic disturbances. In large vehicles, therefore, the control system may operate much more slowly and still maintain control.

The problem of interaction of the control system with structural modes depends on whether vehicle bending frequencies are similarly reduced. For clustered tank designs, the bending rigidity is unusually low, and a worsening of the situation can be avoided only by accepting sizable weight penalties. Assuming that single cylindrical shell tankage is to be used, the overall structural bending frequency may be assumed to vary roughly as

$$f_{\text{veh bend.}} = k\sqrt{EI_{\text{shell}}/W_P L^3}$$

If the structural weight fraction for the shell is to remain the same among the vehicles considered, that is

$$\frac{W_s}{W_P} = \frac{k\rho_s DLt}{W_P} = \text{constant}$$

the shell moment of inertia may be estimated as

$$I_{\text{shell}} = k \frac{W_P}{\rho_s} \frac{D^2}{L}$$

Substituting back in the frequency relation with the material properties E/ρ_s considered constant

$$f_{\text{veh bend.}} = kD/L^2$$

In comparison with the control frequency relation, it must be expected that increase in vehicle diameter will relieve the problem of interaction between structural modes and autopilot. Such an effect appears inescapable as the gross size of vehicles is increased. Reduction in propellant density, however, shifts the required control frequency up into the range of frequencies of structural modes.

The magnitude of the control deflection necessary to avoid exceeding any specified pitching response is established by the requirement that the system provide an impulse sufficient to overcome the aerodynamic input. The available control impulse will vary approximately as

$$\int M_{\text{cont}} d\tau = \int k n_i W_i \beta d\tau = k n_i \frac{W_i}{W_P} \rho_P D^2 L \int \beta d\tau$$

Equating to $\int M_{\text{aero}} d\tau$ and solving

$$\int \beta d\tau = k \frac{1}{n_i} \frac{W_P}{W_i} \frac{1}{\rho_P} \int \frac{u}{v} v^2 d\tau$$

In the wind-shear type of disturbance, the control response will keep up with the aerodynamic input, showing a lag which could be used as a measure of effectiveness. Among equally effective systems the required control deflection is therefore determined by the instantaneous aerodynamic angle of attack u/v, and since this will vary in time about the same for all vehicles, timewise integration of the preceding relation leads to time factors on both sides which are proportionate to each other. Then

$$\beta = k \frac{1}{n_i} \frac{W_P}{W_i} \frac{1}{\rho_P}$$

For indicial disturbances, however, the aerodynamic impulse integrates over a fixed time scale, whereas the control impulse integrates over a period which was found to vary as $\rho_P L^2$. In this case the maximum required control deflection will vary for different vehicle sizes and shapes approximately as

$$\beta_{\text{max req.}} = k \frac{\frac{1}{n_i} \frac{W_P}{W_i} \frac{1}{\rho_P}}{\rho_P L^2} = k \frac{1}{n_i} \frac{W_P}{W_i} \frac{1}{\rho_P^2 L^2}$$

Since the control system period increases with L^2, it is conceivable that for very large vehicles even the jetstream disturbance may be considered an indicial input.

In summary, large vehicles will be sluggish in motion, but it appears that the control system problem will actually be alleviated by increase in vehicle size. This result is in accord with an earlier demonstration by Hebeler (8) based on a study of related designs of size ranging from 10^5 to 10^6 lbm gross, which were "flown" through a synthetic design wind profile on a computer to obtain the maximum pitch angle vs. gross weight; the conclusion reached was that very large booster vehicles will go through the most severe aerodynamic disturbance "like the Queen Mary."

Propellant sloshing, which has been discussed in the foregoing, is of considerable concern in contemporary boosters, because sloshing frequencies vary over a range which approaches and may bracket the value that other considerations dictate for the vehicle autopilot system (3,4). However, sloshing frequencies vary approximately as $1/\sqrt{D}$, whereas, as has been seen, the required vehicle autopilot natural frequency varies approximately as $1/L^2$. Consequently the problem of dynamic interaction is expected to diminish as the two frequencies diverge in very large boosters. Active damping measures may then serve to control incidental sloshing, such as properly phased thrust vector control as

previously suggested, or some other wave or circulation-producing system.

This reasoning is based on a study of propellants of density similar to those in use today. The effect of propellant density ρ_P enters in all the relations derived here in such a way as to make the problems much more serious when designing tankage for the low density liquid hydrogen.

In summary, booster flight loads are seen to be only a part of the overall system response, subject to extremely involved design compromise and especially dependent upon the ability and courage of the control system engineer. With a bold and coordinated approach, it appears that problems arising from coupling of structural and sloshing modes with the control system can be reduced in severity and conquered by sophisticated design.

Environmental Conditions

The forward surfaces of Earth takeoff rockets suffer some aerothermal effects which produce relatively modest structural design problems. Re-entry problems are in a separate category, and have been widely treated, for example, (9).

The environment of space is a topic which currently is of strong interest to structures and materials engineers (10,11). The ultra-hard vacuum which applies above a thousand miles altitude cannot at present be duplicated on Earth; from such experiments as can be conducted it is known that the surface properties of materials, which include crack propagation and fatigue characteristics, may be strongly affected by vacuum. These properties are especially significant in the design of pressurized thin shells and may govern structural weight and reliability. Ionizing radiation, chiefly that of solar origin, will have a detrimental effect on the stability of structural and other properties of plastics and organic materials. Although incident radiation is itself of negligible consequence in the behavior of metals, when in combination with hard vacuum it may hasten or influence the changes which occur in surface characteristics. Finally, by their combined influence, radiation and vacuum may affect surface emissivity, destroying radiative thermal control and leading to detrimental temperatures.

Damage by meteoritic particles constitutes a major environmental hazard which has received attention with regard to identification of the environment (12,13), nature of the damage mechanism (14) and protective design (12,15). However, none of these studies can yet be applied with engineering accuracy. The state of the problem is nicely summarized by Gazley and Bjork (16): "The probability of damage to space vehicles....has appreciable uncertainty because of the difficulty of estimating meteoroid mass and frequency. The results indicate, for example, that a surface 1 meter square and 1 millimeter thick will be punctured sometime between 7 weeks and 620 years."

In summary, the interaction of structures and environment will exert a major influence on the progress and the cost of spaceflight, since it is evident that solution of the environmental problems could involve a doubling or tripling of the dead weight ratio as a result of provision for shielding, meteor protection and fail-safe design. As yet, however, the requirements are undefined, measures to meet them are hardly begun, and an effort at quantitative prediction is premature.

Structural Forms and the Vehicle Design

Loading Density

Requirements for the containment of large volumes under pressure and the simultaneous transmission of vehicle loads establish thin pressurized shells as the dominant structural form. Conventional aircraft shell structure of monocoque or semimonocoque design represents one method of supporting the thrust and bending loads, which is appropriate when the internal pressure is a minor factor. In the other extreme, the pressure itself may be used as the medium which supports the overall compression and bending, with the shell acting chiefly as a membranous container. Successful pressure stabilized structures date from the all-metal dirigible of 1929 (17) and include many contemporary examples. In many other cases, internal ullage pressure will support a part of the overall axial load or bending moment, leaving the balance—as well as the hoop tension loads—to be carried by the shell itself. Which type of structure is most efficient depends on load, size and shape, all at once.

In approaching such a design problem, the structures engineer often makes use of the "structural index" (18). The governing structural indexes for the three major load-carrying functions under consideration here are:

Axial load	$P/\pi R^2$
Bending	$2M/\pi R^3$
Internal pressure	p

The value of the structural index is indicative of the density of the structure required, and because material properties permit only limited freedom in this regard, the structural index usually determines the fabricational form which corresponds to minimum weight. The structural indexes selected here place all three types of loading on a unified basis, namely, equivalent internal pressure.

The way in which the values of these structural indexes vary with the vehicle design parameters of ρ_p, W_P and L/D has been derived in Table 1 for the major types of imposed loads. The assumptions on which each is based, also noted in Table 1, follow from considerations of the previous section; these assumptions are simplified but realistic.

Design Capability

The price in structural weight which the engineer must pay to meet these requirements is expressed graphically by employing the analytical theory of optimum design, as in Figs. 1 and 2. Allowable strength data for conventional stiffened shell structure have frequently been cast into such a form [for example (19 and 20)]. It is also possible to include data for pressure stabilized shell structure as well. The ordinate for these curves is a weight parameter $\rho_s \bar{t}/R$, where $\bar{t}$ is the thickness of a simple unstiffened shell of the same weight (equal to the thickness if pressure stabilized), ρ_s is the material density and R the shell radius. The abscissae are the structural indexes $P/\pi R^2$ and $2M/\pi R^3$; these parameters will be recognized as being equal to the stabilization pressure that would be required for a shell with no inherent stiffness.

In constructing these charts the strength data for unpressurized shells were based on (20), which is somewhat more conservative than (19); the performance of simple monocoque structure and of pressure stabilized shells was based on (21 and 22), with the allowable hoop stress limited to 85 per cent of the material tensile yield stress. The figures apply directly to 7075-T6 material, but the effects of other materials may be estimated by introducing their properties into the ordinates, as is indicated, for example, in (19). The curves for pressure stabilized shells of austenitic stainless steel of 200,000 psi yield strength are conservatively predicted by those for 7075-T6.

From a cursory study of Figs. 1 and 2 it may be concluded that for low values of the structural index (low loads, large dimensions) pressure stabilized structure has a significant weight advantage. For high values (concentrated loading) conventional stiffening is optional. However, when pressure is to be carried in addition to axial or bending load, longitudinal stresses in the conventional stiffened structure are relieved, and the effect is to reduce the design value of the structural index by the magnitude of the ullage pressure

$$(P/\pi R^2)_{\text{effective}} = (P/\pi R^2)_{\text{actual}} - p_{\text{ullage}}$$
$$(2M/\pi R^2)_{\text{effective}} = (2M/\pi R^2)_{\text{actual}} - p_{\text{ullage}}$$

These effective values of structural index and the correspondingly lower weight parameters for the stiffened-and-pressurized design indicate the possibility of a weight advantage over a limited range. The resultant design, of course, must not be inadequate under the simultaneously applied hoop tension.

With respect to the gas pressure storage problems, the structural indexes contain the storage vessel dimension r which can usually be adjusted to exploit material properties to the utmost.

Significance of the Analysis

This presentation of structural performance in terms of structural parameters is not meant to serve in place of a stress analysis. Its purpose is to express the requirements and the capabilities in gross terms, a form more immediately meaningful to the designer.

What does the analysis signify with regard to future problems of the space vehicle designer? Several conclusions may be drawn from Table 1:

1 The effect of size on the structural indexes is slow, but a definite increase with size is unavoidable.

2 The effect of slenderness ratio is mixed, and changes in L, D will therefore lead to new design compromises.

3 The effects of propellant density and of acceleration factor are large, and the reductions which will occur in these quantities with the use of liquid hydrogen propellant and space-based vehicles will lead to much smaller structural indexes.

Figs. 1 and 2, however, clearly show that, thanks to pressure stabilization methods in the usually troublesome low range, the designer is well prepared to meet any foreseeable loading condition with structures that utilize the available properties of materials in an efficient manner.

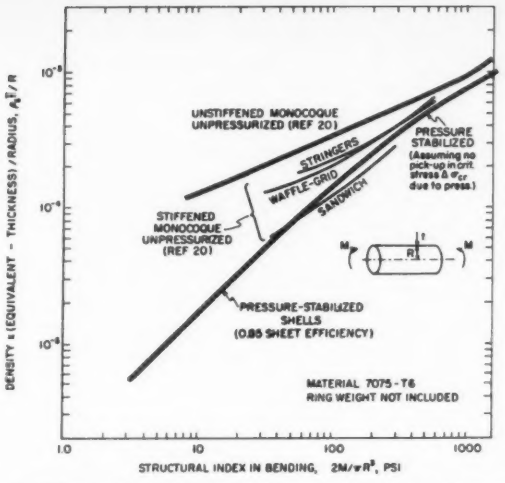
UNSTIFFENED MONOCOQUE UNPRESSURIZED (REF 20)
STRINGERS
WAFFLE-GRID
SANDWICH
PRESSURE STABILIZED (Assuming no pick-up in crit. stress Δ σcr due to press.)
STIFFENED MONOCOQUE UNPRESSURIZED (REF 20)
PRESSURE-STABILIZED SHELLS (0.85 SHEET EFFICIENCY)
MATERIAL 7075-T6
RING WEIGHT NOT INCLUDED
DENSITY × (EQUIVALENT - THICKNESS) / RADIUS, $\rho_s \bar{t}/R$
STRUCTURAL INDEX IN BENDING, $2M/\pi R^2$, PSI

Fig. 1 Structural efficiency of shells in bending: Optimum pressure stabilized structure compared with optimum conventional aircraft construction

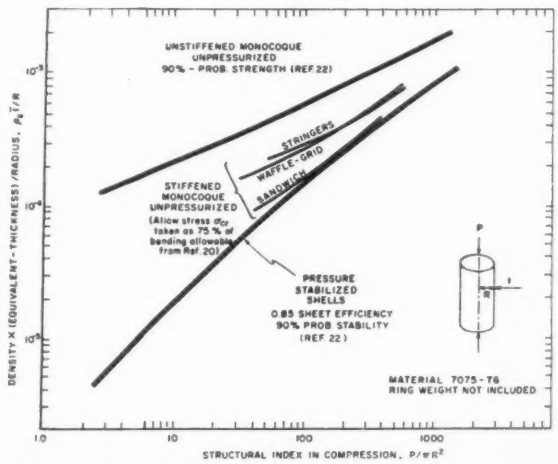

Fig. 2 Structural efficiency of shells in compression: Optimum pressure stabilized structure compared with optimum conventional aircraft construction

Structural Weight and the Vehicle Design

Bossart (3) has presented a study of the effect of gross size on the dead weight ratio of geometrically similar rocket vehicles. Without making extensive and detailed studies, it is possible to present only a few new considerations, some of which were suggested by Bossart, namely, the effects of variation in shape or fineness ratio (L/D) of the vehicle and the effect of propellant density. It is possible also to resort to empirical data, in which case the effect of a continuously advancing technology must be recognized.

Variation of Component Weight With Configuration and Size

Following essentially the same approach as (3) by considering structural weight to be comprised of separable provisions against several different major types of loading, and making simplified statements concerning the effect of basic vehicle proportions and sizes on these structural requirements, the structural weight ratios of Table 1 may be derived. The propellant mass is seen to be the natural normalizing factor for most of the weight allowances (a few depend on gross mass, but the propellant loading factor is relatively inflexible for a given mission). In general, each weight ratio is roughly proportional to the material strength-density ratio, the loading severity and some function of the vehicle parameters W_P, L/D and ρ_P.

Assuming similitude of loads, materials, design efficiency and fabrication, the effects of vehicle design are seen to be as follows:

1 The weight factors allocated for all structure designed by longitudinal thrust, and that designed by bending under maximum control system deflection, vary as the one-third power of the stage propellant mass W_P. None of the other structural weights is influenced directly by size increase.

2 A decrease in the fineness ratio causes large reductions in the weight allocation for material designed by bending, and somewhat smaller reductions in that applying to longitudinal thrust structure, tank bottoms excepted. Tank ends suffer with a decrease in fineness ratio. A design compromise appears possible which would permit offsetting the weight penalties of increased gross size with a reduction in fineness ratio.

3 A decrease in propellant density affects all weight factors adversely, except pressure storage vessels. Structures critical under tank ullage pressure and aerodynamic loading are affected inversely as the first power of the propellant density, whereas factors for thrust and hydrostatic structure vary only inversely as the one-third power; therefore liquid hydrogen tankage should be designed for low internal pressure and small fineness ratio.

4 A decrease in acceleration factor will bring numerous decreases in component weights.

Table 1 Effect of vehicle design parameters on loading indexes and weight ratios of structural components. $W_P = k\rho_P D^2 L$ assumed. The factor k indicates proportionality

Provision	Assumptions			Structural Index	Structural Weight Ratio W_s/W_P
	Design Requirement	Allowable Strength	Weight Estimation		
Longitudinal Thrust Structure					
Mat'l in Axial Compression	$P_{des} = k\, n_i\, W_i$	$P_{allow} = k\, F_a\, Dt$	$W_s = k\rho_s\, D\, L\, t$	$\frac{P}{\pi R^2} = k\, n_i \frac{W_i}{W_P} \rho_P^{\frac{2}{3}} \left(\frac{L}{D}\right)^{\frac{2}{3}} W_P^{\frac{1}{3}}$	$k\,(f.s.)\frac{\rho_s}{F_a}\, n_i \frac{W_i}{W_P}\, W_P^{\frac{1}{3}} \left(\frac{L}{D}\right)^{\frac{2}{3}} \rho_P^{-\frac{1}{3}}$
Mat'l Carrying Hydro. Press.					
Cylindrical Sections	$P_{des} = k\, n_i\, \rho_P\, L$	$P_{allow} = k\, F_t\, t/D$	$W_s = k\rho_s\, D\, L\, t$	$p = k\, n_i\, W_P^{\frac{1}{3}} \rho_P^{\frac{2}{3}} \left(\frac{L}{D}\right)^{\frac{2}{3}}$	$k\,(f.s.)\frac{\rho_s}{F_t}\, n_i\, W_P^{\frac{1}{3}} \left(\frac{L}{D}\right)^{\frac{2}{3}} \rho_P^{-\frac{1}{3}}$
Tank Bottoms	$P_{des} = k\, n_i\, \rho_P\, L$	$P_{allow} = k\, F_t\, t/D$	$W_s = k\rho_s\, D^2 t$	$p = k\, n_i\, W_P^{\frac{1}{3}} \rho_P^{\frac{2}{3}} \left(\frac{L}{D}\right)^{\frac{2}{3}}$	$k\,(f.s.)\frac{\rho_s}{F_t}\, n_i\, W_P^{\frac{1}{3}} \left(\frac{L}{D}\right)^{-\frac{1}{3}} \rho_P^{-\frac{1}{3}}$
Transverse Vehicle Bending					
Aerodynamic Criterion	$M_{des} = k\,(C_{m_\alpha})D^2 L$	$M_{allow} = k\, F_a\, D^2 t$	$W_s = k\rho_s\, D\, L\, t$	$\frac{2M}{\pi R^3} = k\,(C_{m_\alpha})\frac{L}{D}$	$k\,(f.s.)\frac{\rho_s}{F_a}\,(C_{m_\alpha})\frac{L}{D}\,\rho_P^{-1}$
Control System Criterion	$M_{des} = k\,(n_i W_i)\beta\, L$	$M_{allow} = k\, F_a\, D^2 t$	$W_s = k\rho_s\, D\, L\, t$	$\frac{2M}{\pi R^3} = k\, n_i \frac{W_i}{W_P} \beta\, W_P^{\frac{2}{3}} \rho_P^{\frac{2}{3}} \left(\frac{L}{D}\right)^{\frac{5}{3}}$	$k\,(f.s.)\frac{\rho_s}{F_a}\, n_i \frac{W_i}{W_P} \beta\, W_P^{\frac{1}{3}} \left(\frac{L}{D}\right)^{\frac{5}{3}} \rho_P^{-\frac{1}{3}}$
Pressure Carrying Structure					
Prop. Tank Ullage Pressure					
Domes	$P_{des} = k$	$P_{allow} = k\, F_t\, t/D$	$W_s = k\rho_s\, D^2 t$	$R = k$	$k\,(f.s.)\frac{\rho_s}{F_t} \left(\frac{L}{D}\right)^{-1} \rho_P^{-1}$
Cylindrical Sections	$P_{des} = k_1 - k_2\, \rho_P L$	$P_{allow} = k\, F_t\, t/D$	$W_s = k\rho_s\, D\, L\, t$	$p = k_1 - k_2\, W_P^{\frac{1}{3}} \rho_P^{\frac{2}{3}} \left(\frac{L}{D}\right)^{\frac{2}{3}}$	$k_1\,(f.s.)\frac{\rho_s}{F_t}\left[\rho_P^{-1} - k_2\, W_P^{\frac{1}{3}} \left(\frac{L}{D}\right)^{\frac{2}{3}} \rho_P^{-\frac{1}{3}}\right]$
Prop. Tank Press. Storage	$(pr^3)_{des} = k\, W_P/\rho_P$	$P_{allow} = k\, F_t\, t/r$	$W_s = k\rho_s\, r^2 t$	$p = k\, W_P/\rho_P r^3$	$k\,(f.s.)\frac{\rho_s}{F_t}\, \rho_P^{-1}$
Engine Act. Press. Storage	$(pr^3)_{des} = k\, n_i\, W_i$	$P_{allow} = k\, F_t\, t/r$	$W_s = k\rho_s\, r^2 t$	$p = k\, n_i \frac{W_i}{W_P} W_P/r^3$	$k\,(f.s.)\frac{\rho_s}{F_t}\, n_i \frac{W_i}{W_P}$

Empirical Variation in Body Weight With Size

The present open-literature picture of the state of the art in structural design for liquid propellant rockets is summarized by Fig. 3, where the body weight ratio is plotted against stage propellant weight W_P for a number of contemporary vehicles (23). [The body weight ratio is defined as the ratio of structure-plus-engine mass to propellant mass $(W_s + W_E)/W_P$, and does not include residual propellants or fixed-weight items, such as guidance and control equipment.] It is evident that the larger size vehicles offer a great advantage in structural efficiency, and that the trend appears to continue up to the largest devices currently visualized.

This observed trend is in contrast with (3 and 24), which indicate that, as size increases above present-day applications, the structures and engine weight fractions will increase. Conservative predictions must assume uniformity of design philosophy and geometric similarity overall or in detail, whereas in actuality the structure will vary in nature and in shape to suit an optimum overall compromise with all aspects of the design problem. Structures engineers have never resigned themselves to the law of squares and cubes. Moreover, such conservative predictions ignore a very real influence which the more generous research and development budget for a large device has upon the mean level of efficiency obtained in the end product.

An additional quantity affecting the nature of this chart is that, in general, the larger devices have been developed more recently in history and benefit from advances in the general state of the art. It is dangerous to extrapolate technological advance but unrealistic to ignore it.

Effect of Structural Weight on Vehicle Design

The importance of large size booster rockets in the space effort is now well recognized. Fig. 3 indicates that ambitious projects will also be rewarded with exceptional structural efficiency. This effect would be extremely significant to the overall performance of a device such as the V-2, which had a payload ratio of 0.08 and a body weight ratio of 0.30. But in contemporary booster designs the values may be reversed, and then the improvement in payload owing to structural weight saving, particularly weight saving in the booster, is marginal. Instead of exploiting structural efficiency directly, it may be more attractive to effect a tradeoff with such other desirables as reliability, economy of construction and recovery provisions.

One such alternative may be a reduction in the number of stages to perform a given mission. The primary function of staging, with its almost direct increase in complexity, cost and unreliability, is to avoid the penalty which is incurred by only a few per cent of structural weight. A representative example is summarized in Table 2, where for a typical mission the ratio of gross takeoff mass to payload mass is tabulated for three-stage and two-stage satellite launching rockets of several different sizes, assuming body weight ratios given in Fig. 3, with appropriate allowance for residual and fixed mass as indicated. The results, although idealistic, demonstrate that when gross size is increased by an order of magnitude, a mission formerly requiring three stages can probably be done with only two.

Low structural mass fractions, furthermore, result in a notable reduction in sensitivity of the overall performance to staging proportions, and therefore add versatility to the attributes of very large boosters. Fig. 4 illustrates this effect in a two-stage rocket booster, designed to furnish an ideal velocity of 20,000 fps—suitable for launching a third-stage satellite or escape vehicle. For several different dead weight ratios, overall payload ratio is plotted against the staging proportions, the latter being measured by the first-stage mass ratio MR_1 normalized with respect to the mean mass ratio $\sqrt{MR_0} = \sqrt{MR_1 MR_2}$. (A value of 1.0 for the parameter $MR_1/\sqrt{MR_0}$ means that the mass ratios of first and second stages are identical.) Propulsion performance used in the examples is roughly representative of combinations of Lox/RP-1 and Lox/hydrogen systems, with allowance for altitude effects.

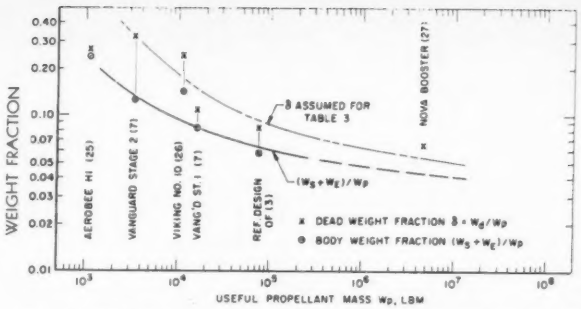

Fig. 3 Effect of vehicle size on body weight for Earth takeoff rockets using conventional liquid propellants

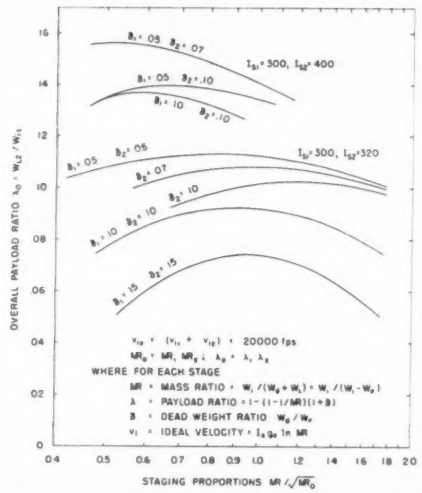
OVERALL PAYLOAD RATIO $\lambda_0 = W_{L2}/W_{L1}$
STAGING PROPORTIONS $MR_1/\sqrt{MR_0}$
I_{s1} = 300, I_{s2} = 400
I_{s1} = 300, I_{s2} = 320
$v_{i0} = (v_{i1} + v_{i2}) = 20000$ fps
$MR_0 = MR_1 MR_2$; $\lambda_0 = \lambda_1 \lambda_2$
WHERE FOR EACH STAGE
MR = MASS RATIO = $W_i/(W_e + W_L) = W_i/(W_i - W_p)$
λ = PAYLOAD RATIO = $1-(1-1/MR)(1+\beta)$
β = DEAD WEIGHT RATIO W_e/W_p
v_i = IDEAL VELOCITY = $I_{s_i} g_0 \ln MR$

Fig. 4 Effect of dead weight ratio on staging optimization for two lower stages of a satellite launcher

Table 2 Two-stage vs. three-stage satellite launcher performance
(Based on dead weight estimates δ vs. W_P of Fig. 3)

Initial mass at takeoff W_i, lbm →	10^5	10^6	10^7
Initial mass/payload in orbit, $1/\lambda_0$			
three-stage vehicle	90	40	35
two-stage vehicle	140	50	40

Assumptions

$$I_{s1} = 300 \text{ sec}$$

$$I_{s2} = I_{s3} = 320 \text{ sec}$$

$$(v_i)_0 = (v_{i1} + v_{i2}) = 32{,}000 \text{ fps}$$

where for each stage

$$\lambda = 1 - (1 - 1/MR)(1 + \delta)$$

$$v_i = I_s g_0 \ln MR$$

Overall payload ratio $\lambda_0 = \lambda_1\lambda_2\lambda_3$ maximized by adjusting staging proportions.

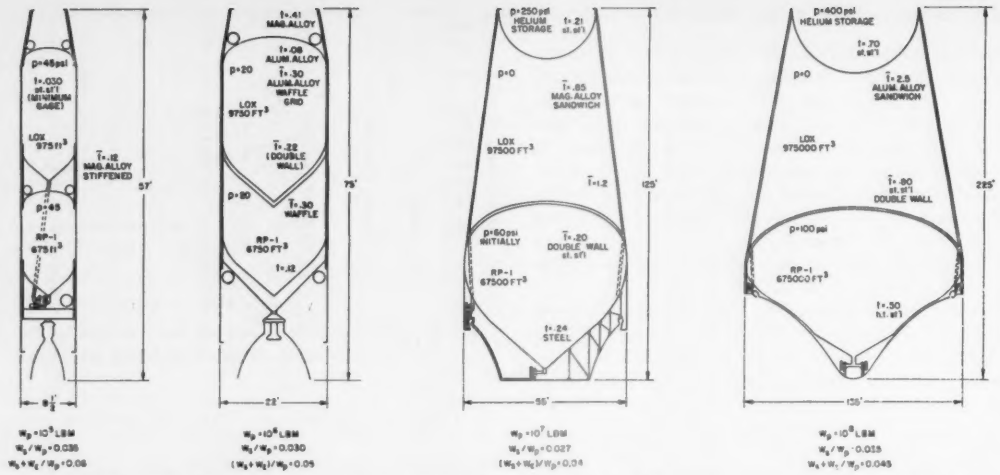

Fig. 5 Family of large booster structures (designed for thrust $F = 2W_P$ approximately 10 deg misaligned)

Clearly, first-stage booster vehicles of low structural weight may be utilized to carry a wide range of off-optimum payloads with small sacrifice in performance, whereas a large dead weight fraction will amount to a restriction in utility as well as a direct performance penalty.

System Design vs. Structures

The evidence is strong that the dead weight fraction for liquid propellant rockets should go down, not up, with size increase. Dead weight is, currently, the primary reason for staging and for carefully optimized staging proportions. In a space systems design the structures contribution must be recognized and exploited, and this means much larger vehicle sizes and fewer units than are usually considered feasible for chemical rockets.

Representative Booster Designs

As an example of the effects of size on structure and of structural problems on configuration, a series of cursory designs for single-shell booster vehicles was made, covering the range from 10^5- to 10^8-lb propellant mass. Fig. 5 presents the results of these design studies and indicates trends which may be expected for such vehicles. Each design is the result of a number of trials and represents a degree of refinement, insofar as the depth and limitations of the study permit.

Conservative methods and assumptions were followed in developing these designs, and the stipulated loadings were met with factors of safety of 1.25 and 1.50, respectively, for unpressurized and pressure-carrying structures. This factor of safety requirement, together with the conservatism of Figs. 1 and 2 regarding the weight of pressure stabilized shells,

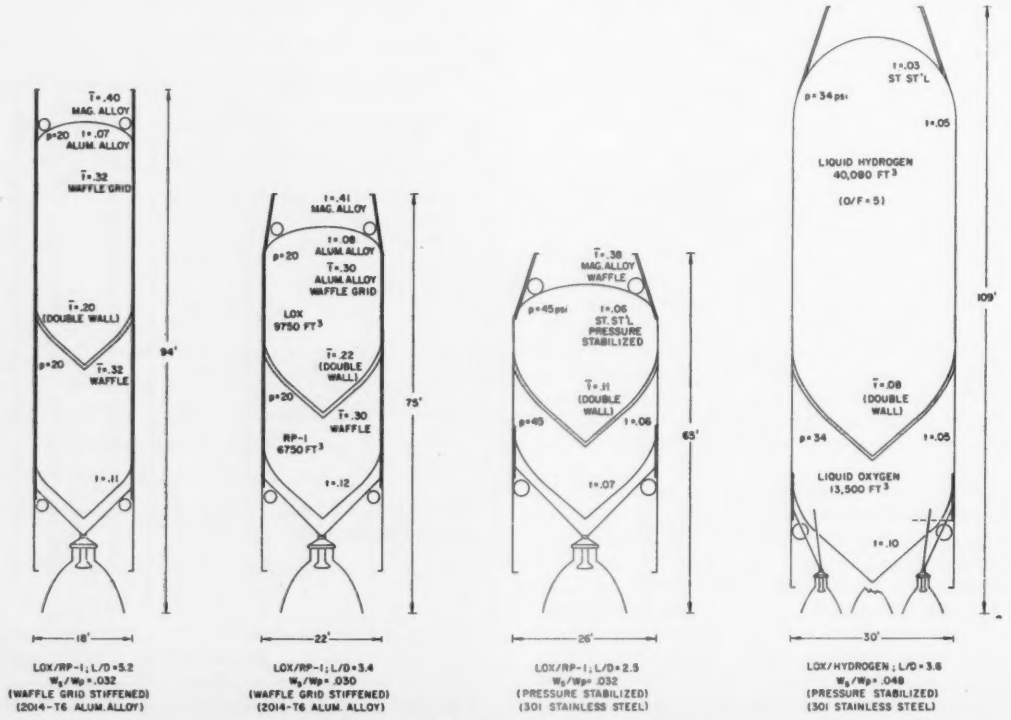

Fig. 6 Comparison of different configurations for 10^6-lb boosters

Table 3 Structural weight estimates for booster designs of Figs. 5 and 6

Propellant mass W_P, lbm	10^5	10^6				10^7	10^8
Propellant	Lox/RP-1	Lox/RP-1			Lox/hydrogen	Lox/RP-1	Lox/RP-1
Booster length, ft	57	94	75	65	109	125	225
Booster diameter, ft	$8\frac{1}{2}$	18	22	26	30	55–35	135–80
Ullage pressure, psi	45–45	20–20	20–20	45–45	34–34	0–60	0–60
Applied axial load for shell, lb	2×10^5	2×10^6	2×10^6	2×10^6	2×10^6	2×10^7	2×10^8
Applied bending stress, % of applied compression stress	85	75	75	75	75	50	33
Design axial load equivalent to combined axial and bending stress	3.28×10^5	3.13×10^6	3.13×10^6	3.13×10^6	3.13×10^6	2.75×10^7	2.5×10^8
Tankage weight, lbm							
Longitudinal shells, axial plus pressure loads	670	15,400	10,500	3800	6900	107,000	1,550,000
Tank bottoms, pressure loads only	296	3370	4990	8200	11,600	81,000	1,234,000
Domes, ullage pressure only	225	760	1130	1820	1760	...	...
Other structure weight, lbm							
Longitudinal shells: Interstage, aft struct.	810	5380	6400	7750	8100	27,700	87,000
Engine mount and skirt	340	1770	2320	2820	3050	15,000	80,000
Miscellaneous plus 5% contingency	300	2450	2400	2490	3250	21,200	240,000
Ullage pressure storage system weight, lbm	900	2500	2500	5500	13,600	19,800	350,000
Total structural weight, lbm	3541	31,630	30,240	32,380	48,260	271,700	3,541,000

Factor of safety 1.50 on pressure loads; 1.25 on other loads. Longitudinal loads based on thrust $F = 2W_P$; superimposed bending stress corresponds to about 10-deg thrust misalignment.

predisposes the larger designs to stiffened-shell structure.

Weight calculations based on these studies support Fig. 3 out to 10^7 lbm. For the 10^8-lbm design the structural weight fraction is greater than that for the 10^7-lbm vehicle. The difference is not so large as to discourage more thorough study and consideration.

A typical crossplot is shown in Fig. 6, where a number of 10^6-lbm boosters of different L/D are compared. The weight breakdown for these designs, given in Table 3, substantiates the detail trends predicted by Table 2. The overall result, however, indicates a surprisingly slow variation in total weight fraction with L/D for the range investigated. The other studies did not permit a similar observation, the 10^5-lbm booster design being constrained by minimum gage considerations, and the larger vehicles by engine size and tankage shape problems.

Fig. 6 also presents, for comparison, a design using liquid hydrogen fuel, at a compromise oxidizer to fuel mixture ratio of 5. About three times larger in volume than the oxygen-kerosene rocket of the same mass, the structure shows 60 per cent increase in weight. This result is in accordance with Table 1, considering that most of the structure carries longitudinal and hydrostatic loads and its weight would vary as $\sqrt[3]{\rho_P}$ if the material could be utilized with equal efficiency. Pressure stabilization makes this roughly possible.

In a study of this type it is not possible to anticipate the ingenuity of the design engineer, who by combining functions and rearranging configurations may gain a notable advantage. It is presumed that many technological advances will be achieved, however, for the larger devices in the family: Thrust damping of propellant sloshing, ullage pressure control, pressurized interstage structure, double-wall tank bulkheads with internal pressure, hot gas pressurization systems, and the plug nozzle, to transmit engine thrust directly into the tankage, eliminating the tortuous load path that is tolerated in contemporary vehicles.

Conclusions

It appears that, at present, structures place no bounds on the size of rocket vehicles, and in fact favor much larger devices than are presently contemplated in our space program. Dynamic problems arising from the interaction of structural deformation, fuel sloshing modes and the control system will probably constitute the area of greatest technical difficulty associated with new, unusual and structurally efficient designs. From the crude analysis presented here, it appears that on the whole these problems may be relieved with increase in size. Despite this possibility, an advance is needed in controls systems to provide isolation and active damping measures.

Many advances have been made since the day of von Pirquet. Mammoth booster vehicles, such as those studied here could establish large lunar and interplanetary missions not only without requiring orbital assembly, but probably at reduced total cost, and certainly much earlier in historical time.

The structural problems of large space vehicles employing thin wall tankage will be much the same as those for today's boosters, differing chiefly in the values of the design parameters. Efficient methods of approaching these new design problems have already been established, although the degree of efficiency can undoubtedly be improved. There remain a number of questions concerning environmental effects, however, which cannot be treated quantitatively at this time. The recent NASA Technical Note D-518 (10) describes in detail what would be necessary to approach these problems with assurance and competence.

Actually it is not necessary that the structures engineer be well equipped for this task. The alternative is greater structural weight in order to obtain a prescribed confidence level. For a given mission, this requires either more complex staging, a design approach which must face up to more severe relia-

bility limitations and mission cost, or improved propulsion performance, which again can be measured in cost and time. The possibility of a bold structures approach contributing to the overall performance of new design is in danger of being overlooked under the pressure of meeting contemporary problems with conventional methods. In brief, structures technology is not a stationary science, and the conquest of space can progress better, faster and more economically when founded on coordinated advances in all fields.

Acknowledgment

The author gratefully acknowledges the influence of L. K. Petersen of Aerojet-General Corp., who made early studies of the application of membrane-structure in very large vehicles, Milton Rosen and his group at NASA, at whose encouragement the parametric studies were initiated, and Messrs. Robert Shorey of Convair-Astronautics, Richard Heldenfels of NASA and Norris Dow of General Electric Co., who furnished valuable help and criticism.

Nomenclature

C_{m_α} = slope of aerodynamic moment coefficient
D = diameter of vehicle
E = modulus of elasticity
F_a = allowable stress
I_s = specific impulse, lbf-sec/lbm
I_{veh} = mass moment inertia vehicle, slug-ft^2
I_{shell} = section moment inertia shell, in.^{4}
K = bulk modulus of fluid, psf
L = length of vehicle
M = bending moment
MR = mass ratio = W_i/W_b
P = longitudinal thrust load, lbf
R = radius of tank, in.
T_n = natural period, sec
W_i = initial gross vehicle mass = $W_b + W_P$, lbm
W_P = useful propellant mass, lbm
W_b = burnout mass = $W_L + W_d$, lbm
W_L = payload mass, lbm
W_d = "dead weight" mass = $W_s + W_E + W_r$, lbm
W_s = mass of vehicle structure including tankage, lbm
W_E = engine mass, lbm
W_r = residual and fixed mass, lbm
f = frequency, cps
g = gravitational conversion constant
h = height of liquid level, ft
k = constant of proportionality
n = acceleration factor
p = internal pressure, psi
q = dynamic pressure = $\frac{1}{2}\rho v^2$
r = radius of pressure sphere
t = skin thickness, in.
v_i = ideal velocity = $(I_s g)$ ln MR, fps
$f.s.$ = factor of safety
α = angle of attack
β = swivel engine control deflection
ρ_P = propellant density, slug/ft^3
ρ_s = density of structural material, lbm/in.^{3}
σ = fiber stress
τ = time, sec
δ = dead weight fraction, W_d/W_P
λ = payload ratio, W_L/W_i

References

1 Ezra, A. A. and Birnbaum, S., "Design Criteria for Space Vehicles to Resist Wind Induced Oscillations," ARS preprint no. 1081-60, April 1960.

2 Sandorff, P. E. and Petersen, L. K., "Propellant Tank Dynamics," Aerojet-General Corp., Rep. no. 1376, Contract AF33(616)-3767, Dec. 20 1957. (*Confidential*)

3 Bossart, K. J., "Design Problems of Large Rockets," High Altitude and Sounding Rockets Symposium, Cranfield, England, July 20, 1957. Published jointly by Royal Aeronautical Society and British Interplanetary Society, London, 1958.

4 Geissler, E. D., "Problems in Attitude Stabilization of Large Guided Missiles," IAS paper no. 60-63, June 1960.

5 Nelson, R. H., Jr., "The Sloshing of a Fluid Draining from a Flexible Tank," Ph.D. Thesis, MIT, Sept. 1960.

6 Sandorff, P. E., "Principles of Design of Dynamically Similar Models for Large Propellant Tanks," NASA Technical Note D-99, Jan. 1960.

7 Klawans, B., "The Vanguard Satellite Launching Vehicle," The Martin Co., Engineering Rep. no. 11022, April 1960. (*Confidential*)

8 Hebeler, H. K., Boeing Airplane Co., private communication, Feb. 25, 1960.

9 Kelley, O. A., "Parametric Weight Study of a Manned Space Entry Vehicle," IAS paper no. 60-56, Institute of Aero Sciences Summer Meeting, Los Angeles, June 1960.

10 NASA TN D-518, "Important Research Problems in Advanced Flight Structures Design—1960," Norris Dow, Ed., NASA Research Advisory Committee on Structural Design, June 1960.

11 Steinberg, M., Fox, J. and Augenstein, B., "A Proposed Ground and Flight Program to Develop Space Age Materials," ARS preprint 1103-60, April 1960.

12 Whipple, F. L., "The Meteoritic Risk to Space Vehicles," in "Vistas in Astronautics," Pergamon Press, N. Y., 1958, p. 115.

13 Gazley, C., Jr., Kellogg, W. W. and Vestine, E. H., "Space Vehicle Environment," *J. Aero/Space Sci.*, Dec. 1959, vol. 26, no. 12, pp. 770–782.

14 Bjork, R. L., "Effects of a Meteoroid Impact on Steel and Aluminum in Space," Tenth International Astronautical Congress, London, Sept. 1959.

15 Olshaker, A. E., "An Experimental Investigation in Lead of the Whipple Meteor Bumper," S. M. Thesis, MIT, June 1960.

16 Bjork, R. L. and Gazley, C., Jr., "Estimated Damage to Space Vehicles by Meteoroids," The Rand Corp., Research Memorandum RM-2332, Feb. 20, 1959.

17 Upson, R. H., "The General Problem of the Stressed-Skin Airship Hull," Daniel Guggenheim Airship Institute, Akron, Ohio, Publication no. 3, 1935.

18 Shanley, F. R., "Weight-Strength Analysis of Aircraft Structures," McGraw-Hill Book Co., Inc., N. Y., 1952.

19 Gerard, G., "Some Structural Aspects of Orbital Flight," ARS preprint no. 729-58, Nov. 1958.

20 Peterson, J. P., "Weight-Strength Studies of Structures Representative of Fuselage Construction," NACA Technical Note 4114, Oct. 1957.

21 Fung, Y. C. and Sechler, E. E., "Buckling of Thin-Walled Circular Cylinders Under Axial Compression and Internal Pressure," *J. Aeron. Sci.*, vol. 24, no. 5, May 1957, p. 351.

22 Harris, L. A., Suer, H. S., Skene, W. T. and Benjamin, R. J., "The Stability of Thin Walled Unstiffened Circular Cylinders Under Axial Compression Including the Effects of Internal Pressure," *J. Aeron. Sci.*, vol. 24, no. 8, Aug. 1957, p. 587.

23 Sandorff, P. E., "Space Flight—Structures and Materials," *Aviation Age*, March 1958.

24 Sutton, G. P., "Liquid Propellant Rocket Engines," in "Space Technology," H. Seifert, Ed., John Wiley and Sons, Inc., N. Y., 1959, chap. 15.

25 Newell, H. E., Jr., "Sounding Rockets," McGraw-Hill Book Co., Inc., N. Y., 1959, chap. 5.

26 The Martin Co., "The Viking RTV-N-12a Design Summary," ER 6534, Contract N6-onr-171, Aug. 1955.

27 Rosen, M. W. and Schwenk, F. C., "Nova—A Manned Lunar Rocket," Astronautics, Sept. 1959, vol. 4, no. 9, p. 20.

Fundamental Satellite Perturbations

F. T. GEYLING[1]

Bell Telephone Laboratories, Inc.
Murray Hill, N. J.

A brief exposition, from an elementary point of view, is given for some basic satellite perturbations. The treatment serves to generate independent checks of formal results from more elaborate analyses and to establish a direct relation of these results to physical principles. Attention is given to in-plane and precessional perturbations of circular orbits resulting from oblateness, luni-solar gravitation and radiation pressure. The derivations have quantitative validity and may be extended to more general situations.

IN THE following, some of the basic phenomena of satellite motion are discussed in the most direct and unsophisticated way that seems possible. The derivations are really the outcome of a quest for independent checks of the results obtainable from the well-established and refined methods of astronomical perturbation analysis.[2] Naturally, an approach from first principles, i.e., energy and momentum conditions, seemed desirable. It is felt that these developments may be of tutorial value to the non-expert who desires a basic understanding of satellite orbit perturbations (on the other hand this "return to nature" may have some amusement value for the specialist in dynamical astronomy). The physical phenomena treated here are: The distortion of an orbit within its own plane resulting from extraterrestrial gravitation, apsidal precession and buildup of eccentricity resulting from radiation pressure, apsidal precession and changes in epoch resulting from the equatorial bulge, and nodal precessions resulting from oblateness, extraterrestrial gravitation and radiation pressure. The geometric relations between the orbit and the source of perturbation have been specialized for maximum simplicity in each case. The quantitative results are precisely correct in all but one example, where a very good approximation of the true rate of precession is obtained.

In-the-Plane Perturbations of the Orbit

For the demonstrations of in-the-plane perturbations of the satellite orbit, we start with the simplest shape—a circular orbit. A convenient coordinate system by which the satellite's departure from the unperturbed orbit may be described are the ξ,η axes of Fig. 1. Their origin lies at a point such as $0'$ which would be the vehicle's instantaneous position in the absence of perturbations. The ξ,η system then is moving with $0'$ while the x,y system, with origin at E, may be taken as an inertial one. The instantaneous radial and tangential velocity components of the satellite shall be denoted by U_r and U_t; the perturbative forces in the ξ,η and x,y system shall be the symbol F with suitable subscripts. (See Fig. 1.) We may then derive the equations of motion of the vehicle in the ξ,η system from the fact that the time derivative of its energy K equals the rate at which work is done on it by the perturbative forces, and the time derivative of its angular momentum A about E equals the moment of the perturbative forces about E. Thus

$$dK/dt = F_tU_t + F_rU_r \qquad [1]$$

$$dA/dt = F_t(r_c + \xi) - F_r\eta \qquad [2]$$

where r_c is the radius of the circular orbit. Clearly

$$K = \frac{m}{2}\dot{\theta}^2[(r_c + \xi + \eta')^2 + (\xi' - \eta)^2] - \frac{GEm}{[(r_c + \xi)^2 + \eta^2]^{1/2}} \qquad [3]$$

$$A = m\dot{\theta}[(r_c + \xi + \eta')(r_c + \xi) - (\xi' - \eta)\eta] \qquad [4]$$

where the primes indicate differentiation with respect to θ, dots denote time derivatives, and GE is the universal gravitational constant times Earth's mass. Substituting Equations [3 and 4] into Equations [1 and 2], we find after some simplification

$$\frac{GEm}{r_c^3}[r_c(2\xi' + \eta'') + (\xi'' - \xi)\xi' + \eta'(2\eta + \eta'') - \eta\xi'' + \xi\eta''] = F_t(r_c + \xi + \eta') + F_r(\xi' - \eta) \qquad [5]$$

and

$$\frac{GEm}{r_c^3}[(r_c + \xi)(2\xi' + \eta'') + (2\eta' - \xi'')\eta] = F_t(r_c + \xi) - F_r\eta \qquad [6]$$

If we retain terms of $0(r_c\xi)$ in the brackets of the left-hand sides and $0(r_c)$ in the parentheses of the right-hand sides, both equations yield

$$2\xi' + \eta'' = (r_c^3/GEm)F_t \qquad [7]$$

Going to $0(\xi^2)$ on the left and $0(\xi)$ on the right, we may eliminate between Equations [5 and 6] to obtain

$$\xi'' - 2\eta' - 3\xi = (r_c^3/GEm)F_r \qquad [8]$$

The solution for the homogeneous form of Equations [7 and 8] may be easily found as

$$\xi = \frac{2}{\dot{\theta}}\dot{\eta}_0 + 4\xi_0 - \left[\frac{2}{\dot{\theta}}\dot{\eta}_0 + 3\xi_0\right]\cos\theta + \frac{1}{\dot{\theta}}\dot{\xi}_0\sin\theta \qquad [9]$$

$$\eta = \eta_0 - \frac{2}{\dot{\theta}}\dot{\xi}_0 - 3\left[\frac{1}{\dot{\theta}}\dot{\eta}_0 + 2\xi_0\right]\theta + 2\left[\frac{2}{\dot{\theta}}\dot{\eta}_0 + 3\xi_0\right]\sin\theta + \frac{2}{\dot{\theta}}\dot{\xi}_0\cos\theta \qquad [10]$$

Received Aug. 20, 1959.

[1] Member of the Technical Staff. Member ARS.

[2] For treatments of this kind, the reader is referred to such well-known texts as references (1 and 2). Since the present discussion is not an attempt to emulate the classical analyses, our somewhat unconventional notation will have to be excused by some astronomers.

This may be used in a straightforward manner to generate particular solutions for nonvanishing right-hand sides, which are really the cases that interest us here.

As mentioned before, our first example will be the perturbation resulting from extraterrestrial gravitation. We locate a disturbing body with mass P on the positive y axis (Fig. 1) so that

$$F_x = -\frac{r_c GPm}{r_{EP}^3}\cos\theta \qquad F_y = \frac{2r_c GPm}{r_{EP}^3}\sin\theta$$

where r_{EP} is the distance from E to P. The forces F_x and F_y are the components of the vector difference of perturbative attraction by P on the satellite and on Earth. Transforming this to F_t and F_r, and substituting these expressions into Equations [7 and 8], we find the solutions

$$\xi = g[1 + 2\cos 2\theta] \qquad [11]$$

$$\eta = -(1/4)g[8\theta + 11\sin 2\theta] \qquad [12]$$

where $g = Pr_c^4/2Er_{EP}^2$. The first term in each of these expressions is secular, whereas the second one is periodic in nature. The periodic term in ξ shows that the orbit develops a major axis in the x direction and a minor axis in the y direction. The periodic term in η expresses the angular anomalies which are caused by the varying distance from E to the satellite, $r_c + \xi$, in order to fulfill the conditions on A and K. This treatment may be easily extended to allow for a moving body P, which, however, adds little to the demonstration of fundamental principles. If we apply these results to lunar perturbations on a 24-hr satellite, we find that the maximum amplitudes of this effect are approximately 3000 ft in η and 2200 ft in ξ. Both displacements are negligible from a practical point of view, whereas the effects of inaccurate launch conditions may be much more significant, as calculated from Equations [9 and 10].

In order to study the effects of radiation pressure, we consider the same configuration as in Fig. 1. The perturbative forces are then

$$F_y = -\beta m/r_{EP}^2 \qquad F_x = 0$$

where β is a coefficient which accounts for radiation intensity and shape, size, surface to mass ratio, and reflectivity of the satellite.[3] From this we note that

$$F_r = -\frac{\beta m}{r_{EP}^2}\sin\theta \qquad F_t = -\frac{\beta m}{r_{EP}^2}\cos\theta$$

which when substituted into Equations [7 and 8] yield

$$\xi = \tilde{g}\,[\theta\, 3\cos\theta - (7/2)\sin\theta] \qquad [13]$$

$$\eta = -\tilde{g}[\theta\, 6\sin\theta + 11\cos\theta] \qquad [14]$$

where $\tilde{g} = \beta r_c^3/2GEr_{EP}^2$.

The most significant features about this result are the periodic terms with increasing amplitudes in both displacements. They are not a surprise if one notes that the excitation given by F_r and F_t is in resonance with the free oscillations of the satellite about the point 0′ as shown by Equations [9 and 10]. Of course one then expects a response whose amplitude grows without limit. It may be shown that this feature is indeed not far from physical reality if the effects of other perturbations are not considered simultaneously with radiation pressure. For the time being, one can deduce the following useful results from this analysis.

The condition $d\xi/d\theta = 0$ reads

$$\theta = -(1/6)\cot\theta \qquad [15]$$

where the pair of roots for θ in each interval of 2π gives the locations of perigee and apogee in that particular pass around the orbit. Inspection of Equation [15] shows that the two apsides approach an angular separation of π only as a limit for large numbers of revolutions. In particular the sequence of roots for ω_q reads

$$\omega_q = 3.08 + \frac{\eta(3.08)}{r_c} \qquad 2\pi + 3.13 + \frac{\eta(2\pi + 3.13)}{r_c}, \ldots$$

where the terms $\eta(\ )/r_c$ are small corrections and

$$\lim_{n \to \infty} \omega_q = (2n - 1)\pi$$

n is the number of the current revolution. A corresponding sequence of roots may be written for ω_Q, the apogee location, with

$$\lim_{n \to \infty} \omega_Q = 2n\pi$$

A physical interpretation of the way in which the apsides are formed by radiation pressure may be given in the following manner. The satellite is being accelerated tangentially by F_t during the approximate interval $\pi/2 < \theta < \pi$. In order to balance the additional centrifugal force resulting from the increased circumferential speed, a decrease in r is required to enhance the gravitational attraction. Thus perigee is formed in the neighborhood of $\theta = \pi$. The opposite mechanism acts to generate apogee near $\theta = 2\pi$.

Now let us define the average value of the semimajor axis for one revolution as

$$\bar{a} = r_c + (1/2)(\xi_{\max} + \xi_{\min})$$

and let us assume for convenience that $\omega_Q = \omega_q + \pi$ in each revolution, then

$$\bar{a} \simeq r_c - \tilde{g}\pi(3/2)\cos\omega_q \qquad [16]$$

which proves that the orbit size is practically unaffected by radiation pressure. For the eccentricity, averaged over 2π, we get however

$$\bar{e} = \frac{1}{2r_c}(\xi_{\max} - \xi_{\min}) \simeq \frac{\tilde{g}}{2r_c}\left[-6\left(\omega_q + \frac{\pi}{2}\right)\cos\omega_q + 7\sin\omega_q\right] \qquad [17]$$

This indicates a secular buildup of eccentricity at the rate

$$\bar{e}' \simeq (-3\tilde{g}/r_c)\cos\omega_q$$

Again we should emphasize that the validity of this result needs to be examined in the light of the various factors that enter a complete solution of the problem. They are the variation of the gravitational potential gradient for large departures from the circular orbit, variable radiation intensity as a function of θ resulting from Earth's shadow and albedo,[4] and the interaction of perturbations from physical sources other than radiation with the effects of the latter. Clearly such a complete treatment is beyond the scope of the basic demonstrations intended here and is given elsewhere. [See reference (3).]

Our last example of in-the-plane perturbations of near-circular orbits concerns the precession of apsides for a slightly elliptic orbit owing to Earth's oblateness. If the oblateness term were absent from Earth's potential, then a slightly elliptic orbit may be described by Equation [10] as resulting from slightly noncircular launch conditions. Here the circular frequency of the periodic terms for ξ and η is that of the orbital motion, and the axes of the eccentric orbit would consequently remain stationary in the x,y plane. If, however, the restoring forces in the satellite's oscillations about the circular orbit are slightly altered by the oblateness term, then a corresponding frequency change occurs in ξ and η, and the latter are no longer in tune with the orbital motion of 0′. Consequently, a precession of the apsides results. Our first

[3] The satellite is assumed to be an isotropic reflector.

[4] This feature turns out to have only a minor effect on the results [15 to 17].

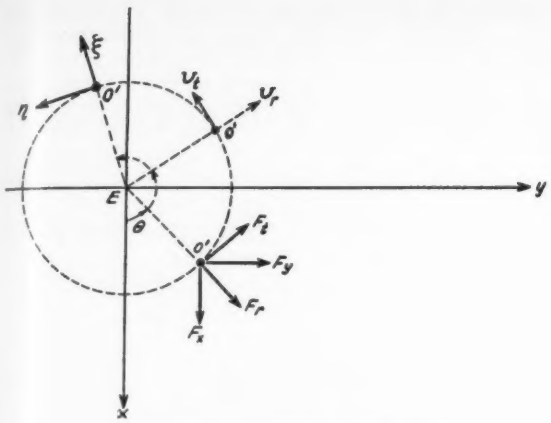

Fig. 1 In-plane perturbation of orbit

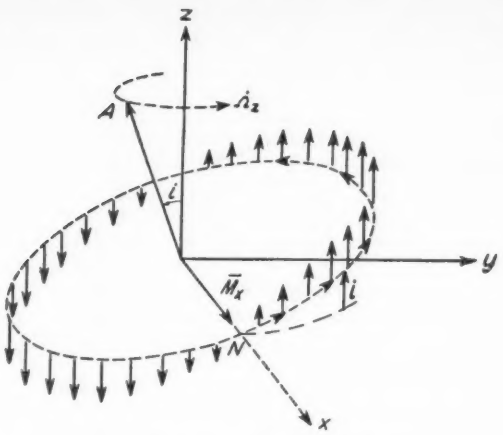

Fig. 2 Perturbation of the orbit plane

task then consists of modifying Equations [7 and 8] to account for a nonspherical Earth. This we may do by using the approach which led to Equations [5 and 6] but replacing the last term in Equation [3] by a more accurate representation of the geopotential. This potential function is usually assumed to be rotationally symmetric about Earth's polar axis, here the z-axis, and thus lends itself to expansion in terms of Legendre polynomials in sin φ where φ is the geocentric latitude. One then finds

$$V = -\frac{GEm}{r} - \frac{Jr_E^2GEm}{r^3}\left[\frac{1}{3} - \frac{z^2}{r^2}\right] - \frac{Dr_E^4GEm}{r^5}\left[\frac{z^4}{r^4} - \frac{6}{7}\frac{z^2}{r^2} + \frac{3}{35}\right] + \ldots \quad [18]$$

where

z/r = sin φ
r_E = 3963.247 miles, Earth's equatorial radius
J = 1.638 10^{-3}, the coefficient for P_2
D = 1.070 10^{-5}, the coefficient for P_4

For the present discussion we may safely drop D from Equation [18], so that for $z = 0$ the radial equilibrium condition of the nominal orbit can be written as

$$V_\xi = \frac{GEm}{r_c^2}\left(1 + J\frac{r_E^2}{r_c^2}\right) = m\dot{\theta}^2 r_c$$

Hence

$$\dot{\theta}^2 = \frac{GE}{r_c^3}\left(1 + \frac{Jr_E^2}{r_c^2}\right) \quad [19]$$

which indicates the slight correction to be made in $\dot{\theta}$, the angular rate of $0'$, as compared to motion around a spherical Earth. Writing the time derivative of Equation [18] and using $r^2 = (r_c + \xi)^2 + \eta^2$ to write binomial expansions for $1/r^3$ and $1/r^5$, one obtains

$$\frac{dV}{dt} = GEm\dot{\theta}\frac{1}{r_c^2}\left[\left(1 + J\frac{r_E^2}{r_c^2}\right)\xi' - \frac{2}{r_c}\left(1 + 2J\frac{r_E^2}{r_c^2}\right)\xi\xi' + \frac{1}{r_c}\left(1 + J\frac{r_E^2}{r_c^2}\right)\eta\eta'\right]$$

to $0(\xi^2)$ in the brackets. Using Equation [19] this becomes

$$\frac{dV}{dt} = m\dot{\theta}^3\left[r_c\xi' - 2(1+\lambda)\xi\xi' + \eta\eta'\right] \quad [20]$$

where $\lambda = Jr_E^2/(r_c^2 + Jr_E^2)$. Substituting Equation [20] as the potential term in the time derivative of Equation [3], we arrive at the following modified version of Equation [8] for the homogeneous case

$$\xi'' - 2\eta' - (3 + 2\lambda)\,\xi = 0$$

which of course reduces to [8] if $J = 0$. The homogeneous form of Equation [7] is unaffected by the change in potential. The solution of this pair of equations is

$$\xi = b_1 \sin \kappa\theta + b_2 \cos \kappa\theta + b_3$$

$$\eta = b_4 - \frac{1}{2}(3 + 2\lambda)b_3\vartheta - \frac{2b_2}{\kappa}\sin \kappa\theta + \frac{2b_1}{\kappa}\cos \kappa\theta \quad [21]$$

where $\kappa = 1 - \lambda$ to $0(\lambda)$, and $b_{1,2,3,4}$ are integration constants.

Since the circular frequency of ξ and η is less than the orbital frequency, a forward motion of the apsides occurs which corresponds to the average rate

$$\dot{\omega} = \dot{\theta}\lambda = \dot{\theta}Jr_E^2/(r_c^2 + Jr_E^2) \quad [22]$$

This result differs from the first-order approximation by more elaborate techniques only by the presence of Jr_E^2 in the denominator.

For a 6000-mile orbit and the constants that were given with Equation [18], we obtain $\omega = 0.479\ 10^{-6}$ rad per sec, and thus an apsidal period of 152 days. Finally, the decrement of epoch during a specified revolution amounts to

$$\Delta_n\tau = -\frac{1}{r_c\dot{\theta}}\left[\eta_n(\theta_\tau) - \eta_{n-1}(\theta_\tau)\right] \quad [23]$$

where θ_τ marks the point whose time of passage is used as the epoch, and n identifies the orbital pass that is being completed.

Perturbations of the Orbit Plane

We will now discuss the physical effects which force a satellite to depart from its original orbital plane, or in other words, which change the orientation of this plane. We now tilt the circular orbit about the x-axis and denote the angle of inclination to the x,y plane by i (see Fig. 2). The ascending node is N. Applying the right-hand rule to the rotation of the satellite in its orbit, the angular momentum vector $\vec{A}$ of this motion forms the angle i with the positive z-axis. We now return to Equation [2] in its vectorial form

$$d\vec{A}/dt = \vec{M}$$

where $\vec{M}$ is a moment that may be exerted on the orbit by perturbative forces. If these perturbations result from the equatorial bulge, we observe from symmetry that the average moment over one revolution lies along the x-axis. It shall be denoted by $\bar{M}_x$. If a positive $\bar{M}_x$ is taken to point in the positive x direction, we note by the preceding equation that it produces a rotation of the momentum vector about the z-axis at a rate $\dot{\Omega}_z = \bar{M}_x/A \sin i$ while the magnitudes of the momentum vector and the inclination remain unchanged. The positive sense of $\dot{\Omega}_z$ is defined again by the right-hand rule about z. The nodal points of the orbit will then precess in the x,y plane at the rate $\dot{\Omega} = \dot{\Omega}_z$.

Since θ is constant around the orbit, a time average of $|\vec{M}|$ is equivalent to an average against θ. As a result of Earth's oblateness we have

$$F_z = -V_z = -(2GEmJr_E^2/r_c^4) \sin\theta \sin i$$

$$\bar{M}_x = \frac{GEmJr_E^2}{2\pi r_c^3} \sin 2i \int_0^{2\pi} \sin^2\theta \, d\theta = -\frac{GEmJr_E^2}{2r_c^3} \sin 2i$$

(The contribution of F_x to this moment can be shown to vanish.) Recalling that

$$A = \dot{\theta} r_c^2 m = (GEr_c)^{1/2} m$$

we find

$$\dot{\Omega} = -J\left(\frac{r_E}{r_c}\right)^2 \left(\frac{GE}{r_c^3}\right)^{1/2} \cos i \qquad [24]$$

Since $\dot{\Omega}$ is negative, we speak of a regression of the nodes. This result agrees exactly with the expression which can be obtained by more advanced methods. If $r_c = 5000$ miles and $i = 51$ deg, we find $\dot{\Omega}$ to be equal to $-5.80\ 10^{-7}$ rad per sec or 0.24 deg per revolution (where the anomalistic period is 7180 sec). The nodal period amounts to 125 days.

Finally, we examine the nodal precessions resulting from gravitation and radiation from a distant body P which we locate again on the positive y-axis. A perturbative moment $\bar{M}_x$ will be exerted on the orbit, resulting in a precession

$$\dot{\Omega}_y = \bar{M}_x/A \cos i \qquad [25]$$

which in this case takes place about the y-axis because the moment vector, initially $\bar{M}_x$, remains always in the x,z plane as the orbit is perturbed. Inspection of the geometry at the node N shows that for small precessional angles we have

$$\dot{\Omega} = \dot{\Omega}_y \cot i = \bar{M}_x/A \sin i \qquad [26]$$

and

$$di/dt = 0$$

For the case of gravitational interference, we note that

$$F_y = (2r_c GPm/r_{EP}^3) \sin\theta \cos i$$

$$F_z = -(r_c GPm/r_{EP}^3) \sin\theta \sin i$$

F_x makes no contribution to $\bar{M}_x$. Then

$$\bar{M}_x = -\frac{1}{2\pi}\int_0^{2\pi} (F_y r_c \sin\theta \sin i - F_z r_c \sin\theta \cos i) d\theta$$

$$= -\frac{3 \sin 2i r_c^2 GPm}{4r_{EP}^3}. \qquad [27]$$

With Equation [26] this results in

$$\dot{\Omega} = -(3P/2Er_{EP}^3)(GEr_c^3)^{1/2} \cos i \qquad [28]$$

For a 24-hr satellite with $i = 20$ deg we thus find $\dot{\Omega} = -1.64\ 10^{-9}$ rad per sec owing to lunar gravitation.

Turning finally to the precessional effects of radiation pressure, we note that $\bar{M}_x = 0$ for a uniformly illuminated orbit. Since this case is not at all realistic, we add the factor $(1 + \sin\theta)$ to the radiation pressure, indiating that the peak intensity occurs on the side of the orbit toward the illuminating body. Thus

$$F_y = -\frac{\beta m}{r_{EP}^2}(1 + \sin\theta) \qquad F_x = F_z = 0 \qquad [29]$$

The sine term in F_y will now generate a perturbing moment on the orbit which is

$$\bar{M}_x = (\beta m r_c/2r_{EP}^2) \sin i$$

Using Equation [26]

$$\dot{\Omega} = \frac{\beta}{2r_{EP}^2}\left(\frac{r_c}{GE}\right)^{1/2} \qquad [30]$$

It is interesting to note that this precession is independent of i. For a 100-ft mylar balloon with a metallized skin of 0.0005-in. thickness, the nodal precession of a 24-hr orbit would amount to $0.6325\ 10^{-7}$ rad per sec. A more complete discussion of the cumulative precession due to radiation pressure is given in reference 3.

Conclusion

The elementary techniques discussed may be readily applied to other physical effects, such as atmospheric drag and the magnus force on spinning satellites. It is hardly necessary to point out that the simple approaches which were given here could, with due perseverance, be extended to the more complicated geometry of more general situations, although they do not compete in elegance and power with the established methods of dynamical astronomy. They have, however, served us well in providing spot checks by which most perturbation phenomena may be traced back to elementary principles.

Nomenclature

m	= satellite mass
GE	= mass of Earth times universal gravitational constant
GP	= mass of planet times universal gravitational constant
x,y,z	= geocentric Cartesian coordinates
ϵ,η	= moving coordinates relative to nominal satellite position
r	= distance Earth to satellite
r_{EP}	= distance Earth to planet
r_c	= radius of nominal circular orbit
θ	= nominal angular position of satellite
K	= total energy of satellite
A	= angular momentum of satellite
$F_{x,y,t,r}$	= perturbing forces acting on satellite
$U_{r,t}$	= radial and circumferential velocity components of satellite
r_E	= Earth's equatorial radius
V	= Earth's gravitational potential
J,D	= Earth's oblateness parameters
$\omega_{q,Q}$	= locations of perigee and apogee
$\dot{\omega}$	= apsidal rate of precession
$\dot{\Omega}$	= nodal rate of precession

References

1 Moulton, F. R., "Introduction to Celestial Mechanics," MacMillan Co., N. Y., 1958.

2 Smart, W. M., "Celestial Mechanics," Longmans, Green and Co., N. Y., 1953.

3 Geyling, F. T., "Satellite Perturbations from Extra-Terrestrial Gravitation and Radiation Pressure," *J. Franklin Inst.*, vol. 269, May 1960, p. 375.

Optimum Orbital Transfer by Impulses

LU TING[1]

Polytechnic Institute of Brooklyn
Brooklyn, N. Y.

The minimum impulse transfer from a given initial orbit to the final orbit of given geometry accomplished by multiple or single impulse is considered. It is shown that the total impulse will be minimum if the two orbits and the transfer trajectory are co-planar. If there is only a single impulse available, the orbital transfer can be accomplished provided that the final orbit can intersect the initial orbit at some orientations. The procedure of finding the optimum orientation is presented. With two impulses available, the orbital transfer can be accomplished without any limitation on the geometries of the initial and the final orbit. It is shown that the sum of the two impulses will be a minimum if the major axes of the two orbits and the transfer ellipse coincide with each other and are oriented in the same sense, and the apogee of the transfer ellipse coincides with that of the orbit with longer apogee distance while the perigee of the transfer orbit coincides with that of the other orbit.

THE PROBLEM of transferring a vehicle from one orbit into another about the same attracting body under the optimum condition has been investigated by Hohmann (1),[2] Lawden (2,3), Munick (4) and others [see references in (5)]. In their investigations, the orbits are co-planar and explicit, or numerical results have been obtained only for the special case of two circular orbits (1) and the case of two elliptical orbits with special geometry and/or orientation (2–4).

In the problem of re-entry of a vehicle from an initial orbit to Earth, it is desirable to transfer the vehicle into a final orbit which will enter the "limit of atmosphere" near its perigee, so that atmospheric drag can be employed to reduce the velocity of the vehicle. The geometries of an orbit are defined by its eccentricity e and its semilatus rectum p. For the initial orbit, they are specified. For the final orbit, they are determined by the entry velocity and angle at the limit of atmosphere. The orientation of the final orbit with respect to the initial orbit is not specified. It should be such that the orbital transfer takes place with minimum fuel consumption.

In the present paper, it is assumed that the initial orbit and the transfer trajectory lie outside the limit of atmosphere and that the orbital transfer is accomplished by several impulses. The transfer trajectory will be composed of several elliptical arcs which together with the initial and the final orbit possess a common focus. The change in velocity at the intersection of two elliptical arcs is proportional to the impulse which represents an integral of the thrust of a rocket engine during a very short firing period. If the rocket engines are similar, the requirement of minimum fuel consumption is equivalent to that of minimum impulses required for the transfer, which in turn is equivalent to that minimum change in velocity.

The investigation begins with the proof that the optimum orbital transfer can be reduced to a planar problem.

Justification of Reduction to Planar Problem

To prove that for the optimum transfer the two orbits and the transfer trajectory should be co-planar, it is shown first that for any orbital transfer at the intersection of two non co-planar orbits there exists a corresponding co-planar transfer with less impulse required.

Received Jan. 20, 1960.

[1] Research Associate Professor.

[2] Numbers in parentheses indicate References at end of paper.

Proof: For a given system, or a given value of the stationary mass M at the focus, the areal velocity h is constant for each orbit. The equation of the orbit and the radial and circumferential components, v and u, of the orbiting velocity are (6)

$$\frac{1}{r} = \frac{1}{p}(1 + e\cos\vartheta) \qquad [1]$$

$$u = \frac{h}{r} = \frac{h}{p}(1 + e\cos\vartheta) \qquad [2a]$$

$$v = \dot{r} = -h\frac{d}{d\vartheta}\left(\frac{1}{r}\right) = \frac{he}{p}\sin\vartheta \qquad [2b]$$

$$p = \frac{h^2}{\mu} = \frac{h^2}{MG} \qquad [3]$$

where

r = distance from the common focus
ϑ = true anomaly
G = universal gravitational constant

u and v depend only on the angular distance from the perihelion.

As shown in Fig. 1, orbits 1 and 2 intersect each other at point K. Therefore SK is the line of intersection of the plane of orbit 1 and that of orbit 2. The angle between these two planes is denoted by ψ. The radial distance of K from the focus S is r^* with

$$\frac{1}{r^*} = \frac{1}{p_1}(1 + e_1\cos\vartheta_1^*) = \frac{1}{p_2}(1 + e_2\cos\vartheta_2^*) \qquad [4]$$

where the starred quantities refer to those at the point K, and subscripts 1 and 2 indicate quantities associated with orbits 1 and 2, respectively. For both orbits, the directions of their radial velocity components at the point K are the same, whereas the directions of their circumferential velocity components lie in the plane normal to the radial direction SK.

Since the direction of the circumferential velocity lies in the plane of the corresponding orbit and normal to the line of intersection of SK, the angle between the velocities u_2 and u_1 is ψ. The change in velocity for the orbital transfer at that orientation is

$$\Delta V = \sqrt{(v_1^* - v_2^*)^2 + u_1^{*2} - 2u_1^*u_2^*\cos\psi + u_2^{*2}} \qquad [5]$$

If the plane of orbit 2 is rotated about the line SK while the plane of orbit 1 is stationary, point K remains at the point of intersection of the two orbits. The focus of both orbits remains at S; and the value of ϑ_1^* and ϑ_2^*, and hence those of u_1^*, v_1^*, u_2^* and v_2^*, are unchanged. In the process of rotation, only ψ is changed. If u_1^*, u_2^* have the same sign, i.e., if the two orbits are in the same sense, ΔV attains its minimum value at $\psi = 0$; i.e., the two orbits are co-planar.

If u_1^*, u_2^* have opposite sign, ΔV attains its minimum value at $\psi = \pi$. Again the two orbits are co-planar. This concludes the proof.

If the transfer from the initial to the final orbit is accomplished by several impulses and the transfer trajectory is composed of several elliptical arcs, then, according to the preceding proof, the two elliptical arcs associated with the same impulse should be co-planar. Therefore, the following conclusion can be drawn: *For the optimum orbital transfer, the initial orbit, the final orbit and the transfer trajectory should be co-planar.*

The next step is to find the optimum transfer trajectory and the relative orientation of two co-planar orbits.

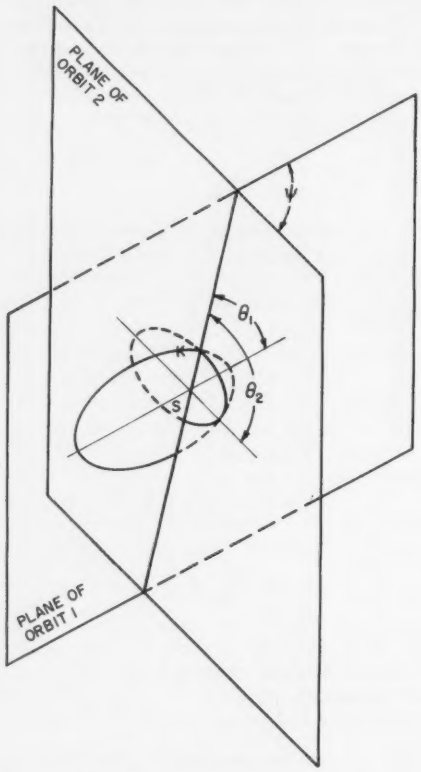

Fig. 1 Nonplanar transfer

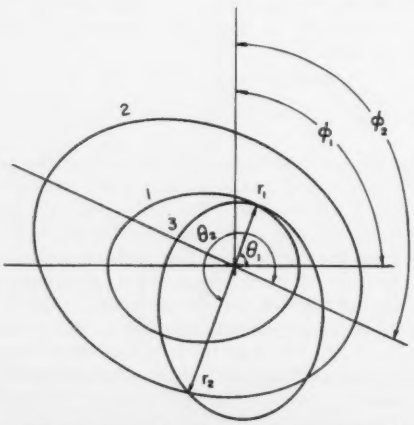

Fig. 2 Orbits 1 and 2 and the transfer orbit 3

Optimum Transfer by Single Impulse

With single impulse the transfer trajectory reduces to the point of intersection of the initial and the final orbit, orbits 1 and 2. This is feasible if the apogee distance (r_a) of one orbit is greater than the perigee distance (r_p) of the other.

For the planar problem, $\psi = 0$ and Equation [5] becomes

$$|\Delta V| = \sqrt{(v_1^* - v_2^*)^2 + (u_1^* - u_2^*)^2} \qquad [6]$$

The change of velocity $|\Delta V|$ is a function of two variables ϑ_1^* and ϑ_2^* which are related by Equation [4]. Therefore, $|\Delta V|$ is a function of one independent variable, say ϑ_1^*, and the optimum transfer takes place when $|\Delta V|$ or $(\Delta V)^2$ is a minimum, i.e.

$$\frac{d(\Delta V)^2}{d\vartheta_1^*} = 0 \qquad \frac{d^2(\Delta V)^2}{(d\vartheta_1^*)^2} > 0 \qquad [7]$$

In an argument similar to that given in the preceding section, Loh (7) concluded that the optimum transfer occurs at the point of tangency of the two co-planar orbits. The argument is not valid in the present case, because when the relative orientation changes the location of the point of intersection, ϑ_1^* changes, and so do the velocities u_1, v_1, u_2 and v_2. In the following paragraph it will be shown that at the point of tangency $|\Delta V|$ is not an extremum.

At the point of tangency of the two orbits, with $\vartheta_1 = \vartheta_t$ and $\vartheta_2 = \vartheta_t + \varphi_t$, the conditions on ϑ_t and φ_t are

$$p_2(1 + e_1 \cos \vartheta_t) = p_1[1 + e_2 \cos (\vartheta_t + \varphi_t)]$$

and

$$p_2 e_1 \sin \vartheta_t = p_1 e_2 \sin (\vartheta_t + \varphi_t)$$

With these two relationships, it can be shown that

$$\left[\frac{d(\Delta V)^2}{d\vartheta_1^*}\right]_{\vartheta_1^* = \vartheta_t} = 2\mu e_1 \sin \vartheta_t \frac{(\sqrt{p_1} - \sqrt{p_2})^2}{p_2}$$

For the upper half of orbit 1, $0 < \vartheta_t < \pi$; therefore the first derivative of ΔV is always positive, and the optimum transfer takes place at an angle ϑ_1^* less than ϑ_t. For the exceptional case of $\sin \vartheta_t = 0$, the radial distance of the perigee of one orbit is equal to that of the perigee of the other, and $\vartheta = \vartheta_t = 0$ or π is the only possible position for the transfer by one impulse.

The value of ϑ_1^* is obtained from Equations [7] by Newton's method with ϑ_t as the starting value. ϑ_t does not exist if the geometries of the two orbits are such that either they do not intersect or they do at all the orientations. For the former case transfer by one impulse is impossible, and for the latter case the true anomaly of one of the points of intersection when $\vartheta_1 = \vartheta_2$ is employed as the starting value of ϑ_1^*. Numerical data regarding the optimum change of velocity, the thrust angle, the location of the orbital transfer and the relative orientation of the two orbits are given in the tables and the charts of (8).

Optimum Transfer by Two Impulses

The two impulses are applied at the point of intersection of the transfer trajectory with the initial orbit 1 and the point of intersection of the transfer trajectory with the final orbit 2, respectively. If the specific impulse does not change, the requirement of minimum fuel consumption is equivalent to

the requirement that the sum of the absolute value of the changes of velocity owing to impulse is a minimum, i.e.

$$S = |\Delta V_1| + |\Delta V_2| = \min \qquad [8]$$

where

ΔV_1 = change of velocity from orbit 1 to transfer trajectory
ΔV_2 = change of velocity from transfer trajectory to orbit 2

S is a function of four independent variables, namely, the geometry of orbit 3, e_3 and p_3 and the orientation of orbits 2 and 3 with respect to orbit 1. The conditions for an extremum of S are in general four nonlinear simultaneous algebraic equations. In (9), it has been shown that the extremal conditions are fulfilled by the solutions of the following equations (Fig. 2)

$$\sin \vartheta_1 = \sin \vartheta_2 = \sin \vartheta_3 = \sin \vartheta_4 = 0 \qquad [9]$$

where ϑ_1 and ϑ_3 represent the true anomalies of the point of intersection of orbits 1 and 3, and ϑ_2 and ϑ_4 represent the true anomalies of the point of intersection of orbits 2 and 3, respectively. This statement will be verified in a different manner in this paper. It will be shown that the first variation of transfer solution subjected to Equation [9] vanishes; the second variation is examined to find out whether the extremal solution is a local minimum solution. The examination of the second variation is simplified when two of the four independent variables therein are uncoupled from the other two. This is accomplished by selecting ϑ_1, ϑ_2, ϑ_3 and ϑ_4 as the four independent variables of S.

Before the study of the extremal solutions, all the possible combinations of the geometries of the initial and the final orbit will be classified as follows:

I Orbits 1 and 2 never intersect each other

$$(r_a)_2 > (r_p)_2 > (r_a)_1 > (r_p)_1 \qquad [10a]$$

II Orbits 1 and 2 always intersect each other

$$(r_a)_1 > (r_a)_2 > (r_p)_2 > (r_p)_1 \qquad [10b]$$

III Orbits 1 and 2 intersect each other at certain orientations

$$(r_a)_2 > (r_a)_1 > (r_p)_2 > (r_p)_1 \qquad [10c]$$

where

r_a = radial distance of apogee $= p/(1 - e)$
r_p = radial distance of perigee $= p/(1 + e)$

It will be understood that these three combinations also include the corresponding ones where the subscripts 1 and 2 are interchanged. For an optimum transfer trajectory from orbit 1 to 2 is also an optimum one for the reverse transfer.

The combinations of the geometries of the initial and final orbits depend on three parameters, p_1/p_2, e_1 and e_2. For a given value of e_2, the combinations I, II and III lie in the corresponding regions in the p_1/p_2, e_1 plane as shown in Fig. 3.

For region I, the condition $(r_p)_2 > (r_a)_1$ yields the upper bound for p_1

$$\frac{p_1}{p_2} < \frac{1 - e_1}{1 + e_2} \qquad [11a]$$

For region II, the lower and upper bounds of p_1 are

$$\frac{1 - e_1}{1 - e_2} < \frac{p_1}{p_2} < \frac{1 + e_1}{1 + e_2} \qquad [11b]$$

It is clear that

$$e_2 < e_1 < 1$$

For region III, the lower and upper bounds of p_1 are

$$\frac{1 - e_1}{1 + e_2} < \frac{p_1}{p_2} < \begin{cases} (1 + e_1)/(1 + e_2) & \text{for } e_2 > e_1 \\ (1 - e_1)/(1 - e_2) & \text{for } e_2 < e_1 \end{cases} \qquad [11c]$$

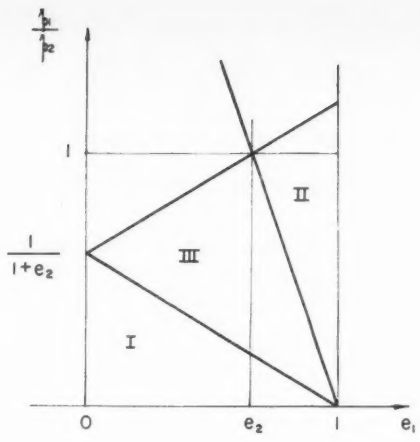

REGION I, $(r_a)_2 > (r_p)_2 > (r_a)_1 > (r_p)_1$

REGION II, $(r_a)_1 > (r_a)_2 > (r_p)_2 > (r_p)_1$

REGION III, $(r_a)_2 > (r_a)_1 > (r_p)_2 > (r_p)_1$

Fig. 3 Classification of combinations of initial and final orbits

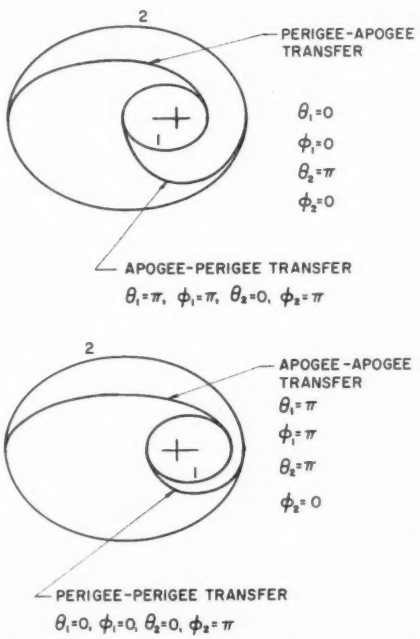

Fig. 4 Combination I—initial and final orbits cannot intersect each other

The solutions of Equation [9] for each of these three combinations are examined separately in the following.

Combination I—Initial and Final Orbit Never Intersect Each Other

Owing to the restriction of Equations [10a] or [11a], the apogee of the transfer orbit 3, corresponding to the solution of Equation [9], has to coincide with the apogee or the perigee of orbit 2, whereas the perigee of orbit 3 coincides with that

of orbit 1. There are four solutions for the transfer from orbit 1 to orbit 2 (Fig. 4):

1 Perigee to apogee—orbits 1, 2 and 3 are in same sense.

2 Apogee to perigee—orbit 3 is in opposite sense to that of orbit 1 and 2.

3 Perigee to perigee—orbit 2 is in opposite sense to that of orbit 1 and 3.

4 Apogee to apogee—orbit 1 is in opposite sense to that of orbits 2 and 3.

For each solution, its first and second variation are examined.

For the perigee to apogee transfer, the values of e_3 and p_3 are given by the equations

$$\frac{1+e_1}{p_1} = \frac{1}{(r_p)_1} = \frac{1+e_3}{p_3} \qquad [12a]$$

$$\frac{1-e_2}{p_2} = \frac{1}{(r_a)_2} = \frac{1-e_3}{p_3} \qquad [12b]$$

The true anomaly of the point of transfer from orbit 1 to orbit 3 is zero and that from orbit 3 to orbit 2 is π with $\varphi_1 = \varphi_2 = 0$, where φ_1 and φ_2 denote the true anomaly of the perigee of orbit 3 with respect to orbits 1 and 2, respectively.

The change of velocity at the perigee and the apogee are

$$\mathrm{I}_1 = \frac{1}{\sqrt{\mu}}(\Delta V)_p = \frac{1+e_3}{p_3}(\sqrt{p_3} - \sqrt{p_1}) \qquad [13a]$$

$$\mathrm{I}_2 = \frac{1}{\sqrt{\mu}}(\Delta V)_a = \frac{1-e_3}{p_3}(\sqrt{p_2} - \sqrt{p_3}) \qquad [13b]$$

The small variation of this solution can be represented in general as (Fig. 5) a transfer orbit of semilatus rectum p_3' and eccentricity e_3' with

$$p_3' = p_3(1+\sigma) \qquad \sigma \ll 1 \qquad [14a]$$

$$e_3' = e_3 + \epsilon \qquad \epsilon \ll 1 \qquad [14b]$$

intersecting orbit 1 at (r_1, δ_1) and orbit 2 at $(r_2, \pi - \delta_2)$. The true anomalies of the corresponding points with respect to the transfer orbit are, respectively, δ_3 and $\pi - \delta_4$. The angles $\delta_3 - \delta_1$ and $\delta_4 - \delta_2 - (\delta_3 - \delta_1)$ represent the new orientations of the transfer orbit and orbit 2 with respect to orbit 1.

With $\delta_j \ll 1$ and $j = 1, 2, 3, 4$, σ and ϵ can be related to δ_j by Equations [1 and 12]

$$\frac{1}{r_1} = \frac{1+e_1\cos\delta_1}{p_1} \cong \frac{1+e_1}{p_1} - \frac{e_1\delta_1^2}{2p_1}$$

$$\frac{1}{r_1} = \frac{1+e_3'\cos\delta_3}{p_3'} \cong \frac{1+e_3}{p_3} - \frac{1+e_3}{p_3}\sigma + \frac{\epsilon}{p_3} - \frac{e_3\delta_3^2}{2p_3}$$

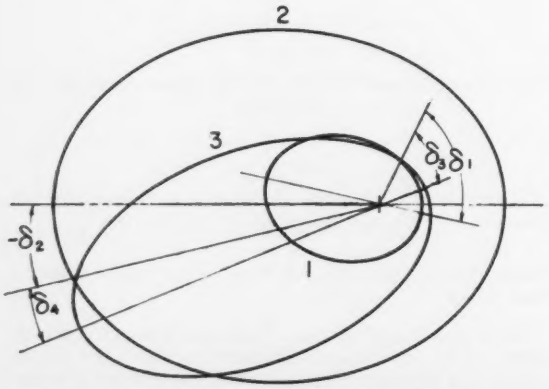

Fig. 5 Small variation of a solution of Equation [9]

$$\frac{1}{r_2} = \frac{1+e_2\cos(\pi-\delta_2)}{p_2} \cong \frac{1-e_2}{p_2} + \frac{e_2\delta_2^2}{2p_2}$$

$$\frac{1}{r_2} = \frac{1+e_3'\cos(\pi-\delta_4)}{p_3'} \cong \frac{1-e_3}{p_3} + \frac{e_3\delta_4^2}{2p_3} - \frac{\epsilon}{p_3} - \frac{1-e_3}{p_3}\sigma$$

Therefore

$$\frac{1+e_3}{p_3}\sigma - \frac{\epsilon}{p_3} = \frac{e_1\delta_1^2}{2p_1} - \frac{e_3\delta_3^2}{2p_3} \qquad [15a]$$

$$\frac{1-e_3}{p_3}\sigma + \frac{\epsilon}{p_3} = \frac{e_3\delta_4^2}{2p_3} - \frac{e_2\delta_2^2}{2p_2} \qquad [15b]$$

It is evident that ϵ and σ are of the order of δ_j^2.

At the point of transfer from orbit 1 to the transfer orbit, Equations [2] for the radial and circumferential velocities become

$$\frac{v_1}{\sqrt{\mu}} \cong \frac{e_1\delta_1}{\sqrt{p_1}} \qquad \frac{v_3}{\sqrt{\mu}} \cong \frac{e_3\delta_3}{\sqrt{p_3}}$$

$$\frac{(u_3-u_1)}{\sqrt{\mu}} = \frac{(\sqrt{p_3'} - \sqrt{p_1})}{r_1} \cong \mathrm{I}_1 + K_p$$

where I_1 is defined by Equation [13a] and

$$K_p = \frac{1+e_3}{\sqrt{p_3}}\left(\frac{\sigma}{2}\right) - \frac{e_1\delta_1^2}{2p_1}(\sqrt{p_3} - \sqrt{p_1}) \qquad [16]$$

The change of velocity normalized by the factor $\sqrt{\mu}$ is

$$|\mathrm{I}_1'| = \sqrt{[(u_3-u_1)^2 + (v_3-v_1)^2]/\mu} = |\mathrm{I}_1| + [\mathrm{I}_1 K_p + (v_3-v_1)^2/2\mu]/|\mathrm{I}_1|$$

and the variation in the change of the normalized velocity is

$$|\mathrm{I}_1'| - |\mathrm{I}_1| = K_p(\mathrm{sg}\ \mathrm{I}_1) + \tfrac{1}{2}(v_3-v_1)^2/(|\mathrm{I}_1|\mu) \qquad [17a]$$

where $(\mathrm{sg}\ \mathrm{I}_1)$ means sign of I_1.

Similarly, the variation in the change of the normalized velocity during the transfer from orbit 3 to orbit 2 is

$$|\mathrm{I}_2'| - |\mathrm{I}_2| = K_a(\mathrm{sg}\ \mathrm{I}_2) + \tfrac{1}{2}(v_4-v_2)^2/(|\mathrm{I}_2|\mu) \qquad [17b]$$

where

$$v_2 \cong e_2\delta_2/\sqrt{p_2}$$

$$v_4 \cong e_3\delta_4/\sqrt{p_3}$$

and

$$K_a = \{(\sqrt{p_2} - \sqrt{p_3})e_2\delta_2^2/p_2 - \sigma(1-e_3)/\sqrt{p_3}\}/2 \qquad [18]$$

The total variation is

$$|\mathrm{I}_1'| - |\mathrm{I}_1| + |\mathrm{I}_2'| - |\mathrm{I}_2| = K_a(\mathrm{sg}\ \mathrm{I}_2) + K_p(\mathrm{sg}\ \mathrm{I}_1) + \frac{1}{2}\left\{\frac{(v_2-v_4)^2}{|\mathrm{I}_2|\mu} + \frac{(v_1-v_3)^2}{|\mathrm{I}_1|\mu}\right\}$$

$$= \frac{1}{2|\mathrm{I}_1|}(a_1\delta_3^2 + 2b_1\delta_1\delta_3 + c_1\delta_1^2) + \frac{1}{2|\mathrm{I}_2|}(a_2\delta_4^2 + 2b_2\delta_4\delta_2 + c_2\delta_2^2) \qquad [19]$$

In the derivation of Equations [12 to 19], the restriction of Equation [10a] has not been imposed; therefore, they are valid for any combination of the initial and final orbits.

The expression on the right-hand side of Equation [19] is a linear combination of $\delta_i\delta_j$. It is a second variation since the first variation of $|\mathrm{I}_1| + |\mathrm{I}_2|$ vanishes. It will be explained later how to change the sign of e so that Equations [12 to 19] hold for other solutions of Equation [9]. The disappearance of terms of first variation verifies that solutions of Equation [9] are extremal solutions.

The uncoupling of δ_1 and δ_3 from δ_4 and δ_2 obviously simplifies the study of the second variation.

For the perigee-apogee transfer between two orbits sub-

jected to the restriction of Equation [10a], it is clear that $p_2 > p_3 > p_1$, and sg I_1 and sg I_2 are both equal to 1. With the definitions of the six coefficients in Equation [19], it follows that

$$a_1 = \tfrac{1}{2}e_3^2[1 - e_3 + \sqrt{(1 + e_3)(1 + e_1)}]/p_3 \qquad [20a]$$

$$a_1c_1 - b_1^2 = e_1e_3^3(1 + e_3)(3 - e_3)(\sqrt{p_3} - \sqrt{p_1})^2/(4p_1p_3^2) \qquad [20b]$$

$$a_2 = \tfrac{1}{2}e_3^2[1 + e_3 + \sqrt{(1 - e_3)(1 - e_2)}]/p_3 \qquad [21a]$$

$$a_2c_2 - b_2^2 = e_2e_3^3(1 - e_3)(3 + e_3)(\sqrt{p_2} - \sqrt{p_3})^2/(4p_2p_3^2) \qquad [21b]$$

It is obvious that $a_1 > 0$, $a_1c_1 - b_1^2 > 0$, $a_2 > 0$ and $a_2c_2 - b_2^2 > 0$ for all possible combinations of e_1, e_2, p_1 and p_2 subjected to the condition of Equation [11a]. Consequently, the second variation of $|I_1| + |I_2|$ given by Equation [19] is positive definite, and the perigee-apogee transfer represents a local minimum solution.

For the apogee-perigee transfer, Equations [12 to 20] hold if e_1 and e_2 are replaced respectively by $-e_1$ and $-e_2$. Consequently, $a_1c_1 - b_1^2$ is less than 0 and $a_2c_2 - b_2^2$ is less than 0, and the apogee-perigee transfer does not represent a minimum solution.

For the perigee-perigee transfer, all those equations hold if e_2 is replaced by $-e_2$. Consequently, $a_2c_2 - b_2^2$ is less than 0, and the perigee-perigee transfer does not represent a minimum solution.

For the apogee-apogee transfer, all those equations hold if e_1 is replaced by $-e_1$. Consequently, $a_1c_1 - b_1^2$ is less than 0, and the apogee-apogee transfer does not represent a minimum solution.

In conclusion, only the perigee to apogee transfer represents a local minimum solution for transfers from orbit 1 to 2 which do not intersect each other at any orientation.

Combination II—Initial and Final Orbit Always Intersect Each Other

Owing to the restriction of Equation [10b], the extreme solutions for the transfer from orbit 1 to 2 are perigee to apogee, apogee to perigee, perigee to perigee and apogee to apogee as shown in Fig. 6. The orientation of the transfer orbit for the apogee to perigee transfer and that for the apogee to apogee transfer are 180 deg out of phase from the corresponding ones in Fig. 4.

For the perigee to apogee transfer, Equations [12 to 19] hold. From Equations [12 and 10b] it is clear that

$$p_3 < p_1 \qquad p_3 < p_2 \qquad [22a]$$

$$\text{sg } I_1 = -1 \qquad \text{sg } I_2 = 1 \qquad [22b]$$

After the evaluation of the six coefficients in Equation [19], the following is obtained

$$a_1 = \tfrac{1}{2}e_3[-1 + e_3 + \sqrt{(1 + e_3)(1 + e_1)}\,]/p_3 \qquad [23a]$$

$$a_1c_1 - b_1^2 = e_1e_3(1 + e_3)(3 - e_3)(\sqrt{p_1} - \sqrt{p_3})^2/(4p_1p_3^2) \qquad [23b]$$

$$a_2 = \tfrac{1}{2}e_3[-\sqrt{(1 - e_3)(1 - e_2)} + (1 + e_3)]/p_3 \qquad [24a]$$

$$a_2c_2 - b_2^2 = e_2e_3(1 - e_3)(3 + e_3)\ (\sqrt{p_2} - \sqrt{p_3})^2/(4p_2p_3^2) \qquad [24b]$$

It is clear that $a_1 > 0$, $a_2 > 0$, $a_1c_1 - b_1^2 > 0$ and $a_2c_2 - b_2^2 > 0$, and the perigee-apogee transfer represents a local minimum solution.

For the apogee-perigee transfer, Equations [12 to 19] and [23 to 24] hold, if negative signs are added to e_1, e_2 and e_3. Consequently, the apogee-perigee transfer also represents a local minimum solution.

By changing the sign of e in those equations it can be shown

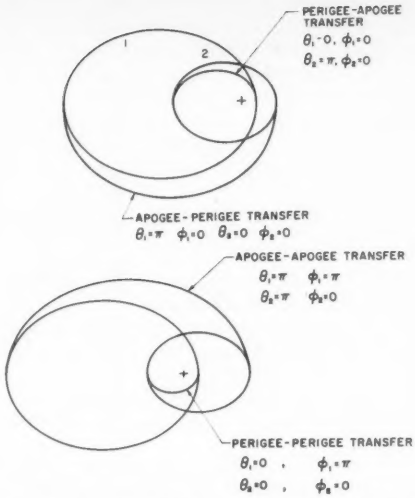

Fig. 6 Combination II—initial and final orbits always intersect each other

(9) that neither the perigee-perigee transfer nor the apogee-apogee transfer represents a minimum solution.

There are two local minimum solutions, the perigee-apogee transfer and the apogee-perigee transfer. The total impulse or the sum of the absolute values of the changes of velocities corresponding to one of those two minimum solutions will be compared with that of the other, so as to determine which solution of transfer requires less impulse.

For the perigee to apogee transfer, the total impulse required is proportional to I_{p-a} which, according to Equations [12, 13 and 22], is

$$I_{p-a} = |I_1| + |I_2| = \frac{1 + e_1}{\sqrt{p_1}} + \frac{1 - e_2}{\sqrt{p_2}} - \frac{2}{\sqrt{p_3}} \qquad [25]$$

For the apogee to perigee transfer, the geometries of the transfer orbit are given by the equations

$$\frac{1 - e_4}{p_4} = \frac{1 - e_1}{p_1} < \frac{1 - e_2}{p_2} \qquad \frac{1 + e_4}{p_4} = \frac{1 + e_2}{p_2} < \frac{1 + e_1}{p_1} \qquad [26]$$

It is evident that $p_4 > p_1$ and $p_4 > p_2$, and the total impulse required is proportional to I_{a-p} which is

$$I_{a-p} = \frac{(1 - e_1)\,|\sqrt{p_4} - \sqrt{p_1}|}{p_1} + \frac{(1 + e_2)\,|\sqrt{p_2} - \sqrt{p_4}|}{p_2}$$

$$= \frac{2}{\sqrt{p_4}} - \frac{1 - e_1}{\sqrt{p_1}} - \frac{1 - e_2}{\sqrt{p_2}}$$

The difference of impulse required is proportional to

$$I_{p-a} - I_{a-p} = \frac{2}{\sqrt{p_1}} + \frac{2}{\sqrt{p_2}} - \frac{2}{\sqrt{p_3}} - \frac{2}{\sqrt{p_4}} \qquad [27]$$

From Equations [10b, 12 and 26] it can be shown that

$$\frac{1}{p_3p_4} - \frac{1}{p_1p_2} = \frac{[(r_a)_2 - (r_a)_1]\ [(r_p)_2 - (r_p)_1]}{4(r_a)_1(r_a)_2(r_p)_1(r_p)_2} < 0$$

$$\left[\frac{1}{\sqrt{p_1}} + \frac{1}{\sqrt{p_2}} + \frac{1}{\sqrt{p_3}} + \frac{1}{\sqrt{p_4}}\right][I_{p-a} - I_{a-p}] = \frac{4}{\sqrt{p_1p_2}} - \frac{4}{\sqrt{p_3p_4}} > 0 \qquad [28]$$

Therefore, the perigee-apogee transfer is not a minimum solution as compared to the apogee-perigee transfer. For the latter, the apogee of the transfer orbit coincides with that of orbit 1. Since $(r_a)_1 > (r_a)_2$, it is concluded that the transfer from the apogee of the orbit with longer apogee distance to the perigee of the other orbit represents a minimum solution. This statement is also applicable for the optimum transfer between two orbits of combination I.

Combination III—Initial and Final Orbit Intersect Each Other at Certain Orientation

Owing to the restriction of Equation [11c], p_1 is less than p_2. The four extreme solutions are shown in Fig. 7. The orientation of the transfer orbit for the apogee-perigee transfer is 180 deg out of phase from the corresponding one in Fig. 4.

For the perigee to apogee transfer, Equations [12 to 21] hold, since $p_2 > p_3 > p_1$, and the transfer represents a local minimum solution.

For the apogee to perigee transfer, those equations again hold if negative signs are added to e_1, e_2 and e_3. This transfer also represents a local minimum solution.

By changing the sign of e in Equations [12 to 19, 23 and 24], it can be shown that neither the perigee-perigee transfer nor the apogee-apogee transfer represents a minimum solution.

Again there are two local minimum solutions, the perigee-apogee transfer and the apogee-perigee transfer. The corresponding transfer orbits are designated as orbits 3 and 4, respectively. With p_3 and p_4 both lying between p_2 and p_1, the difference of the impulses required corresponding to these two solutions is proportional to

$$\Delta = I_{p\to a} - I_{a\to p} = \frac{2e_3}{\sqrt{p_3}} + \frac{2e_4}{\sqrt{p_4}} - \frac{2e_1}{\sqrt{p_1}} - \frac{2e_2}{\sqrt{p_2}} \quad [29]$$

Δ is a function of e_1, e_2, p_1 and p_2. Proving that it is positive or negative in a straightforward procedure similar to Equations [27 and 28] has not been successful. Instead, it is shown in (9) that $\partial\Delta/\partial p_1 > 0$. Along the upper bound of p_1, according to Equation [11c], either the perigee or the apogee of orbit 1 coincides with that of orbit 2 and Δ vanishes. Therefore in region III of the p_1/p_2, e_2 plane (Fig. 3) $\Delta < 0$; i.e., the apogee-perigee transfer is not a minimum solution as compared to the perigee-apogee transfer. For the latter, the apogee of the transfer orbit coincides with that of orbit 2. Since $(r_a)_2 > (r_a)_1$ according to Equation [10c], the general statement regarding the optimum transfer between two orbits of combination II applies also for the present combination.

Concluding Remarks

It has been shown that the minimum impulse transfer from one given orbit to another of given geometry can be accomplished only when the two orbits and the transfer trajectory are co-planar.

If the two orbits can intersect each other at some relative orientation, the orbital transfer can be executed by a single impulse. The procedure of finding the optimum orientation has been presented.

The transfer from a given elliptical orbit to another of given geometry by two impulses has been studied. It is shown that the total impulse will be a minimum, provided that the two orbits and the transfer trajectory are co-planar, with the same major axis and oriented in the same sense, and provided that the apogee of the transfer trajectory coincides with that of the orbit, with longer apogee distance, and the perigee of the transfer trajectory coincides with that of the other orbit. This optimum transfer trajectory represents a generalization of Hohmann's transfer between two concentric circular orbits.

It should be pointed out that the solutions of Equation [9] are extremal solutions, but they may not necessarily represent all the extremal solutions. Investigation in this respect will be carried out.

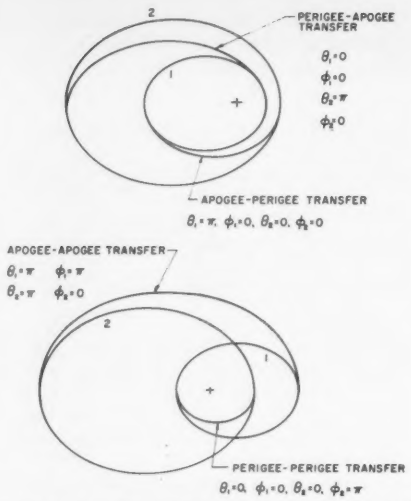

Fig. 7 Combination III—initial and final orbits can intersect each other at some orientations

If the two orbits can intersect each other, orbital transfer can be accomplished by either one or two impulses. By comparison of numerical results, the sum of the two impulses in the optimum transfer is always less than the corresponding optimum single impulse. An analytic proof of this statement is desirable. Although the transfer from one orbit to another can always be accomplished by two impulses, Shternfeld (10) and Hoelker and Silber (11) have shown that the transfer between two circular orbits can be accomplished more economically by three impulses if the ratio of the larger radius to the smaller one is greater than 11.9. As a generalization of their investigation, the optimum transfer between two elliptical orbits by three impulses or more has been studied (12).

Acknowledgment

This research was supported by the Army Ballistic Missile Agency, U. S. Army Ordnance Missile Command, Redstone Arsenal, Ala., Contract no. DA-30-069-ORD-2639, under the supervision of Professor Antonio Ferri, to whom the author is indebted for invaluable discussions.

References

1 Hohmann, W., "Die Erreichbarkeit der Himmelskörper," R. Oldenburg, Munich, 1925.

2 Lawden, D. F., "Inter-Orbital Transfer of a Rocket," *J. Brit. Interplanet. Soc.*, vol. 11, 1952, pp. 321–333.

3 Lawden, D. F., "Orbital Transfer via Tangential Ellipses," *J. Brit. Interplanet. Soc.*, vol. 11, 1952, pp. 278–289.

4 Munick, H., "An Optimum Transfer Path From an Elliptical Orbit to a Higher Energy Circular Orbit," ARS JOURNAL, vol. 29, no. 6, June 1959, pp. 449–451.

5 Pohle, F. V. and Feitis, P., "Annotated Bibliography of Astrodynamics and Re-entry Mechanics," Polytechnic Institute of Brooklyn, PIBAL Rep. no. 551, Aug. 1959.

6 Synge, J. L. and Griffith, B. A., "Principle of Mechanics," McGraw-Hill Book Co., N. Y., 2nd ed., 1949, pp. 168–184.

7 Loh, W. H. T., "Two Simple Equations for Orbital Mechanics," ARS JOURNAL, vol. 29, no. 2, Feb. 1959, pp. 146–147.

8 Ting, L., "Optimum Orbit Transfer by Impulse," Polytechnic Institute of Brooklyn, PIBAL Rep. no. 532, Aug. 1959.

9 Ting, L., "Optimum Orbital Transfer by Two Impulses," Polytechnic Institute of Brooklyn, PIBAL Rep. no. 536, Jan. 1960.

10 Shternfeld, A., "Soviet Space Science," Basic Books, Inc., N. Y., 1959, pp. 109–111.

11 Hoelker, R. F. and Silber, R., "The Bi-elliptical Transfer Between Circular Coplanar Orbits," Army Ballistic Missile Agency, Development Operations Division, Redstone Arsenal, Ala., Rep. no. DA-TM-2-59, Jan. 1959.

12 Ting, L., "Optimum Orbital Transfer by Several Impulses," Polytechnic Institute of Brooklyn, PIBAL Rep. no. 608, June 1960.

Relative Thermodynamic Efficiency of Supersonic Combustion and Subsonic Combustion Hypersonic Ramjets

GEORGE H. McLAFFERTY[1]

United Aircraft Corp.
East Hartford, Conn.

An analytical model is set up to permit comparison of the relative thermodynamic efficiencies (fuel consumption or specific impulse) of supersonic combustion and subsonic combustion hypersonic ramjets for arbitrary inlet performance. The results indicate that the specific impulse of a supersonic combustion ramjet will be superior to that of a subsonic combustion ramjet at Mach numbers above approximately 7 for configurations having isentropic spike external compression inlets and above 10 for configurations having internal compression inlets.

IN COMPARING the performance of conventional ramjets and ramjets having supersonic combustion, the Mach number of combustion and the total pressure losses in the inlet diffuser for the supersonic combustion ramjet should be identical to the Mach number upstream of the inlet normal shock and the total pressure losses owing to diffusion to this Mach number, respectively, for the subsonic combustion ramjet. Although several comparisons of supersonic combustion and subsonic combustion ramjets were made in (1),[2] none were made for the case where each ramjet type employed inlets having the same minimum supersonic Mach number and the same total pressure losses in the supersonic diffusion process.

The purpose of the study reported here was to determine the relative performance of the two ramjet types for the two cases where each system employs an isentropic spike external compression inlet and where each system employs an internal compression inlet. The study is based on a simple analytical model rather than on complete cycle studies such as those used in (1).

Discussion

Typical Mach numbers which might exist in a supersonic combustion hypersonic ramjet are shown in the upper part of Fig. 1. The Mach number at the inlet throat (M_1) was chosen so that the addition of fuel at an equivalence ratio ϕ of 0.5 would result in sonic flow at the burner exit.

Also shown in Fig. 1 is a subsonic combustion hypersonic ramjet operating with the same inlet throat Mach number, the same free stream Mach number (M_0) and the same equivalence ratio as the supersonic combustion ramjet shown at the top of the figure. The geometry of the subsonic combustion ramjet is unconventional in that the pressure rise through the normal shock and the combustion of the fuel take place in the same constant-area passage. If wall friction in the constant-area section is neglected, then the same input information (pressure, temperature and velocity) and equations (continuity, momentum and energy) are employed to calculate the change of properties across the combustor in the supersonic combustion ramjet as across the normal shock and combustor of the subsonic combustion ramjet. Usually there are two solutions to these equations, one indicating supersonic flow at Station 3 and the other indicating subsonic flow at Station 3. However, since the equivalence ratio was chosen to give a Mach number of unity at Station 3, the two solutions are identical, the conditions at Station 3 (pressure, temperature and velocity) are the same for both ramjets, and both ramjets would produce the same thrust with the same specific impulse or fuel consumption.

The effect of variations of equivalence ratio from the value employed in Fig. 1 on the ratio of burner exit total pressure to free stream total pressure (which determines specific impulse) for a fixed value of M_1 is shown in the upper part of Fig. 2. A decrease in equivalence ratio results in a relatively small reduction in the total pressure losses in the subsonic combustion ramjet, since the majority of the total pressure losses occur across the normal shock wave for this configuration. (A reduction in equivalence ratio requires a reduction

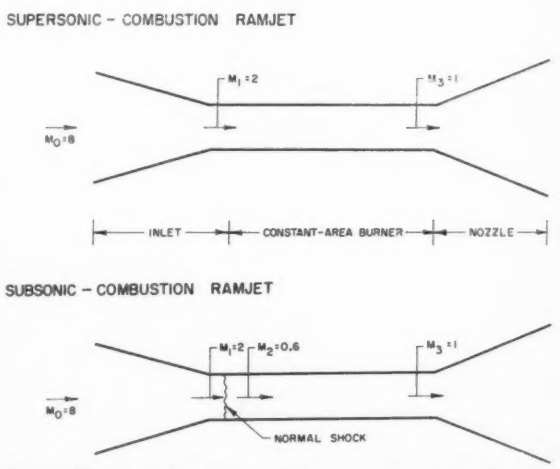

Fig. 1 Mach numbers in equal thrust supersonic combustion and subsonic combustion hypersonic ramjets. $M_0 = 8$, $\phi = 0.5$

Received Jan. 28, 1960.

[1] Assistant to Chief Research Engineer, Research Laboratories.

[2] Numbers in parentheses indicate References at end of paper.

in area at the burner exit to maintain proper matching of components in the subsonic combustion ramjet.) However, for the supersonic combustion ramjet, a reduction in the heat addition in the supersonic stream results in a large decrease in total pressure losses across the supersonic combustor and produces a supersonic rather than a sonic velocity at the burner exit. Conversely, the increase in total pressure losses resulting from an increase in equivalence ratio is much less for the subsonic combustion ramjet than for the supersonic combustion ramjet. If the equivalence ratio is increased above 0.5, it is necessary as a result of continuity considerations to have the combustion from the added fuel take place in an increased cross-sectional area. In the supersonic combustion ramjet, this additional combustion would take place in the divergent portion of the nozzle, thereby creating additional losses in total pressure. For the subsonic combustion case, however, it would be more advantageous to increase the area of the combustion chamber between the inlet throat and the exhaust nozzle throat in order to allow combustion of the increased amount of fuel.

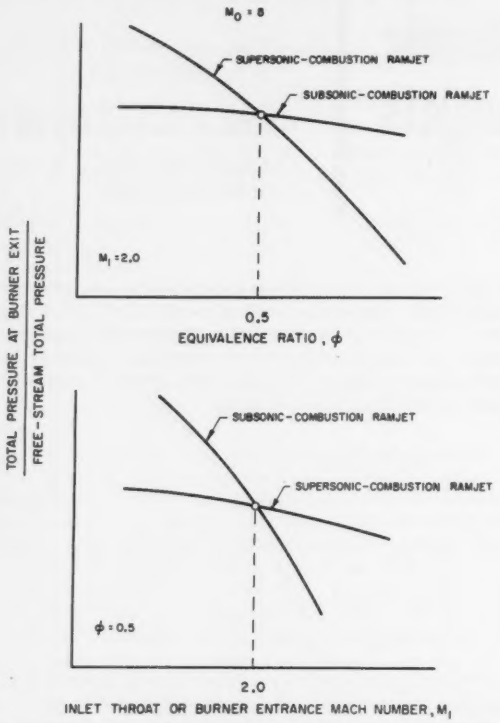

Fig. 2 Effect of equivalence ratio and inlet throat Mach number on total pressure losses in supersonic combustion and subsonic combustion hypersonic ramjets

Although the reasoning presented in the preceding paragraph was given in terms of a fixed Mach number at the inlet throat and a variable equivalence ratio, the same kind of reasoning can be used for a fixed equivalence ratio and a variable inlet throat Mach number (see lower half of Fig. 2). If the Mach number (M_1) provided by the inlet is greater than that which would result in $M_3 = 1$, then the supersonic combustion configuration is more efficient. Conversely, if the Mach number provided by the inlet is less than that which would result in $M_3 = 1$, then the subsonic combustion configuration is more efficient.

Since the breakeven free stream Mach number for supersonic combustion and subsonic combustion ramjets is a function of the Mach number delivered by the inlet to the throat of the configuration, it is of interest to examine the throat Mach numbers which would exist for various types of supersonic inlets. It can be shown that it is always desirable for both subsonic combustion and supersonic combustion ramjets to decrease the inlet throat Mach number as much as possible. (A decrease in M_1 in a subsonic combustion ramjet decreases the total pressure losses across the normal shock. A decrease in M_1 in a supersonic combustion ramjet decreases the total pressure losses in the combustion process, even though a decrease in M_1 in some cases might require that some of the combustion take place downstream of Station 3.) However, the minimum attainable value of M_1 for supersonic inlets is limited by various aerodynamic considerations. The variation of minimum attainable inlet throat Mach number with free stream Mach number is shown in Fig. 3 for three

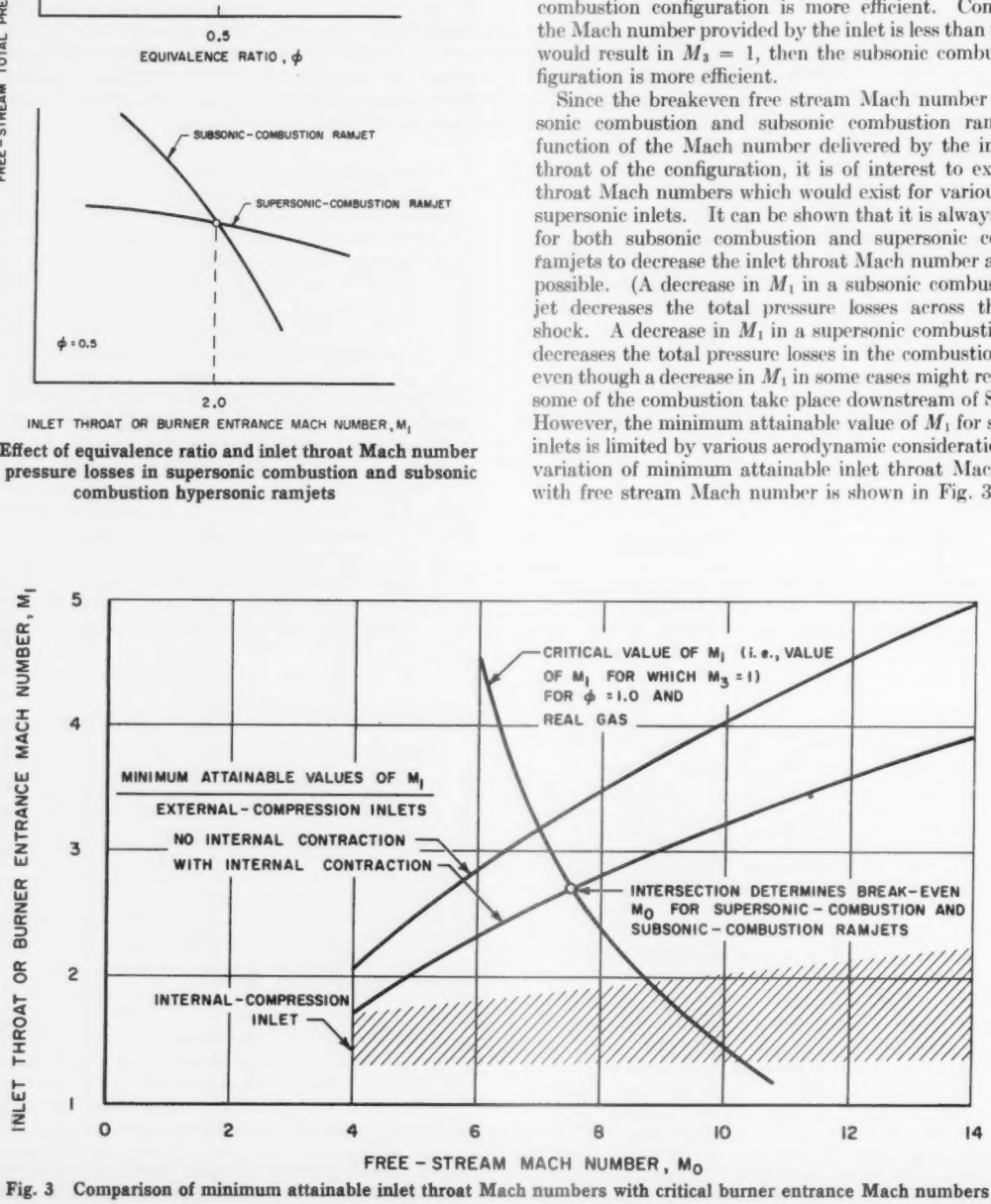

Fig. 3 Comparison of minimum attainable inlet throat Mach numbers with critical burner entrance Mach numbers

types of supersonic inlets: External compression inlets with no internal contraction, external compression inlets with internal contraction, and internal compression inlets. The curve shown for the external compression inlets with no internal contraction was obtained from a procedure which is similar to that outlined in (2), but which accounts for real gas effects and boundary layer growth. The minimum attainable Mach numbers for the external compression inlet with internal contraction shown in Fig. 3 were obtained by reducing those shown for the inlet with no internal contraction by the maximum allowable amount for fixed-geometry inlets. The range of minimum attainable throat Mach numbers shown for internal compression inlets was determined on the basis of experience obtained with these inlet types at the UAC Research Laboratories.

Also shown in Fig. 3 are critical values of burner entrance Mach number (i.e., values of burner entrance Mach number M_1 for which the addition of heat results in a Mach number of unity at the downstream end of the burner). The critical values of burner entrance Mach number shown in Fig. 3 were determined by a procedure which accounts for all real gas effects. As noted in a preceding paragraph, the Mach number at which supersonic combustion and subsonic combustion ramjets produce the same thermodynamic efficiencies is determined by the free stream Mach number at which the critical value of burner entrance Mach number is equal to the throat Mach number provided by the inlet. It is shown in Fig. 3 that the breakeven free stream Mach number varies from approximately 7 for external compression inlets to approximately 10 for internal compression inlets.

The critical value of burner entrance Mach number is a function of the fuel-air ratio and method of fuel injection in the burner. If the equivalence ratio is decreased below 1.0, the critical inlet throat Mach number will decrease slightly (this decrease is very small at high Mach numbers because the fuel added at high equivalence ratios results in an increase in dissociation rather than an increase in temperature). The critical burner entrance Mach numbers for equivalence ratios greater than 1.0 are also slightly less than those shown on Fig. 3 for an equivalence ratio equal to 1.0. Upstream injection of the fuel results in an increase in critical burner entrance Mach number from the values shown in Fig. 3.

The efficiency of a subsonic combustion configuration could be improved over that obtainable with the subsonic combustion configuration shown in Fig. 1 by increasing the area of the passage downstream of the inlet throat and by injecting and burning the fuel at the resulting reduced Mach number. Therefore, the breakeven free stream Mach numbers for this alternate, more conventional, subsonic combustion configuration would be higher than those given in Fig. 3.

It has been suggested that the weight of a supersonic combustion configuration would be less than that of a subsonic combustion configuration. Weight is determined by three factors: Pressure loads, length and cooling requirements. Although the pressures within a supersonic combustion configuration are less than those in a subsonic combustion configuration, it might be necessary to design the supersonic combustion configuration to provide for the possibility that a normal shock would be created inadvertently in the inlet throat. If this condition were considered, there would be no difference in weight owing to differences in pressure loads within the two configurations.

The overall length of a burner at high free stream Mach numbers is determined primarily by the length of the fuel injection portion of the burner. It seems doubtful that the fuel can be injected in a supersonic stream in a shorter distance than in a subsonic stream.

The rate of heat transfer to the ramjet duct wall per unit area at a given free stream Mach number is a function of the mass flow per unit duct area and the wall friction coefficient. Although there is no difference in the mass flow per unit area for the two configurations shown in Fig. 1, the friction coefficients in supersonic flow are slightly less than those in subsonic flow. Therefore, the heating load in the supersonic combustion configuration would be somewhat less than that in the subsonic combustion configuration if the supersonic burner could be made as short as the subsonic burner.

Dissociation of the products of combustion in high Mach number ramjets results in a loss in thrust if the reaction rates in the exhaust nozzle are not fast enough to maintain chemical equilibrium. For the equal-thrust configurations shown in Fig. 1, the static temperatures at Station 3 for chemical equilibrium at Station 3 are equal for the supersonic combustion ramjet and the subsonic combustion ramjet. For this case the chemical reaction rate in the exhaust nozzle has no influence on the breakeven free stream Mach number between supersonic combustion and subsonic combustion ramjets. If the flow at Station 3 is not in chemical equilibrium, the dissociation will be greater for the subsonic combustion ramjet than for the supersonic combustion ramjet, as a result of the higher static temperatures upstream of Station 3 for the subsonic combustion ramjet. This increased dissociation will cause a loss in thrust and serve to decrease the breakeven free stream Mach number from that determined by the construction given in Fig. 3.

Nomenclature

M_0 = free stream Mach number
M_1 = inlet throat or burner entrance Mach number
M_2 = Mach number behind normal shock in subsonic combustion configuration
M_3 = burner exit Mach number
ϕ = equivalence ratio, ratio of actual fuel flow to fuel flow for stoichiometric mixture

References

1 Weber, R. J. and MacKay, J. S., "An Analysis of Ramjet Engines Using Supersonic Combustion," NACA TN 4386, Sept. 1958.

2 Connors, J. F. and Meyer, R. C., "Design Criteria for Axisymmetric and Two-Dimensional Supersonic Inlets and Exits," NACA TN 3589, Jan. 1956.

Effect of Nonlinear Losses on the Design of Absorbers for Combustion Instabilities

A. W. BLACKMAN[1]

United Aircraft Corp.
East Hartford, Conn.

Investigations were conducted to provide a basis for the design of multiple-resonator absorbers to control high amplitude combustion instabilities (screech) in high output combustors. An impedance tube technique was employed to determine the effect of high amplitude sound pressure waves on the absorption characteristics of absorber configurations having open areas varying between 0.5 and 10 per cent. Frequencies were varied between 200 and 1200 cps. It was found that the acoustical impedance of the absorbers contains a nonlinear facing resistance which depends on the oscillating velocity and particle displacement in the absorber neck, and that the nonlinear resistance can generally be correlated with the amplitude of the incident pressure wave plotted on a decibel scale. A design procedure is presented in which the absorption characteristics of perforated liners for a particular sound wave amplitude can be calculated from known physical dimensions.

SCREECH is a type of combustion instability encountered in high output combustors, such as those used in rockets, ramjets and turbojet afterburners. It is characterized by high amplitude pressure and flame front oscillations which occur at one of the resonant frequencies of the combustion chamber. These oscillations increase heat transfer and stress repetition rates, and usually cause failure of structural components of the combustion chamber in a matter of seconds. It is obvious that combustion instabilities of this type must be avoided.

Previous investigations have shown that screech pressure oscillations can be suppressed by lining the combustion chamber with a perforated metal sheet to absorb the kinetic energy of the oscillations in much the same manner that a Helmholtz resonator absorbs sound. The problem of screech liner design is one of adapting the simple Helmholtz resonator theory to the conditions of high pressure amplitude that exist when screech occurs. Previous investigations of single resonator configurations (1)[2] have shown that absorption is a function of pressure wave amplitude when the amplitude level is greater than about 100 db. This relationship is obtained at the higher amplitudes because a resonator contributes a nonlinear resistance to the sound wave in addition to the linear resistance. This increase in resistance results from changes in the circulation and turbulence of the gas particles at the neck of the resonator as the pressure wave amplitude or particle velocity increases. At levels greater than about 100 db, the nonlinear resistance becomes a controlling factor in determining the absorption characteristics of a resonator. This resistance has been measured for certain limited conditions, but has not been quantitatively expressed for the perforated plate, i.e., the resonator array.

The purpose of the investigation described in this paper was to determine the effects of high amplitude pressure waves on the absorption characteristics of multiple resonator absorbers and to incorporate these results in the development of a design procedure for screech absorption liners.

Received Jan. 14, 1960.

[1] Supervisor, Chemical Kinetics Group, Propulsion Section, Research Laboratories. Member ARS.

[2] Numbers in parentheses indicate References at end of paper.

Theoretical Considerations

Resonator Array

Fig. 1 illustrates an array of closely spaced resonators typical of configurations used in screech absorption liners. If the perforated area is assumed to have a uniform impedance, the absorption coefficient (defined as the fractional part of the energy of an incident sound wave absorbed by the liner) can be written for normal incident waves (2) as

$$\alpha = 4\tilde{\theta}/[(\tilde{\theta} + 1)^2 + \tilde{\chi}^2] \qquad [1]$$

where $\tilde{\theta}$ is the specific acoustic resistance ratio and $\tilde{\chi}$ is the specific acoustic reactance ratio, which can be expressed as

$$\tilde{\chi} = \left(\frac{2\pi f_0 l_{eff}}{c\sigma}\right)\left(\frac{f}{f_0} - \frac{f_0}{f}\right) \qquad [2]$$

Hence

$$\alpha = \frac{4\tilde{\theta}}{(1 + \tilde{\theta})^2 + \left(\frac{2\pi f_0 l_{eff}}{c\sigma}\right)^2 \left(\frac{f}{f_0} - \frac{f_0}{f}\right)^2} \qquad [3]$$

which for $\tilde{\theta} = 1$ and $f = f_0$ gives $\alpha = 1$.

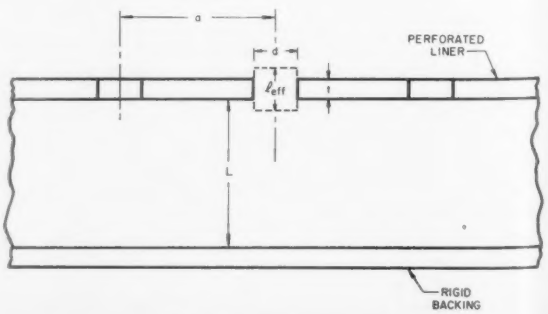

Fig. 1 Resonator array

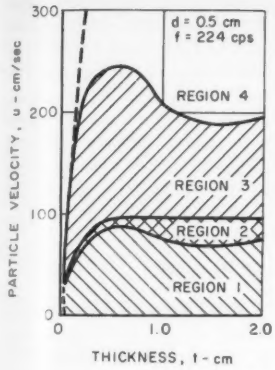

Fig. 2a Aperture phase diagram showing regions of acoustic streaming and turbulence particle velocity vs. plate thickness (1)

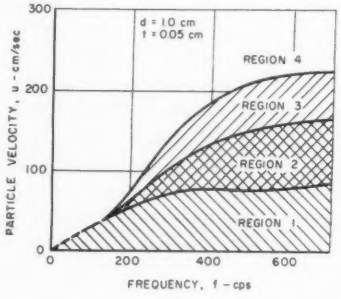

Fig. 2b Aperture phase diagram showing regions of acoustic streaming and turbulence particle velocity vs. frequency (1)

The assumption of uniform impedance applies only if the distance a between the centers of the resonator necks spaced in a square array is less than $\lambda/(2\pi)^{1/2}$ (approximately one half wave length) and greater than the diameter d of the aperture (1,3). For values of $a > \lambda/(2\pi)^{1/2}$, the individual resonators should act independently, and the total absorption should be determined as the sum of the individual absorption cross sections of the resonators. For values of a approaching d, the resonators should probably be treated as a pure resistive load with no reactance. The dimensions of all practical liners for screech absorption are expected to fall within the range where the assumption of uniform impedance applies.

If the pressure waves striking the absorber are not of normal incidence (4)

$$\alpha_\phi = \frac{4\bar{\theta}\cos\phi}{(\bar{\theta}\cos\phi + 1)^2 + \left(\frac{2\pi f_0 l_{eff}}{c\sigma}\right)^2 \left(\frac{f}{f_0} - \frac{f_0}{f}\right)^2 \cos^2\phi} \qquad [4]$$

Partitions located in the resonator volume behind the perforated plates are generally necessary if the pressure waves are not of normal incidence; however, for normal incident waves, partitions have little or no effect on the absorption characteristics.

Effect of High Intensities on Absorption Characteristics of Resonators

Previous investigators have shown that the absorbing characteristics of resonators are materially different when exposed to high amplitude sound waves rather than low amplitude sound waves. The most thorough investigations of this phenomenon, as reported in (1 and 5), have shown that the flow of air particles in and out of the resonator neck can be classified in one of four regions. Phase diagrams of these regions are presented in Figs. 2a and 2b. Region 1 is a low intensity sound region with stationary circulation; the flow is directed out of the orifice along the orifice axis. Region 2 is a region of stationary circulation in which the direction of flow along the axis is toward the orifice. Region 3 is characterized by pulsing effects superposed on circulation of the kind in Region 2. Region 4 is a high intensity sound region in which pulsatory effects predominate and result in the formation of jets and vortex rings.

The losses contributed by the turbulence and circulation associated with these flow regions are nonlinear and similar to those caused by the facing and aperture resistance; they may be incorporated in the equation for resonator resistance by a term Δ_{nl} to give

$$\bar{\theta} = \frac{4}{\sigma\rho c}\left(\frac{\pi\mu\rho f}{g}\right)^{1/2}\left(1 + \frac{t}{d} + \frac{\Delta_{nl}}{d}\right) \qquad [5]$$

where the terms 1, t/d and Δ_{nl}/d represent the facing, neck and circulation losses respectively.

At incident wave pressure levels of the order of 100 db, the nonlinear losses represent a significant part of the total resistance. When the levels are as large as 130 db, the total resistance is almost entirely a result of this term. Since screech pressure levels are of such order of magnitude, it is essential that the Δ_{nl} term be accurately known for the design of screech liners. Some evidence also indicates that additional nonlinear terms should be included if there is flow past or through the resonator face (6). In the work described here, these losses have been assumed to be small relative to the intensity dependent loss and have not been included.

Some work has been done to determine the nonlinear losses as a function of operating variables (1), and the results have been expressed in accordance with the phase diagrams previously mentioned; i.e., the nonlinear resistance is correlated with a variable whose relation to the region boundaries is known. It was found that the onset of the turbulent regions in the phase diagrams (Figs. 2a and 2b) was a function of frequency f, particle velocity u and resonator aperture thickness t. A critical thickness was defined as

$$t_c = u_c/2\pi f \qquad [6]$$

where u_c is the velocity corresponding to the lower boundary of Region 3. The dashed lines in Figs. 2a and 2b correspond to $u = 2\pi ft$ in which the particle displacement in the aperture equals the aperture thickness t. For sufficiently large values of t ($t > t_c$), the turbulence onset occurs approximately at a constant value of u and is independent of the aperture thickness t. If $t < t_c$, the criterion for the onset of turbulence is $s/t \leqq 1$, where s is the particle displacement amplitude. The critical thickness t_c was found to be of the order of 0.0236 in. (1).

The nonlinear resistance was found to be consistent with the observations on turbulence. For $t < t_c$, the nonlinear resistance depends essentially on s/t, but for $t > t_c$ the particle velocity amplitude is the governing variable. Ingard's results (1) were of limited value when applied to screech liner design because multiple resonator effects, frequency variation and reactive loading were not considered. It was a purpose of the work described here to consider these effects.

Apparatus and Procedure for Experimental Investigation

Method of Measuring Absorption Coefficients

The impedance tube technique was utilized to measure the absorption coefficients of the various test configurations. It can be shown (7) that the absorption coefficient can be determined by placing the test configuration at the end of a tube which is excited at a resonant frequency by some driving source and by measuring the magnitude of the pressure maxima and minima of the standing wave pattern in the tube and the distance between the pressure maxima and minima.

Determination of Natural Frequency

The natural frequency of a resonator configuration is the frequency at which the resonator offers no specific reactance

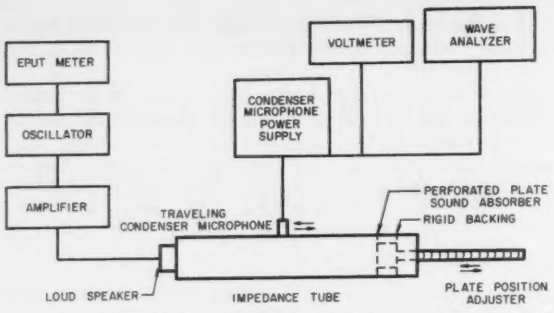

Fig. 3 Instrumentation diagram for impedance tube method of sound absorption measurement

$\tilde{\chi}$ to the sound wave. This frequency, called the resonant frequency, can be expressed as follows for the resonator array

$$f_0 = \frac{c}{2\pi}\sqrt{\frac{\sigma}{Ll_{eff}}} \qquad [7]$$

Because the ratio of the minimum pressure amplitude to the maximum pressure amplitude of the standing wave in the impedance tube is a maximum at resonance, it was determined that a plot of p_{min}/p_{max} vs. frequency was a suitable method for obtaining a value of f_0 from experimental data. A plot of the minimum pressure position vs. frequency was used as a check.

Test Configurations

All configurations were designed so both the backing distance and the position of the test configuration in the impedance tube could be varied. Aperture plates were cut from $\frac{1}{16}$-in. steel sheets. The per cent open area of the test configurations varied between 0.5 and 10 per cent. Apertures were spaced in a symmetrical square array so the openings had an equivalent absorbing or working area. Apertures could not be spaced around the outer portion of the plate because of the lack of symmetry which this would have produced. However, additional holes were added around the edges of one configuration to determine if these holes changed the absorption characteristics appreciably. There did not appear to be a significant difference between the two cases.

Impedance Tube

The impedance tube was a 4-in. diameter brass tube about 4 ft long. One end of the tube was closed with the perforated plate absorption configuration. At the other end, a loudspeaker was placed which propagated sound waves of controlled frequency and intensity. The incident wave added to the sound wave reflected from the surface of the absorber to result in a standing wave along the tube. A traveling microphone inserted in a slit cut along the upper length of the impedance tube indicated the position and amplitude of the maximum and minimum pressure points from which the absorption coefficient was determined.

The resistance of the tube was measured and was found to cause negligible attenuation.

Instrumentation

The test equipment used for this investigation is illustrated in Fig. 3. The frequency was determined by means of a Berkeley EPUT meter and a Hewlett-Packard oscillator. For a particular sound pressure level intensity the frequency was set so the pressure amplitude at the plate would be maximized. The maximum pressure amplitude of the standing wave was adjusted by means of a Fisher amplifier and measured with a General Radio condenser microphone pickup system and a Hewlett-Packard harmonic wave analyzer. A Ballantine voltmeter was used to indicate the occurrence of a maximum pressure amplitude at the plate. The voltmeter was not used for recording actual pressures because it lacked the filter medium of the analyzer. Microphone pickup tubes of different diameters were used in order to measure pressures accurately over a large range of intensities.

Discussion of Experimental Results

The absorption characteristics of test configurations having open areas varying between 0.5 and 10 per cent were determined for various frequencies at pressure levels between 100 and 160 db. The impedance tube technique was utilized; measurements allowed computation of the real and imaginary parts of the impedance for the various test conditions.

Effect of Intensity Level on Absorption at Resonance

From experimentally determined values of the resonant frequency and facing resistance, it was possible to compute the nonlinear resistance factor Δ_{nl}/d at the various pressure levels from Equation [5]. Following Ingard's procedure (1), attempts were made to correlate the nonlinear resistance factor with both the particle velocity and particle displacement in the neck of the resonator. The particle velocities and displacements were calculated from the following equation (2)

$$u = 2\pi f s = \left| \frac{2P_i}{\sigma\rho c\left[(\tilde{\theta}+1) + i\,\frac{2\pi f_0 l_{eff}}{\sigma c}\left(\frac{f}{f_0} - \frac{f_0}{f}\right)\right]} \right| \qquad [8]$$

Fig. 4a shows that the nonlinear resistance can be correlated with the particle velocity of the liner configuration. The method of least squares was used to determine the location of the solid line through the experimental data; the dashed line corresponds to the data obtained for a single resonator configuration (1). The solid line can be expressed empirically as

$$\log_{10}(\Delta_{nl}/d) = -0.009 + 0.400\log_{10}(u) \qquad [9]$$

It can be seen that some divergence exists between the slope of the two lines. Presumably this results from the coupling of the multiple resonators. The particle velocities were usually relatively high, and the acoustic jet (Region 4 of Figs. 2a and 2b) should have been formed under most conditions. Ingard (1) indicates that the nonlinear resistance should correlate with particle velocity if the aperture thickness is above a critical value and with the ratio of the particle displacement to the aperture thickness if the aperture thickness is below the critical value. Although the aperture thickness used in this investigation was greater than the critical thickness given by Ingard (1), Fig. 4b shows that some degree of correlation does exist between the nonlinear resistance and the particle displacement. Again, the method of least squares was used to determine the location of the solid line through the experimental data points; the dashed line corresponds to the data given by Ingard (1) for a single resonator configuration. The solid line is given by the empirical equation

$$\log_{10}\left(\frac{\Delta_{nl}}{d}\right) = 0.516 + 0.482\log_{10}\left(\frac{s}{l}\right) \qquad [10]$$

The scattering of points indicates that the nonlinear resistance is really a complex function of many variables, but it will be shown later that the degree of correlation which exists is adequate for design purposes.

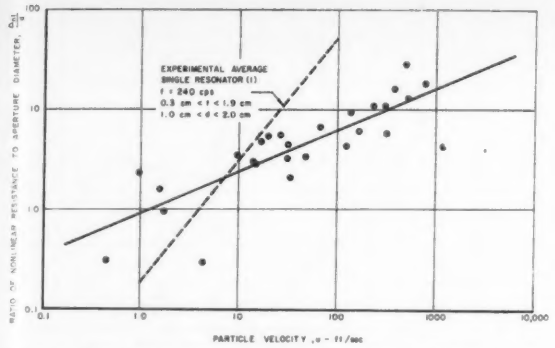
EXPERIMENTAL AVERAGE
SINGLE RESONATOR (1)
f = 240 cps
0.5 cm < t < 1.9 cm
1.0 cm < d < 2.0 cm
RATIO OF NONLINEAR RESISTANCE TO APERTURE DIAMETER, Δnl/d
PARTICLE VELOCITY, u - ft/sec

Fig. 4a Nonlinear resistance vs. particle velocity in the aperture

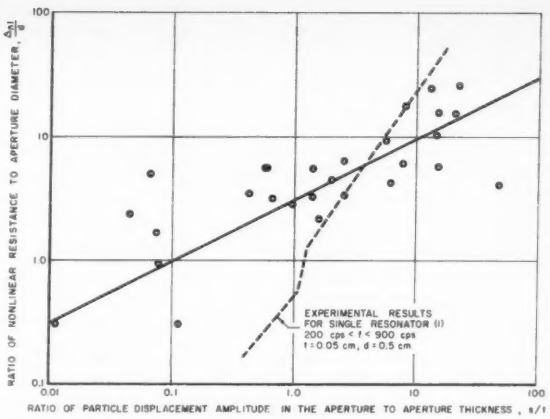
EXPERIMENTAL RESULTS
FOR SINGLE RESONATOR (1)
200 cps < f < 900 cps
t = 0.05 cm, d = 0.5 cm
RATIO OF NONLINEAR RESISTANCE TO APERTURE DIAMETER, Δnl/d
RATIO OF PARTICLE DISPLACEMENT AMPLITUDE IN THE APERTURE TO APERTURE THICKNESS, s/t

Fig. 4b Nonlinear resistance vs. particle displacement amplitude in the aperture

By plotting the sound pressure level vs. the nonlinear resistance, a fair degree of correlation was obtained as shown in Fig. 5. The solid line through the data points was determined by the method of least squares and can be expressed as

$$\log_{10}(\Delta_{nl}/d) = -1.685 + 0.0185\ (\text{db}) \qquad [11]$$

The degree of fit is somewhat misleading, since the pressure amplitude doubles with a mere 6-db increase. However, this presentation is a satisfactory and convenient correlation for liner design purposes because the absorption coefficient is rather insensitive to variations in the nonlinear resistance term. For the accuracies presently required for screech absorber design, it is suggested that the correlation of Fig. 5 be used for determining the nonlinear resistances for per cent open areas between approximately 0.5 and 10 per cent. The use of Fig. 5 for design purposes is discussed in more detail in the subsection titled "Improvements in Accuracy of Design System."

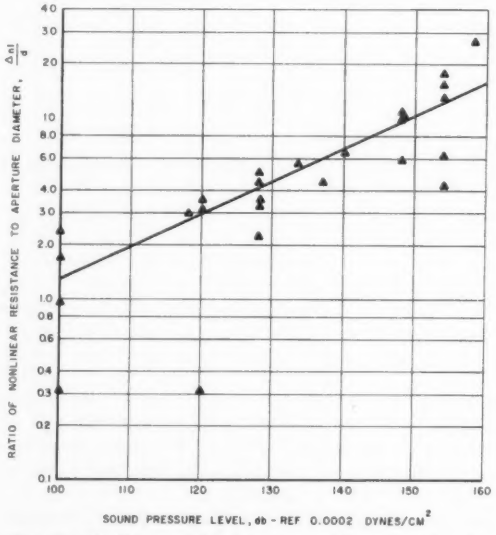

Fig. 5 Nonlinear resistance vs. sound pressure level

Effect of Intensity Level on Absorption at Nonresonant Conditions

The correlations presented previously apply rigorously only at resonant conditions where the reactive part of the impedance is zero and the mass in the aperture neck vibrates in phase with the incident wave. It is of some practical interest to be able to determine the absorption characteristics of screech liners at off-resonance conditions, for the liner natural frequency does not necessarily correspond to the screech frequency for an optimum liner design. The reactance of a multiresonator absorber can be computed for various frequencies from Equation [2], and the absorber facing resistance can be computed from Equation [5]. The absorption coefficient can be expressed in terms of the reactance and resistance using Equation [1]. Figs. 6a and 6b present experimental data on specific acoustical reactance and resistance typical of data obtained for the various liner configurations. Fig. 6a shows that the reactance increases

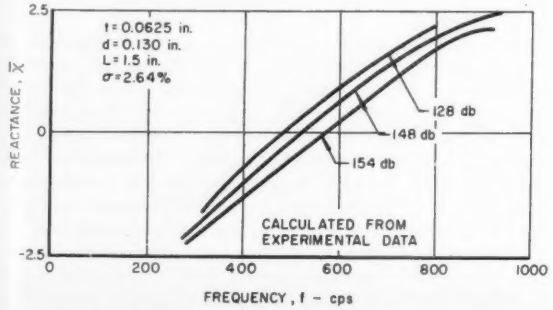

Fig. 6a Specific acoustical reactance vs. frequency

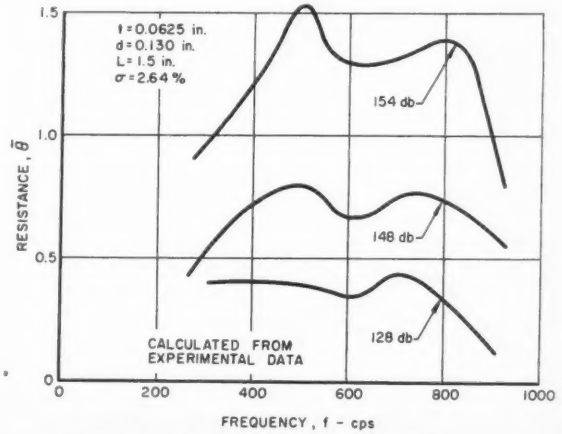

Fig. 6b Specific acoustical resistance vs. frequency

with frequency and decreases slightly with increasing sound pressure level. This result is in agreement with Ingard's findings (1).

Fig. 6b shows the variation of the facing resistance $\bar{\theta}$ with frequency. From Equation [5] it can be seen that if Δ_{ni}/d were independent of frequency, $\bar{\theta}$ would vary with $f^{1/2}$. This is evidently not the case. No consistent relationship could be found between the facing resistance $\bar{\theta}$ and frequency for the various test configurations at the high sound pressure levels. In some instances $\bar{\theta}$ increased with frequency and in others it decreased. At frequencies far from resonance, the resistance became small.

Effective Length of Vibrating Air Mass in Resonator Neck

In the computation of the natural frequency and reactance of resonator configurations, it is necessary to know the effective length of the vibrating mass. An end correction applied to the aperture neck makes the length of the vibrating air mass in the neck greater than the plate thickness t (see Fig. 1). As discussed by Ingard (1), the effective length can be written as

$$l_{eff} = t + 0.85d(1 - 0.7\sqrt{\sigma}) - \delta \qquad [12]$$

where δ is an experimentally determined correction factor. Ingard (1) found that δ could be correlated with the sound pressure level for single resonators.

Values of the correction factor were determined by means of Equations [7 and 12] from measurements of the natural frequency of the resonator configuration for sound pressure levels between 100 and 160 db. It was found that δ could not be correlated directly with the sound pressure level, but the per cent open area of the configuration had a predominant effect on δ as shown in Fig. 7. The value of δ appears to decrease until open areas of around 6 per cent are reached and then remains essentially constant at higher per cent open areas.

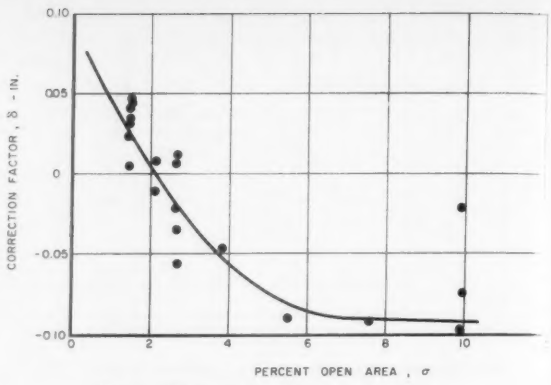

Fig. 7 Effective length correction factor

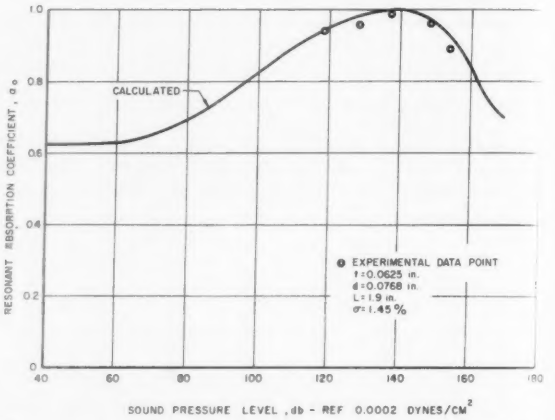

Fig. 8 Resonant absorption coefficient vs. sound pressure level

Design System for Screech Absorption Liners

In presenting a design system for screech liners, some consideration must be given to the required accuracy and utility of the system. With this in mind, a basic system is presented in which accuracy is compromised slightly for the sake of utility, and methods for improving the accuracy of the system at the cost of increasing the tediousness of the problem are indicated.

Basic Design System

An examination of the experimentally determined curves of acoustical reactance and resistance vs. frequency (see Figs. 6a and 6b) shows that a reasonable approximation to the curves can be made by assuming that the reactance is independent of the sound pressure level, and assuming that the resistance varies with sound pressure level but is invariant with frequency. On the basis of these assumptions, the equations describing the operation of the absorber can be written as

$$\alpha = \frac{4\bar{\theta}_0}{(\bar{\theta}_0 + 1)^2 + Q^2\bar{\theta}_0^2\,(f/f_0 - f_0/f)^2} \qquad [13]$$

where

$$Q = 2\pi f_0 l_{eff}/c\sigma\bar{\theta}_0 \qquad [14]$$

$$\bar{\theta}_0 = \frac{4(\pi\mu\rho f_0/g)^{1/2}(1 + t/d + \Delta_{ni}/d)}{\sigma\rho c} \qquad [15]$$

$$f_0 = \frac{c}{2\pi}\sqrt{\frac{\sigma}{Ll_{eff}}} \qquad [16]$$

$$l_{eff} = t + 0.85d(1 - 0.7\sqrt{\sigma}) - \delta \qquad [17]$$

In most practical liner designs the backing distance L and the liner thickness t will generally be fixed because of considerations of strength and cooling requirements. The diameter of an aperture that can be conveniently punched in a plate of thickness t, as well as cooling flow requirements, put limitations on the values of d which can be tolerated. With these restrictions, the per cent open area σ appears to be the most convenient variable to control in designing a liner.

Equations [13 through 17] can be solved for a selected value of σ by using Figs. 5 and 7. An optimum σ can then be determined by plotting the absorption coefficient vs. selected values of frequency f with σ as a parameter. The optimum σ is that value which gives the maximum value of the absorption coefficient over the widest frequency bandwidth. The same procedure can be followed to optimize the aperture size d if there is sufficient variation allowable in d to warrant the added difficulty.

In cases where the absorption bandwidth is too narrow, it will be necessary to change the value of Q (see Eq. [14]) for the system. The Q value is proportional to the inverse of the damping coefficient and is a measure of the absorption bandwidth. A system having a high Q value absorbs very selectively and has a narrow bandwidth. Systems with a low Q value usually have less peak absorption but absorb over a wider range of frequencies. Therefore, judgment must be used to achieve a required absorption over the required frequency range. Variations in Q can probably best be achieved by varying the aperture diameter d, and both σ and d should be optimized if the required bandwidth cannot be achieved by optimizing σ alone.

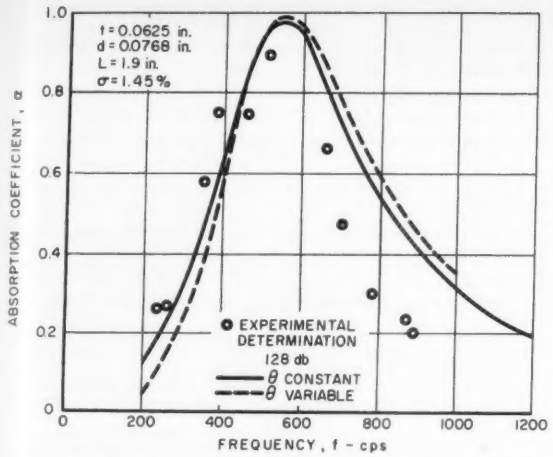

Fig. 9a Comparison of measured and calculated absorption coefficients—128 db

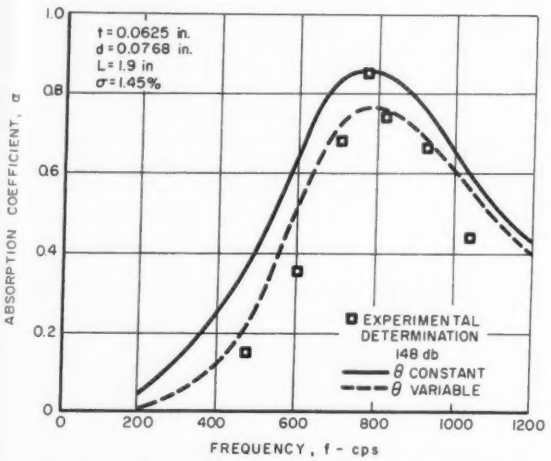

Fig. 9b Comparison of measured and calculated absorption coefficients—148 db

If variations in d are impractical, the effective Q of the system can be controlled by providing multiple absorption-liner sections having different peak frequencies.

The simplifying assumptions introduced in the design system appear to be justified because large errors in the value of $\bar{\theta}$ result in small errors in the absorption coefficient. In Fig. 8 a comparison is presented of the calculated and experimental values of the resonant absorption coefficient as a function of sound pressure level obtained from a typical test configuration. Good agreement was obtained, and the effect of the nonlinear losses is quite apparent. The nonlinearities are unimportant below sound pressure levels of about 80 db, but at higher levels they change the absorption coefficient markedly. At approximately 140 db the nonlinear corrections increase the value of $\bar{\theta}$ to 1, and a theoretical 100 per cent absorption is obtained. Further increase in $\bar{\theta}$ by the nonlinear corrections causes the absorption coefficient to decrease. The importance of the nonlinear considerations in liner design is obvious.

Improvements in Accuracy of Design System

Sources of error in the basic design system are the assumption that the facing resistance is independent of frequency and the use of the correlation presented in Fig. 5 to determine the nonlinear resistance term Δ_{nl}/d. Without these simplifying assumptions, Equation [15] in the equations describing the operating characteristics of the absorber is replaced by Equation [5]. (It should be noted that f and not f_0 is used in Eq. [5] for computing $\bar{\theta}$.) Equation [17] can be solved for l_{eff} as before by using Fig. 7, and Equation [16] can be solved for f_0. If the correlations of Figs. 4a and 4b are used, it is necessary to calculate the particle velocity and/or the displacement in the resonator neck. The particle velocity can be computed from Equation [8], where P_i is the pressure amplitude of the incident wave. The particle displacement is given by

$$s = u/2\pi f \qquad [18]$$

The correlation of Fig. 4a should be used to determine Δ_{nl}/d except for very thin plates where the plate thickness is less than the critical value of approximately 0.023 in. (1). For these thin plates, the correlations of Fig. 4b should be used. For plate thicknesses greater than critical, a given σ, sound pressure level, aperture diameter and frequency, Equations [5 and 8] can be solved by trial and error by using Fig. 4a. The absorption coefficient can then be determined from Equation [3]. The process can then be repeated for various frequencies to determine the absorption coefficient as a function of frequency. If the plate thickness is less than critical, the correlation of Fig. 4b can be used in a similar manner in conjunction with Equations [5 and 18].

Figs. 9a and 9b present a comparison of experimentally measured absorption coefficients obtained for a typical configuration and absorption coefficients calculated using both the simplified ($\bar{\theta}$ constant) and rigorous ($\bar{\theta}$ variable) procedures. Good agreement was obtained between the measured and calculated values. The more complicated calculation procedure described here appears to give better agreement with the experimental data at the higher sound pressure levels, but the simplified design procedure differs only slightly from the more complicated procedures.

Conclusions

1 The resistance of an absorption liner to a sound wave is composed of a configuration resistance and a nonlinear resistance dependent on sound pressure level. At levels higher than about 100 db, the nonlinear resistance controls the absorption characteristics of the liner. This nonlinear resistance can be correlated with the sound pressure level of the waves being absorbed.

2 The effect of increased sound pressure level on absorption depends on the physical dimensions of the resonator. For most practical configurations, an increase in the sound pressure level will cause an increase in the theoretical absorption coefficient to a value of 100 per cent between 120 and 150 db followed by a continuous decrease.

3 The effective length of the air mass vibrating in the resonator aperture is dependent on the per cent open area of the absorber configuration. Absorption liners having open areas ranging between 1 and 12 per cent should satisfactorily eliminate screeching combustion under most conditions.

Nomenclature

a = distance between the centers of individual resonators necks arranged in a square array, ft
c = velocity of sound, fps
d = aperture diameter, ft (unless noted otherwise)
db = sound pressure level, 0.0002 dynes/cm²
f = frequency, sec^{-1}
f_0 = resonant frequency, sec^{-1}
g = gravitational constant, 32.2 fps²
i = imaginary quantity, $\sqrt{-1}$
l_{eff} = effective length of aperture mass, ft

L = absorber backing distance, ft (unless noted otherwise)
p = excess pressure in sound wave, lb/ft²
P_i = sound pressure amplitude of incident wave, lb/ft²
Q = measure of the absorption bandwidth (Eq. [14]), dimensionless
s = particle displacement, ft
t = plate thickness, ft (unless noted otherwise)
u = particle velocity, fps
α = absorption coefficient, dimensionless
α_0 = absorption coefficient at resonance, dimensionless
α_ϕ = absorption coefficient with non-normal incidence, dimensionless
δ = effective length correction factor, ft (unless noted otherwise)
Δ_{nl} = nonlinear correction factor, ft
$\tilde{\theta}$ = specific acoustic resistance ratio for resonator array, dimensionless
$\tilde{\theta}_0$ = specific acoustic resistance ratio at resonance, dimensionless
λ = wave length, ft
μ = viscosity, lb/sec-ft
ρ = density, lb-sec²/ft⁴
σ = fraction of open area of resonator array, $(\pi d^2)/(4a^2)$
ϕ = angle of incidence of non-normal waves
$\tilde{\chi}$ = specific acoustic reactance ratio for resonator array, dimensionless

Subscripts

c = critical conditions
max = maximum value
min = minimum value

References

1 Ingard, U., "On the Theory and Design of Acoustic Resonators," *J. Acoustical Soc. Amer.*, vol. 25, no. 6, Nov. 1953, pp. 1037–1061.
2 Zwikker, C. and Kosten, C. W., "Sound Absorbing Materials," Elsevier Publishing Co., N. Y., 1949, chap. 7.
3 Beranek, L. L., "Acoustics," McGraw-Hill Book Co., Inc., N. Y., 1954, p. 138.
4 London, A., "The Determination of Reverberant Sound Absorption Coefficients from Acoustic Impedance Measurements," *J. Acoustical Soc. Amer.*, vol. 22, no. 2, March 1950, pp. 263–269.
5 Ingard, U. and Labate, S., "Acoustic Circulation Effects and the Nonlinear Impedance of Orifices," *J. Acoustical Soc. Amer.*, vol. 22, no. 2, March 1950, pp. 211–218.
6 McAuliffe, C. E., "The Influence of High Speed Air Flow on the Behavior of Acoustical Elements," M.Sc. Thesis, Massachusetts Institute of Technology, 1950.
7 Morse, P. M., "Vibration and Sound," McGraw-Hill Book Co., Inc., N. Y., 1948, second ed., p. 242.

Technical Notes

Specific Heat Inequality Effect in the Chemically Frozen Stagnation Point Boundary Layer

GEORGE R. INGER[1]

University of Michigan, Ann Arbor, Mich.

IT HAS often been assumed, for purposes of mathematical simplicity in the dissociated laminar boundary layer problem, that the specific heats of the atomic and molecular species are equal.[2] This, of course, is not necessarily true and may lead to a significant error in the temperature gradient and heat transfer calculation for a highly cooled dissociated boundary layer. It is the purpose of this note to give a solution to the energy equation for chemically frozen flow at the stagnation point which takes this specific heat inequality into account and explicitly shows the resulting effect on the heat conduction and total heat transfer to a highly cooled wall for arbitrary Lewis number.

Received May 27, 1960.

[1] Graduate Student, Department of Aeronautical Engineering. Now with the Aerodynamic Research Group, Aero/Astrodynamics Dept., Missiles and Space Div., Douglas Aircraft Co., Inc., Santa Monica, Calif. Member ARS.

[2] The inequality of atomic and molecular species specific heats, including the temperature dependence of each specific heat, was included in the digital computations of reference (1). However, the explicit effect of this specific heat inequality was not displayed in the results given for temperature distribution or heat transfer.

At a symmetric body stagnation point, the application of the well-known similarity transformation

$$\xi = \int_0^x \rho_w \mu_w U_e r_0^{2k} dX$$

($k = 0$ two dimensional, $k = 1$ axially symmetric)

$$\eta = \rho_e U_e (2\xi)^{-(1/2)} \int_0^y \frac{\rho}{\rho_e}\, dY$$

$$U = U_e f'(\eta)$$

$$\rho\mu = \rho_w \mu_w$$

reduces the laminar boundary layer equations for a dissociated air mixture to the following set of ordinary differential equations in the absence of homogeneous chemical reactions

$$S_c f z_F' + z_F'' = 0 \qquad [1]$$

$$[P_R f + (1 + L_e)(\bar{C}_p'/\bar{C}_p)]\theta_F' + \theta_F'' = 0 \qquad [2]$$

where

F = chemically frozen flow
S_c = Schmidt number
L_e = Lewis number ($S_c = P_R/L_e$)
z_F = $\alpha_A/\alpha_{A_e} = \sum_{\text{atoms}} \alpha_i \Big/ \sum_{\text{atoms}} \alpha_{ie}$, total atomic species mass fraction referred to that at the edge of the boundary layer
θ_F = T/T_e
$\bar{C}_p$ = $C_{pm} + \alpha_{A_e} z_F (C_{p_A} - C_{pm})$, frozen specific heat of the mixture

EDITOR'S NOTE: The Technical Notes and Technical Comments sections of ARS JOURNAL are open to short manuscripts describing new developments or offering comments on papers previously published. Such manuscripts are usually published without editorial review within a few months of the date of receipt. Requirements as to style are the same as for regular contributions (see masthead page).

It has been assumed in Equation [2] that the atomic and molecular specific heats, C_{pA} and C_{pm}, respectively, are unequal constants. The boundary conditions for these two equations in the absence of wall mass transfer are: $z_F(\infty) = \theta_F(\infty) = 1$, $\theta_w = T_w/T_e$ given, and either $z_F(0) = 0$ (completely catalytic wall) or $z_F'(0) = 0$ (completely noncatalytic wall).

Under the assumed conditions of a highly cooled wall ($\theta_w \ll 1$), it has been shown by Lees (2)[3] that it is sufficiently accurate to take $f(\eta)$ as the Blasius function for the purpose of solving the composition and energy equations. Consequently, these equations become linear and can be readily integrated. Equation [2] can be solved as a first-order equation in z_F' to yield

$$z_{F\text{cat.}} = 0.47\, S_c^{1/3} \int_0^\eta \exp\left(-S_c \int_0^\eta f d\eta\right) d\eta$$

$$z_{F\text{noncat.}} = 1 \qquad [3]$$

With the composition distribution known, Equation [2] can now be solved to indicate the effect of the specific heat inequality term on the frozen boundary layer temperature distribution. For the case of zero atom recombination at the wall surface ($z_F = 1$, $\bar{C}_p' = 0$), we see immediately that $C_{pA} - C_{pm}$ has absolutely no effect on the temperature distribution. However, in the opposite extreme of complete atom recombination at the wall [$z_F(0) = 1$, $\bar{C}_p' \neq 0$], the specific heat difference introduces a dependence of the temperature distribution on the atomic species distribution. As a first-order equation in θ_F', Equation [2] can be integrated twice to the following solution

$$\theta_{F\text{ at.}} = \theta_w + (1 - \theta_w)[I_1(\eta)/I_1(\infty)] \qquad [4]$$

where

$$I_1(\eta) = \int_0^\eta \left[\frac{\bar{C}_p(\eta)}{\bar{C}_p(0)}\right]^{-(1+L_e)} \exp\left(-P_R \int_0^\eta f d\eta\right) d\eta \qquad [5]$$

Now for a catalytic wall

$$\frac{\bar{C}_p(\eta)}{\bar{C}_p(0)} = 1 + \alpha_{A_e} z_{F\text{cat.}} \left(\frac{C_{pA}}{C_{pm}} - 1\right)$$

varies from zero at the wall to a value of 0.20 at the edge of the boundary layer for the typical case $\alpha_{A_e} = 0.50$, $C_{pA}/C_{pm} = 1.40$. Hence it appears permissible for most practical problems to use the approximation

$$\left[\frac{\bar{C}_p(\eta)}{\bar{C}_p(0)}\right]^{-(1+L_e)} \simeq 1 - (1 + L_e)\alpha_{A_e} z_F \left(\frac{C_{pA}}{C_{pm}} - 1\right)$$

Concerning ourselves only with the effect on wall temperature gradient, then, this simplifying approximation gives $\theta_F'(0)$ from Equations [4 and 5] as

$$\theta_F'(0) \simeq \frac{0.47\, P_R^{1/3}(1 - \theta_w)}{1 - 0.47 P_R^{1/3}(1 + L_e)\alpha_{A_e}(C_{pA}/C_{pm} - 1) I_2(\infty)} \qquad [6]$$

[3] Numbers in parentheses indicate References at end of paper.

where

$$I_2(\eta) = \int_0^\eta z_{F\text{cat.}} \exp\left(-P_R \int_0^\eta f d\eta\right) d\eta \qquad [7]$$

$$I_2(\infty) \simeq 1.49(0.47\, S_c^{1/3})(0.47 P_R)^{-2/3} \qquad [8]$$

Equation [6] clearly shows that the effect of $C_{pA} - C_{pm}$ increases the catalytic wall temperature gradient and raises the entire temperature profile above the corresponding noncatalytic wall solution. For the typical example $S_c = 0.50$, $P_R = 0.70 (L_e = 1.40)$, $\alpha_{A_e} = 0.50$ and $C_{pA}/C_{pm} = 1.40$, Equations [6 and 8] give $\theta_F'(0)/[\theta_F'(0)]_{C_{pA} = C_{pm}} \simeq 1.357$, i.e., a 36 per cent increase in the wall temperature gradient owing to the composition influence introduced into the energy equation when $C_{pA} = 1.4 C_{pm}$.

The total heat transfer rate to the wall $\dot{Q}_w$ can be written in the following nondimensional form in the similarity plane for chemically frozen flow

$$\frac{P_R(\dot{Q}_w/C_{pm}T_e)_F}{\sqrt{\rho_w \mu_w (1 + k)(dU_e/dX)_{stag.}}} \equiv \dot{q}_F = \frac{\bar{C}_p(0)}{C_{pm}} \theta_F'(0) + L_e z_F'(0) \frac{h_D}{C_{pm} T_e} \qquad [9]$$

where

$$h_D = \sum_{\text{atoms}} \alpha_{i_e} h_{f_i}(0)$$

is the average heat of formation (dissociation energy) in the dissociated external flow. In the noncatalytic wall case ($z_F' = 0$), there is no diffusion and only the heat conduction transfer exists

$$\dot{q}_{F\text{noncat.}} = 0.47 P_R^{1/3}[1 + \alpha_{A_e}(C_{pA}/C_{pm} - 1)](1 - \theta_w) \qquad [10]$$

In this case, the specific heat inequality does not change the temperature gradient but does increase the thermal conductivity for constant P_R, hence increasing the total heat transfer proportionally to $\alpha_{A_e}(C_{pA}/C_{pm} - 1)$. On the other hand, the catalytic wall accepts the full heat of recombination by diffusion [$z_F(0) = 0$, $z_F'(0) = 0.47\, S_c^{1/3}$]; the thermal conductivity at constant P_R is unaffected by $C_{pA} - C_{pm}$[$\bar{C}_p(0) = C_{pm}$], but the wall temperature gradient is increased according to Equation [6]. Consequently, we have

$$\dot{q}_{F\text{cat.}} \simeq 0.47 P_R^{1/3}\left[\underbrace{\frac{1 - \theta_w}{1 - 0.47 \times 1.49(0.47/L_e)^{1/3}(1 + L_e)\alpha_{A_e}(C_{pA}/C_{pm} - 1)}}_{\text{conduction}} + \underbrace{L_e^{2/3}\left(\frac{h_D}{C_{pm}T_e}\right)}_{\text{diffusion}}\right] \qquad [11]$$

In addition to the diffusion term, the catalytic wall heat transfer is also larger than that for the noncatalytic case because of the relatively greater effect of the specific heat inequality on the conduction term. For example, in the previously cited case $S_c = 0.50$, $P_R = 0.70$, $\alpha_{A_e} = 0.50$ and $C_{pA}/C_{pm} = 1.4$, we have

$$[\dot{q}_F/(\dot{q}_F)_{C_{pA} = C_{pm}}]_{\text{noncat. conduction}} = 1.200$$

$$[\dot{q}_F/(\dot{q}_F)_{C_{pA} = C_{pm}}]_{\text{cat. conduction}} \simeq 1.357$$

The magnitude of these ratios suggests that the specific heat inequality effect on the heat transfer in the highly cooled dissociated boundary layer on a hypersonic body should be taken into account in engineering calculations.

References

1 Fay, J. A. and Riddell, F. R., "Theory of Stagnation Point Heat Transfer in Dissociated Air," Avco-Everett Res. Lab., Everett, Mass., Research Rep. 1, April 1957.

2 Lees, L., "Laminar Heat Transfer Over Blunt-Nosed Bodies at Hypersonic Flight Speeds," Jet Propulsion, vol. 26, no. 4, April 1956, p. 259.

Transient Heat Conduction in a Melting Finite Slab: An Exact Solution

R. W. SANDERS[1]

Lockheed Missiles and Space Div., Sunnyvale, Calif.

Transient heat conduction in a melting finite slab is studied. Solutions are determined for which the melting rate is inversely proportional to the amount of unmelted material. The solutions obtained demonstrate that a better measure of accuracy for any numerical procedure is its ability to predict the melting rate and not the grosser quantity—the total amount melted.

IN GENERAL, the only exact solutions for the transient heat conduction equation are for linear problems on regions of simple shapes. When nonlinear problems are considered, solutions for arbitrary heat flux input can be obtained only by numerical methods. Since very little is known about the convergence and stability of numerical procedures for nonlinear problems, it is desirable to have exact solutions of typical problems for comparison. This paper presents such a solution for a nonlinear transient heat conduction problem of current interest. This solution will be used to compare the effects of two different heat flux inputs on the quantities of interest.

The temperature distribution and the melting rate of a one-dimensional finite slab, with constant thermal properties, subjected to a specific heat flux input will be determined. The slab, originally extending from $x = 0$ to $x = a$, has the face $x = a$ insulated and has heat flowing in through the other face at a rate $H_0(t)$ per unit area. Only the phase of the problem that involves the actual melting will be considered. It is assumed that all molten material is removed immediately upon formation, so that the face which was initially at $x = 0$ moves inward, and at time t is at the position $x = S(t)$ (1).[2] In terms of the specific heat c, density ρ, thermal conductivity K, latent heat of a fusion L, melting temperature T_m and the temperature distribution at the start of melting $[T_0(x)]$, the process is described by

$$c\rho \frac{\partial T}{\partial t} = K \frac{\partial^2 T}{\partial x^2} \qquad S(t) < x < a, t > 0 \qquad [1a]$$

$$T(x, 0) = T_0(x) \qquad 0 < x < a \qquad [1b]$$

$$\partial T/\partial x = 0 \qquad x = a, t > 0 \qquad [1c]$$

$$T[S(t), t] = T_m \qquad t > 0 \qquad [1d]$$

$$H_0(t) = -K \frac{\partial T}{\partial x} + \rho L \frac{dS}{dt} \qquad x = S(t), t > 0 \qquad [1e]$$

The essential difficulty is that the problem is defined for a region having an unknown moving boundary. Following the guide of Landau (1), the moving boundary can be eliminated by the transformation $\xi = (a - x)/[a - S(t)]$. If, in addition, the dependent variables are nondimensionalized by defining

$$\theta(\xi, t) = [T(\xi, t) - T_m]/T_m \qquad s(t) = S(t)/a \qquad [2]$$

the problem can be stated as

$$\frac{(1 - s)^2}{r} \frac{\partial \theta}{\partial t} = \frac{\partial^2 \theta}{\partial \xi^2} - \xi \left[\frac{1 - s}{r} \frac{ds}{dt}\right] \frac{\partial \theta}{\partial \xi} \qquad 0 < \xi < 1, t > 0 \qquad [3a]$$

$$\theta(\xi, 0) = \theta_0(\xi) \qquad 0 < \xi < 1, t = 0 \qquad [3b]$$

$$\partial \theta/\partial \xi = 0 \qquad \xi = 0, t > 0 \qquad [3c]$$

$$\theta(1, t) = 0 \qquad t > 0 \qquad [3d]$$

$$H_0(t) = \frac{T_m K}{a(1 - s)} \frac{\partial \theta}{\partial \xi} + \rho L a \frac{ds}{dt} \qquad \xi = 1, t > 0 \qquad [3e]$$

$$r \equiv K/\rho c a^2 \qquad [4]$$

For an arbitrary $H(t)$ and a nontrivial initial temperature distribution, this problem must be solved numerically. Since we are attempting to develop a solution that may be used to check the accuracy of numerical techniques, we need not study the direct problem but will consider the indirect one. That is, if ds/dt is chosen, then Equations [3a, 3b, 3c and 3d] form a well-posed boundary value problem with Equation [3e] as the specifying equation for $H_0(t)$. A similar procedure was followed by Baer and Ambrosio (2) for the semi-infinite slab. If $s(t)$ is chosen such that, with A as an arbitrary real constant

$$(1 - s)^2 = 1 - 4A^2 rt \qquad [5]$$

the bracketed term in Equation [3a] is a constant, namely $2A^2$. After changing independent variables by setting $y = A\xi$, Equation [3a] becomes

$$\frac{(1 - s)^2}{A^2 r} \frac{\partial \theta}{\partial t} = \frac{\partial^2 \theta}{\partial y^2} - 2y \frac{\partial \theta}{\partial y} \qquad 0 < y < A, t > 0 \qquad [6]$$

Since the problem has been defined for positive t, the fact that ds/dt is nonzero at $t = 0$ presents no difficulties.

The problem can now be solved by separation of variables. Let $\theta(y,t) = f(y)g(t)$. Then

$$\frac{f''}{f} - 2y \frac{f'}{f} = \frac{(1 - s)^2}{A^2 r} \frac{g'}{g} = -4\lambda \qquad [7]$$

where λ is an unknown constant. Making the change of variable $y^2 = Z$ changes the equation for f into a well-known form having two independent solutions in terms of the confluent hypergeometric function

$$f(y) = B_1 F_1(-\lambda; \tfrac{1}{2}; y^2) + C y {}_1F_1(\tfrac{1}{2} - \lambda; \tfrac{3}{2}; y^2) \qquad [8]$$

Here

$${}_1F_1(\alpha; \gamma; x) \equiv 1 + \frac{\alpha}{\gamma} \frac{x}{1!} + \frac{\alpha(\alpha + 1)}{\gamma(\gamma + 1)} \frac{x^2}{2!} + \cdots$$

The second term of Equation [8] can be eliminated by applying boundary condition [3c]. Use of boundary condition [3d] gives the eigenvalue equation

$${}_1F_1(-\lambda; \tfrac{1}{2}; A^2) = 0 \qquad [9]$$

The function ${}_1F_1(-\lambda; \frac{1}{2}; A^2)$ behaves like $\cos(A\sqrt{4\lambda + 1})$ for large values of λ. Hence, there exist $\lambda = \lambda_n$ such that Equation [9] is satisfied. From the form of the ${}_1F_1$ function, we can show that $\lambda \leq 0$ cannot satisfy Equation [9]. That λ_n must be real will be shown in the discussion of the orthogonality property of these functions.

To study orthogonality, change the dependent variable from $f_n(y)$ to $\varphi_n(y)$ as follows

$$\varphi_n(y) = e^{-y^2/2} f_n(y) \sim e^{-y^2/2} {}_1F_1(-\lambda_n; \tfrac{1}{2}; y^2) \qquad [10]$$

Then $\varphi_n(y)$ satisfies the Sturm-Liouville equation

$$\varphi_n'' + (4\lambda_n + 1 - y^2)\varphi_n = 0 \qquad [11]$$

In this form it is easily seen that the eigenvalues are real, and that the φ_n are orthogonal over the interval $(0, A)$. That is

$$\int_0^A \varphi_n \varphi_m \, dy = \begin{cases} 0, & m \neq n \\ N_n^2, & m = n \end{cases} \qquad [12]$$

and the normalizing factor N_n can be calculated.

Received June 2, 1960.

[1] Thermodynamics Engineer. Presently at Dept. of Mathematics, Arizona State Univ.

[2] Numbers in parentheses indicate References at end of paper.

From Equations [5 and 7] we see that $g_n(t) \sim (1 - 4A^2rt)^{\lambda_n}$.

The indirect problem is linear; we can therefore write the general solution by superposition

$$\theta(y,t) = \sum_n D_n(1 - 4A^2\,rt)^{\lambda_n}{}_1F_1(-\lambda_n; \tfrac{1}{2}; y^2) \qquad [13]$$

The values of the D_n can be determined by applying the initial condition and using the orthogonality property of the $\varphi_n(y)$. It is apparent from the relation of the D_n to $\theta_0(y)$ that a proper choice of $\theta_0(y)$ will greatly simplify the numerical calculations required. With the D_n determined, Equation [3e] specifies $H_0(t)$, the heat flux required to generate the melting rate indicated by Equation [5].

When the function $(-1)_1F_1(-\lambda_0; \frac{1}{2}; A^2\xi^2)$, where λ_0 is the least eigenvalue, is chosen for the initial temperature distribution, the general solution given by Equation [13] reduces to a one-term solution. This function chosen for $\theta_0(\xi)$ is well-behaved for almost all A. The one-term solution for the temperature distribution, with the required heat flux input, is

$$\theta(\xi, t) = -(1 - 4A^2rt)^{\lambda_0}{}_1F_1(-\lambda_0; \tfrac{1}{2}; A^2\xi^2) \qquad [14a]$$

$$H_0(t) = 2\lambda_0\,{}_1F_1(1 - \lambda_0; \tfrac{1}{2}; A^2) \cdot \frac{T_mK}{a}(1 - 4A^2rt)^{\lambda_0 - 1/2} + \frac{2LKA^2}{ca}(1 - 4A^2rt)^{-1/2} \qquad [14b]$$

Several solutions have been obtained using various values for A:

A^2	λ_0	$2\lambda_0\,{}_1F_1(1 - \lambda_0; \frac{1}{2}; A^2)$
0.5	1.0	2.0
0.85403	0.5	2.3491
0.99	0.40514	2.4933
1.00	0.39922	2.5041

Aspects of the last two solutions indicated are presented in the figures for typical thermal properties. Fig. 1 shows the temperature distribution at times $t = 0$ and 20 sec. The initial temperature distribution is essentially the same for $A = 1$ and $\sqrt{0.99}$. Fig. 2 shows $H_0(t)$ and ds/dt vs. t for $A = 1$. Fig. 3 shows the percentage differences of $H_0(t)$ and ds/dt for the two solutions as functions of time. These results indicate that a perturbation of $H_0(t)$ is reflected immediately in ds/dt even though it might go unnoticed in $s(t)$. Thus a better measure of accuracy of any numerical procedure is its ability to predict ds/dt and not just the grosser quantity $s(t)$. This is also evidenced by writing the differential equation in the form [3a] instead of [1a].

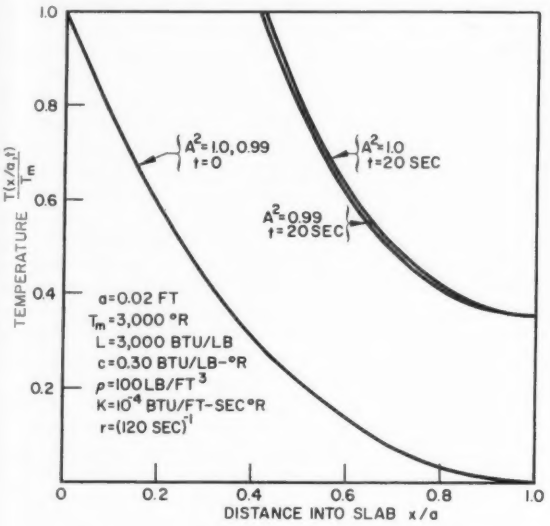

Fig. 1 Temperature profiles in a melting slab

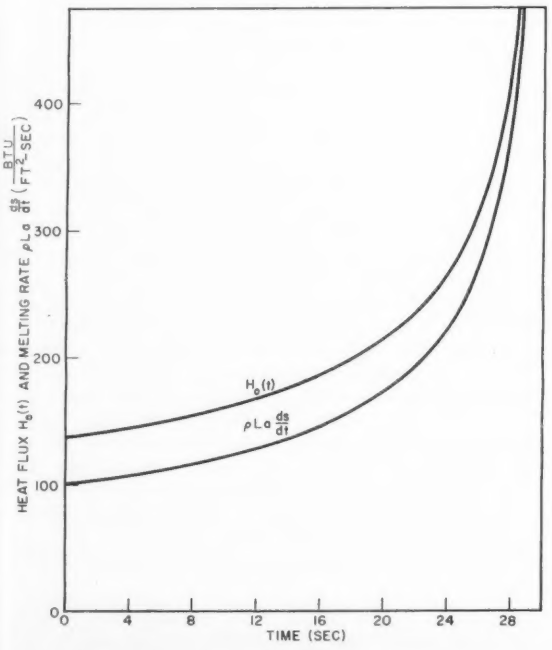

Fig. 2 Heat flux and melting rate vs. time

References

1 Landau, H. G., "Heat Conduction in a Melting Solid," *Quart. J. Appl. Math.*, vol. 8, no. 1, April 1950, pp. 81–94.

2 Baer, D. and Ambrosio, A., "Heat Conduction in a Semi-infinite Slab with Sublimation at the Surface," TR-59-0000-00610, Space Technology Laboratories, Inc., Los Angeles, Feb. 24, 1959.

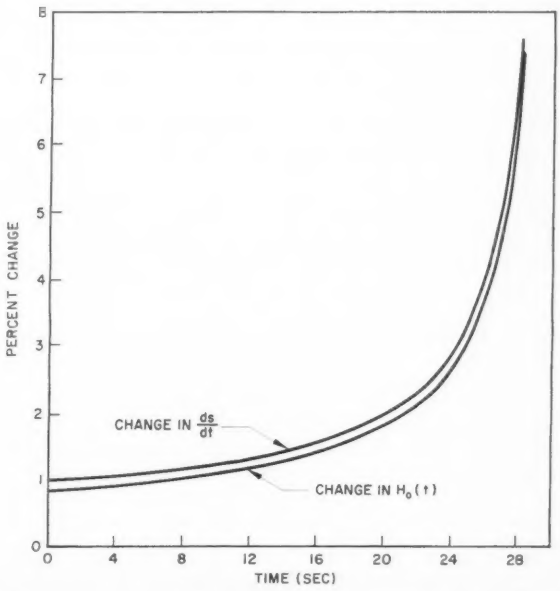

Fig. 3 $(H_0 - H_0^e)/H_0$ and $[(ds/dt) - (ds^e/dt)]/(ds/dt)$ vs. t

Further Comments on the Measurement of the Speed of Propagation of Turbulent Combustion

R. E. BOLZ[1] and H. BURLAGE Jr.[2]

Case Institute of Technology, Cleveland, Ohio

THE AUTHORS wish to discuss Professor Shchelkin's recent criticism (1)[3] of the combustion model and method of data processing employed in their paper published in 1955 (2). The experiments discussed in that paper involved the ignition, by means of a single spark pulse, of a jet of homogeneously mixed natural gas (methane) and air. This produced a small spherical flame kernel which was carried along by the moving stream. From successive photographs of the growing kernel, taken with a high speed camera and a shadowgraph optical system, the apparent flame propagation speeds were determined by direct measurement. The actual flame speeds relative to the unburnt gases were calculated by eliminating the growth rate of the flame kernel due to the constant pressure adiabatic increase of volume. This was done using

$$\frac{S_{\text{actual}}}{S_{\text{apparent}}} = \frac{NRT}{N_b R_b T_b} = C$$

where

N,R,T = number of moles, gas constant and absolute temperature of unburned gases, respectively
b = burned gases
S = flame speed

By calculating the constant C in this manner it is implied that the flame front or combustion zone width is thin compared with the radius of the flame kernels, and, therefore, the combustion is complete within the confines of the observed flame front. Professor Shchelkin, however, disagrees with this assumption and believes that although the assumption is valid for laminar flow, it is not valid for turbulent flow. He believes that for the turbulent case the combustion zone will be of the order of 5 mm in thickness, a value quite large compared with the kernel diameters that were measured in these experiments and which never exceeded 30 mm. As a result, he predicts that the values of the turbulent flame speeds given in (2) are only about half of what he estimates they should be. His estimate is based upon a combustion situation where v' the average turbulent perturbational component of flow velocity is very large compared with S_n the normal flame speed.

Professor Shchelkin comments further that the dependence of the flame velocity on the radius of the flame kernel, shown in Figs. 7, 14, 15 and 16 of (2), are not to be expected. He reasons that due to the damping of the turbulence with distance one should actually expect a decrease in flame speed, and that this expectation would be realized if the value of the constant C were evaluated as he suggests, i.e., the value of C calculated on the basis of a thick flame of the order of 5 mm.

The authors seriously disagree with Professor Shchelkin's criticisms as presented in (1), and this disagreement is based upon several arguments which will be discussed here.

In the combustion experiments under consideration, a spark pulse ignited a small but finite mass or kernel of homogeneously mixed fuel and air. This ignition process took place in a matter of microseconds, and the initial shape of the flame front was essentially independent of the mild stream turbulence as is shown in (2). The combustion surface thus begun was enlarged as the flame front moved into the unburned mixture and as the high temperature gases produced within the kernel expanded. Since there is no dependence upon turbulent or diffusion mixing of the fuel and air (which were premixed), it appears reasonable to hypothesize that for this case of very mild turbulence, where the value of the root-mean-square perturbation velocity was usually less than 3 fps, the combustion will propagate at the normal laminar flame velocity at each point on the flame front. Consequently the mild turbulence that was generated in the flow field by screens would have only the effect of slowly distorting and wrinkling the essentially spherical flame front. An important fact here is that in the experiments of (2) the complete time lapse for each sequence of photographs was usually less than 0.01 sec, the same order of magnitude as the characteristic time of turbulence, and during this complete time lapse, the *average* perturbation velocity component was only about 2 fps. The effect of such turbulence, then, cannot be immediate, but must develop slowly during the very short time period of observation. Furthermore, the authors can visualize no mechanism for this mild turbulence to produce the thick flame front pictured by Professor Shchelkin. It appears much more reasonable to hypothesize that, in the case of the experiments of Bolz and Burlage, since the normal flame speed is approximately equal to the mean turbulent perturbational velocity components, the flame should progress as stated here, as an essentially laminar flame front which is being slowly wrinkled by the turbulence. This wrinkling is a transient process; it is building up during the short time of the photographic observations. If the studies could extend over a longer time period than that available to the experimenters (and *without* decay of turbulence), then one would expect an asymptotic steady-state value of flame propagation rate to be reached. This is much the same as the mechanism pictured by Scurlock and Grover in (3). *With* turbulence decay, one would expect an increase to some maximum value of apparent flame propagation rate due to increased flame front surface area (but not a change in the basic mechanism of propagation) followed by a decrease in this rate which would eventually approach the laminar value.

Furthermore, based upon this model of a wrinkled laminar flame and the theory of (3), an equation relating the kernel radius (reduced by the factor C) with the time was derived in recent work by the authors[4] taking into account the damping of the turbulence. The theoretical values obtained from this equation were compared with new and much more precise and extensive data taken in the past few years by Bolz and Burlage [similar to that in Figs. 7, 14, 15 and 16 of (2)], and the comparison showed a remarkable correlation in all cases between the theory and the experimental data as reduced by the method of the Bolz and Burlage paper (2). Such a correlation does not prove the validity of either the theory or the data reduction method but does lend support to the authors' arguments.

The authors will certainly agree with Professor Shchelkin that if the rms turbulent perturbational velocities v' were very large compared with S_n the normal flame velocity ($v' >> S_n$), the rapid oscillation of the mixture at the flame front would almost certainly result in a thick flame zone. This is the case pictured by Professor Shchelkin and the assumption upon which he bases his flame front thickness calculation in the absence of any other information. However, it is just this fact, that the v' and S_n involved in the work of (2) are of approximately equal magnitude, that the authors believe substantiates their view.

As a further substantiation for the authors' methods,

Received May 19, 1960.

[1] Professor of Aeronautical Engineering.

[2] Associate Professor of Aeronautical Engineering.

[3] Numbers in parentheses indicate References at end of paper.

[4] This work will be published shortly as an NASA publication and may be obtained on loan in prepublication form from Professors Bolz and Burlage, Case Institute of Technology.

(*Continued on page 1089*)